COMPUTATIONAL MODELS OF INFLAMMATION AND WOUND HEALING

by

Cordelia Ziraldo

BS Mathematics, University of Chicago, 2005

Submitted to the Graduate Faculty of

School of Medicine in partial fulfillment

of the requirements for the degree of

Doctor of Philosophy

University of Pittsburgh

2013

UNIVERSITY OF PITTSBURGH

SCHOOL OF MEDICINE

This dissertation was presented

by

Cordelia Ziraldo

It was defended on

April 16, 2013

and approved by

James Faeder, PhD, Assistant Professor, University of Pittsburgh Department of Computational and Systems Biology

Greg Constantine, PhD, Professor, University of Pittsburgh Department of Mathematics

Robert F. Murphy, PhD, Professor, Carnegie Mellon University Department of Computational Biology

Gary An, MD, Associate Professor, University of Chicago Department of Surgery

Dissertation Advisor: Yoram Vodovotz, PhD, Professor, University of Pittsburgh Department

COMPUTATIONAL MODELS OF INFLAMMATION AND WOUND HEALING

Cordelia Ziraldo, PhD

University of Pittsburgh, 2013

The acute inflammatory response to biological stress involves a highly conserved cascade of events mediated by a large array of cells and molecules. While not intrinsically detrimental, inflammation can cause secondary or ancillary damage to tissues, which in turn leads to the production of molecules that amplify inflammatory response and, in extreme cases, promote organ dysfunction and death. Therefore, there is a need to identify and modulate dysregulated inflammatory processes while allowing healthy inflammation to carry on. While *in vitro* and *in vivo* studies have brought many insights into the components and dynamics of the inflammatory response, computational techniques are becoming increasingly relevant to tease out complex relationships and inter-dependencies that may not be directly measureable. In this dissertation, we explore a computational model of pressure ulcer formation that generates tissue-realistic output and clinically-relevant predictions. By simulating basic inflammatory mechanisms and ischemia/reperfusion injury to soft tissue, our model spontaneously produces both resolving and ulcerative inflammatory patterns from a single set of parameter values. We use statistical methods to explore which mechanisms in the model are responsible for this spontaneous bifurcation. We also use data-driven methods to examine dynamics of inflammatory mediators during *in vitro* murine hepatocellular stress. Our results lead to identification of MCP-1 as a clinically-predictive inflammatory mediator in human trauma patients.

TABLE OF CONTENTS

LIST OF TABLES

LIST OF FIGURES

PREFACE

I would like to thank all of my colleagues who contributed to the work presented here via helpful discussions: Alexey Solovyev, Qi Mi, Ruben Zamora, Joyeeta Dutta-Moscato, Nabil Azhar, Justin Hogg, Grace Huang, and Luis Pedro Coelho.

I am also very grateful to Sandra Yates, Kelly Gentille, and Thom Gulish for their help and support on numerous occasions throughout my graduate career.

I would especially like to acknowledge each of my committee members, all of whom were generous with their time and enlightening with their guidance. This is especially true of my advisor, Yoram Vodovotz. It has been a pleasure learning from you.

And finally, I would like to thank my ever-supportive family, without whom this would not be possible: John, Monica, and Quirico Ziraldo, and Ken Overwater. You all mean the world to me; I'm so happy to be able to share this with you.

1.0 INTRODUCTION

Inflammation has evolved as a response to danger that functions to eliminate threats and restore the body to homeostasis. This is accomplished by clearing debris and pathogens before sensing tissue damage and initiating repair machinery. As a well-coordinated communication network, inflammation is a critical and necessary process that allows organisms to deal with a rapidly changing and often hostile environment. While not intrinsically detrimental, inflammation can cause secondary or ancillary damage to tissues, which in turn leads to the production of molecules that amplify inflammatory response and, in extreme cases, promote organ dysfunction and death (92). Many diseases, such as cancer, diabetes, atherosclerosis, Alzheimer's, and obesity are also associated with dysregulated inflammation. This feedback loop of damage to inflammation to damage also underlies the basis of multiple organ dysfunction syndrome (MODS) following trauma. Unmediated inflammation can cause damage to remote organs that were not involved in the initial traumatic injury. This, coupled with the initiating trauma is often fatal to patients who would have otherwise survived the initial assault. In wound healing, inflammation can be essential to clear out invading pathogens, but overactive pro-inflammatory cells can cause additional tissue damage before healing mechanisms are engaged. This additional damage can incite new inflammation, engaging the positive feedback mechanism mentioned above, leading to chronic wounds.

The acute inflammatory response to biological stress (e.g. infection or tissue injury/damage) involves a highly conserved cascade of events mediated by a large array of cells (e.g. mast cells, macrophages, neutrophils, natural killer cells, dendritic cells, and T- and B-lymphocytes) and molecules (inflammatory cytokines, free radicals, and Damage-Associated Molecular Pattern molecules [DAMPs]) that locate invading pathogens or stressed/damaged tissue, alert and recruit other cells and molecules, eliminate the offending agents, and finally restore the body to equilibrium. The interplay of these functional modules is what determines the success or failure of the inflammatory response. These intracellular signaling networks and their products, including diffusible molecular mediators, are in essence the carriers of information in the network of inflammatory communication and therefore possible targets for intervention. The problem is that any given pathway or mediator may exert either beneficial or detrimental effects in a dynamically varying fashion based on the nature of the wound and the particular aspects of the individual patient. Selecting likely therapeutic targets for wound healing – in a rational fashion that takes into consideration this complex system as a whole – is thus a tremendously difficult task.

Chronic, non-healing wounds present a significant burden of both time and money to the healthcare community. Wounds, whether developed in hospital or present on admission, pose a great threat to a patient's health. They provide an opportunity for pathogens to invade and simply divert resources that the body could be using to restore health elsewhere. Furthermore, the inflammatory response incited can lead to extreme complications, especially when it becomes dysregulated. Wounds pose a specific problem to researchers in that they cannot be sampled clinically, without necessarily perturbing their course. In addition, it is essentially impossible to modulate all possible mechanisms of inflammation and wound healing in an attempt to find

novel therapies. While mathematical modeling has been useful in helping to integrate these mechanisms, the increasing availability of spatial, non-invasive data (such as clinical photographs) and physico-mechanical information suggests the need for new modeling approaches to leverage these new data sources to enhance the discovery of effective therapeutic regimens.

An alternative method for studying such a complex, clinically-realistic system is to use a mechanistic computational model based on literature knowledge, which could be compared to data from lab experiments or clinical subjects, which in turn may have applications in diagnosing/predicting the wound healing trajectories of individuals or possibly in the design of novel therapeutic modalities for wound healing. Extensive work has gone into computational studies of wound healing, spanning many stages of this process, from re-epithelialization and cell migration to collagen deposition and scar formation, to angiogenesis (84; 90).

Agent-Based modeling is an object-oriented, rule-based, discrete event computational modeling technique well suited for integrating and synthesizing cellular and molecular-level data, and provides a useful translational tool for examining stochastic and spatial aspects of inflammation and wound healing (7). In an Agent-Based Model (ABM), agents representing individual cellular or molecular components of a system populate a "virtual world," in which their simulated behaviors are governed by rules extrapolated from known data regarding their true biological behaviors (7). Component-level mechanistic detail can be included in the rules that govern the behavior of agents. Typically, both the qualitative pattern and predicted quantitative time evolution of the agents (variables) can be assessed using agent-based models. Because the rules in an ABM define local, instantaneous interactions and since the rules governing agent behavior are probabilistic, the overall behavior of the system being simulated

will often be different than what was hypothesized from the rules put into the model. The power of agent-based modeling is highlighted by the degree that these system-level effects, sometimes called “emergent phenomena”, reflect real outcomes observed in traditional biological research (36). In this dissertation, an ABM of pressure ulcer formation was created and matched to clinical images of pressure ulcers in individuals with spinal cord injury. In chapter 2, we describe the process of model development, calibration to clinical images, and comparison to mechanistic data from the literature. The model was also used as a platform for *in silico* clinical trials of potential therapies. Two distinct, clinically-relevant phenotypes emerged spontaneously from simulations of the model despite starting with the same set of parameter values. In chapter 3, statistical methods were employed to explore the cause of the spontaneous divergence, with the hope of developing mechanistic hypotheses for which treatment strategies could be devised.

In addition to modeling the synthesis of understood mechanisms, additional questions persist about the nature of the complex interactions that make up the inflammatory response. Mathematical and computational (*in silico*) methods have emerged as adjuncts to *in vitro* and *in vivo* studies of acute inflammation to tease out the dynamics of key mediators (7). For example, we have recently applied both mechanistic and data-driven computational modeling to help define the dynamic, multi-dimensional inflammatory response to Trauma/ Hemorrhagic Shock (T/HS) *in vivo* (8-12). In chapter 4, we sought to determine if combined *in vitro*/*in silico* studies could help elucidate key hepatic inflammatory mediators relevant to human T/HS. We identified the chemokine Monocyte Chemoattractant Protein-1 (MCP-1) as a main driver of the response of hepatocytes *in vitro* and as a biomarker for organ damage in clinical settings of T/HS, and, more generally, suggests a pathway for combined experimental and computational studies to facilitate the discovery of novel clinical biomarkers of inflammation.

2.0 A TISSUE-REALISTIC, COMPUTATIONAL MODEL OF PRESSURE ULCER FORMATION IN INDIVIDUALS WITH SPINAL CORD INJURY

This chapter comes from a manuscript by the same name that is currently under review at *Science Translational Medicine*. (**Ziraldo, C.;** Solovyev, A.; Allegretti, A.; Krishnan, S.; Henzel, M.K.; Sowa, G.A.; Brienza, D.; An, G.; Mi, Q.; Vodovotz, Y.; A Computational, Tissue-Realistic Model of Pressure Ulcer Formation in Individuals with Spinal Cord Injury.) In this work, I developed an agent-based model of pressure ulcer formation in soft tissue overlaying a bony prominence. I incorporated mechanisms of ischemia/reperfusion and inflammatory-induced injury and calibrated the model to clinical photographs of people with spinal cord injury. Model behaviors were compared to qualitative data from the literature, and emergent phenomena were observed that match clinical realities. Sensitivity analysis was performed to determine which mechanisms of injury had the greatest influence on model outcomes, and finally the model was used as an *in silico* platform for testing anti-inflammatory therapies, corticosteroids and anti-HMGB1 antibodies. Once this manuscript is published, the model code will be available at: www.pitt.edu/~cirm/spark.

2.1 ABSTRACT

Spinal cord injury (SCI) predisposes those afflicted to pressure ulcers (PU). PU remain a significant problem in cost of patient care and quality of life despite advancements in mechanistic understanding and technological interventions. An agent-based model (ABM) of ischemia/reperfusion-induced inflammation and PU (the PUABM) was created, calibrated to serial images of post-SCI PU, and used to investigate potential treatments *in silico*. System-level features of the PUABM recapitulated visual patterns of ulcer formation in people with SCI. Sensitivity Analysis of model parameters suggested that increasing oxygen availability would reduce PU. An *in silico* trial of corticosteroids using the PUABM suggested that early application of corticosteroids at a sufficiently high dose could attenuate local inflammation and reduce pressure-associated tissue damage, but could not reduce PU incidence. An *in silico* trial of neutralizing antibody targeted at Damage-Associated Molecular Pattern molecules suggested no efficacy. Thus, tissue-realistic, clinically calibrated models such as the PUABM may yield novel mechanistic insights and suggest a therapy development platform for complex inflammatory diseases.

2.2 INTRODUCTION

Pressure ulcers (PU) affect 2.5 million US acute care patients per year, costing up to $1 billion per year (75). They are a significant source of morbidity in hospitalized patients as well as in community-dwelling individuals with impaired mobility. These ulcers are especially common (80% at some point in life) in people with spinal cord injury (SCI), a condition associated with

decreased functional mobility, acutely increased oxidative activity in leukocytes and chronic elevation in systemic inflammatory markers (15; 39; 82). Pressure ulcers are thought to arise from pressure-induced ischemia, reperfusion injury, shear forces, and moisture (34). Despite increased understanding of the underlying mechanisms and improved clinical vigilance, PU remain a prevalent problem in hospitalized patients (14).

The pathogenesis of PU involves activation of the inflammatory response (43; 71), consisting of a highly conserved cascade of events mediated by a set of specialized cells (e.g. platelets, mast cells, macrophages, and neutrophils) and molecules (inflammatory cytokines, free radicals, and Damage-Associated Molecular Pattern molecules [DAMPs]) that demarcate stressed/damaged tissue, and alert and recruit other cells and molecules. This inflammatory response can either restore the tissue to equilibrium (healing) or propagate self-maintaining inflammation that inhibits wound healing and can lead to PU (90). The complex, dynamic interplay of the various functional modules of the intertwined inflammatory and healing cascades determines the ultimate success or failure of the healing process. These intracellular signaling networks and their products, including diffusible molecular mediators, are possible targets for therapeutic intervention. However, the complexity of the process as a whole, and the dependence of any given pathway or mediator on timing and context, complicates such therapeutic approaches.

We and others have suggested that computational modeling could underlie the rational design of therapies for inflammatory diseases, including aberrant wound healing (6; 90). Differential equations are the classical method for computational modeling of biological processes, and have been used for decades to explore all phases of wound healing, from inflammation (98; 99), to wound closure (12; 28; 29; 53; 69; 100), to tissue remodeling and

angiogenesis (23; 61; 70). These computational models have incorporated aspects of mechanical stress, population dynamics, and biochemical signaling (84). This compendium of differential equation models has resulted in important insights into the wound healing response and has advanced our understanding of effective wound healing, as well as suggesting underlying pathological mechanisms and testing therapies *in silico* (61; 99).

The clinical verification of such computational models has been stymied by the difficulties inherent in obtaining tissue-level-- especially spatiotemporal-- data regarding the dynamics of inflammation and wound healing. While wound healing is well-studied in animal systems (32; 50; 80), only recently have experimental methodologies emerged that may allow for the study of the time courses of wound healing in humans (50). A continuing complication is that time courses of primary samples from humans with chronic wounds are difficult to collect without disturbing the very process being measured.

Wound images are, in theory, both plentiful and non-invasive-- unlike wound biopsies. We and others have generated spatially-realistic, agent-based computational models of inflammation and tissue injury/healing based on wound healing and inflammation (1; 7; 76; 87; 94; 95) literature. We hypothesize that wound images could be used to calibrate and validate tissue-realistic, mechanistic simulations of inflammation and healing.

Agent-Based Models (ABMs) allow for the investigation of both space- and time-dependent dynamics of complex systems via mechanistic simulations. The modeler provides behavioral rules that allow the model to proceed stepwise through discrete space and time. It is important to note that while the most of the rules that govern model behavior are deterministic, the simulation is stochastic and thereby likely replicates the randomness of biological processes.

As a simulation progresses, morphological features evolve that may be indicative of the trajectory of the simulation (7).

We report herein on the creation of an ABM of PU formation (the Pressure Ulcer Agent Based Model, or PUABM) that incorporates key inflammation mechanisms. Explicitly included was the forward feedback loop of inflammation to damage to inflammation that has served as the core motif of our prior simulations of inflammation in both systemic and local contexts (90; 93). The PUABM replicates the visual morphology associated with the development and resolution of post-SCI PU by simulating the effect of repeated ischemia/reperfusion (representing the turning of a person with SCI in bed) on vascularized soft tissue overlaying a bony prominence (the clinically recognized "pressure points" at which PU typically develop). We demonstrate the possible utility of the PUABM as a platform for *in silico* clinical trials for PU prevention and treatment post-SCI, since the prevalence of PU remains high despite great efforts to implement strategies for improved patient care (13; 75). Our study therefore suggests the possibility for a novel, *in silico*-aided platform for discovery, diagnosis, and development of therapeutic targets in the settings of complex inflammatory diseases in which pattern-oriented data such as wound images are readily available.

2.3 MATERIALS AND METHODS

2.3.1 Model Implementation

The PUABM was built using SPARK, a platform designed for agent-based modeling of biological systems, freely available for download at: www.pitt.edu/~cirm/spark (86). SPARK

models are written in a logo-like language called SPARK-PL and run on a java platform (85) . SPARK models contain agents-- autonomous entities that interact with each other and the environment, called Space-- and data layers, corresponding to individual species in the environment that can diffuse, etc. The behavior of the model is determined by rules that govern how and when agents interact and react. These rules are generally written to be interpreted by one agent at a time, and therefore are necessarily restricted in scope (both time and space). A rule specifies how much an agent should move, produce, change an internal variable, etc. when it encounters a certain amount or type of data layer or agent in its immediate neighborhood. Model rules can be probabilistic in nature, allowing the model to evolve in a stochastic manner. Therefore, the behaviors and patterns produced by simulating several ticks of the model in succession arise as emergent phenomena resulting from the accumulated actions of a population of agents over time.

The components of the PUABM are described in Table 2.1, and the operant biological mechanisms and tissue structures are shown graphically in Fig.2.1. In the PUABM, simulation time is linked to actual time using the lifespans of cellular agents. A macrophage lifespan ranges from 100-150 ticks in our simulation, corresponding to 100-150 hours (4-6 days) of actual clock time. Neutrophil lifespans range from 10-20 ticks (hours) in the tissue, but increase when neutrophils become activated. Each simulation takes roughly five minutes to compute on an IBM Power6™ 575 supercomputing node, which has a 32 processor core with each one running at 4.7 GHz, making it possible to complete approximately 1000 simulations per day. The model contains 68 numerical parameters that are set by the modeler and 11 random variables whose values are set throughout the course of a simulation by a random number generator. At any given tick, the maximum number of agents computed in the model is on the order of 10^5.

Table 2.1: Summary of Agents, Data Layers, and their interactions encoded in the ABM. Substances are all encoded as Data Layers; Cells are all encoded as Agents, each with its own type. See Fig. 2.1 for schematic.

Substances in ABM	Cell Sources in ABM	Biological Functions in ABM
DAMPs	secreted by damaged Tissue cells	Chemo-attract and Activate Neutrophils
TNF-α	secreted by Activated Neutrophils	Chemo-attract resting and M1 Macrophages, activate Macrophages to M1 state
IL-1β	secreted by M1 Macrophages	Chemo-attract resting and M1 Macrophages, activate Macrophages to M1 state, at high levels activate Macrophages to M2 state
TGF-β1	secreted by M2 Macrophages	Chemo-attract resting and M2 Macrophages, activate Macrophages to M2 state
ROS	secreted by Tissue Cells on Reperfusion, by Neutrophils on death	Injure Tissue Cells
Oxidase	produced inside Tissue Cells during Ischemia	React with Oxygen to produce ROS
Oxygen	released by Blood Vessels	Necessary for Tissue Cell health, react with Oxidase to produce ROS

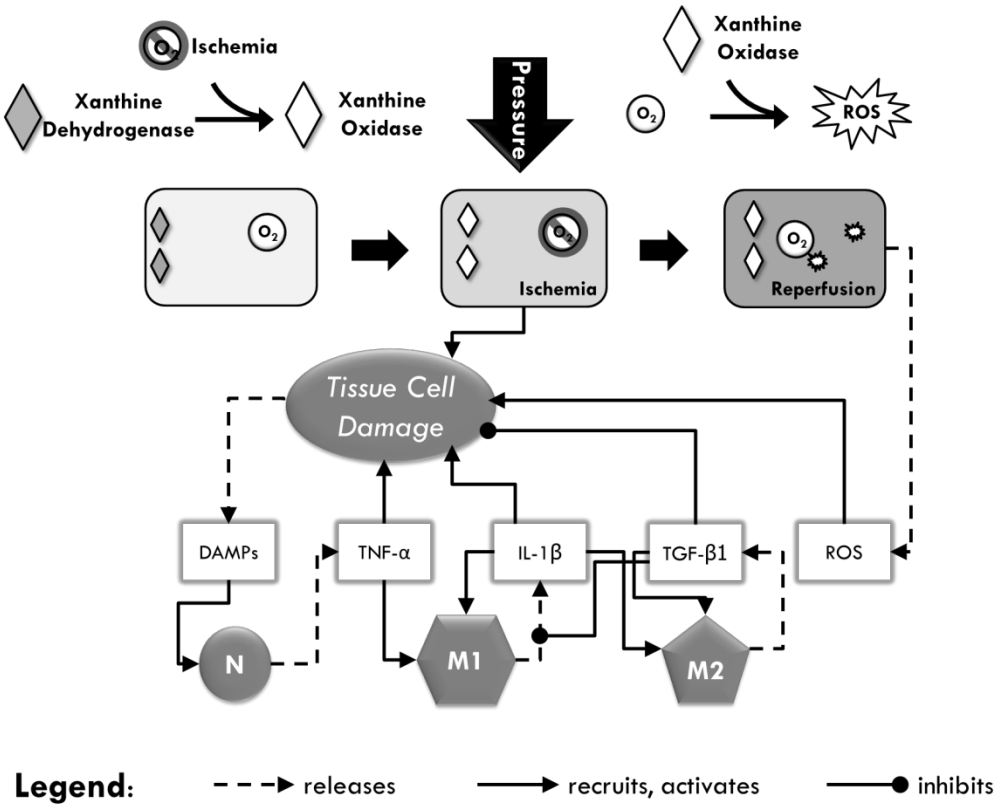

Figure 2.1. A schematic illustrates how model components interact to simulate two mechanisms of injury: ischemia/reperfusion injury and damage due to inflammation.
A tissue cell (muscle, fat, or skin) is situated over a bony prominence. When pressure is applied, oxygen supply is reduced and the cell becomes ischemic, leading to tissue damage. Simultaneously, the enzyme xanthine dehydrogenase is converted into xanthine oxidase. Thus, reactive oxygen species (ROS) are produced when pressure is released and oxygen flows back to the cell, causing further damage. Tissue damage causes the cell to release DAMPs, which, along with local concentrations of pro-inflammatory cytokines activate both neutrophils (N) and macrophages (M1, M2) when these mediators are present above a given threshold parameter. For example, a sufficiently high local concentration of DAMPs activates neutrophils to secrete TNF-α, which can activate macrophages to a pro- inflammatory M1 phenotype. Tissue damage is ameliorated by anti-inflammatory mediators [TGF-β1].

2.3.2 Work Flow

The PUABM was built using an iterative approach (Fig. 2.2). A simpler model of pressure ulcer formation (65) was altered to increase mechanistic detail and create clinically relevant model output by making rational improvements based on domain knowledge and data from the literature. First, the area of tissue simulated in the field was extended. Whereas in the previous

version of the model pressure was applied evenly across the entire field, in this version, it was applied maximally (value determined by the parameter, *pressure-intensity*) to a circular area in the center of the field and decreasing radially outward. This allowed representation of pressure over a bony prominence and the surrounding tissue, which also experiences pressure, but to a lessening degree (26; 55). Next, the PUABM code was altered so that neutrophils and macrophages enter the tissue in a resting state and can be activated by one of two circulating mediators (TNF-α or TGF-β1), which are released upon incitation of inflammation by damage. Then, circulating inflammatory cells were removed to a secondary viewing window and the colors indicating to tissue health were adjusted to increase the realism of the model's visual output so that it might be compared clinical images.

Mechanistic details in the PUABM were augmented by incorporating damage to tissue via ischemic injury and its counterpart, reperfusion injury. Damage directly associated with pressure was removed and a cost was applied to tissue health receiving inadequate oxygen levels. (In the previous version, oxygen had positive effects on tissue health, but lack of oxygen was not damaging.) A mechanism based on the conversion of xanthine dehydrogenase to xanthine oxidase during ischemia (21; 41) was also implemented. The accumulation of xanthine oxidase in ischemic cells represents the potential of a cell to experience reperfusion injury, due to formation of ROS when oxygen reperfuses (41). The complexity of the inflammatory response was increased by creating two subpopulations of activated macrophages, one with pro-inflammatory (M1 macrophages) and another with anti-inflammatory (M2 macrophages) phenotype (58; 66). A fourth mediator was also added. Representing a canonical late-acting pro-inflammatory mediator, it is released by pro-inflammatory macrophages and labeled IL-1β.

After the mechanisms comprising the PUABM were set, model behaviors were explored over wide ranges of parameter values and default values were tweaked into ranges producing behavior that qualitatively matched the clinical data. Finally, we further investigated dynamics encoded in the model by simulating hypothetical and existing therapies. Corticosteroids were incorporated as a data layer that could be introduced to the tissue via blood vessels (as in an IV injection), while antibodies to DAMPs were simulated as a topical cream applied to the entire field. The dose and timing of administrations of each were varied to assess the viability of these treatment options.

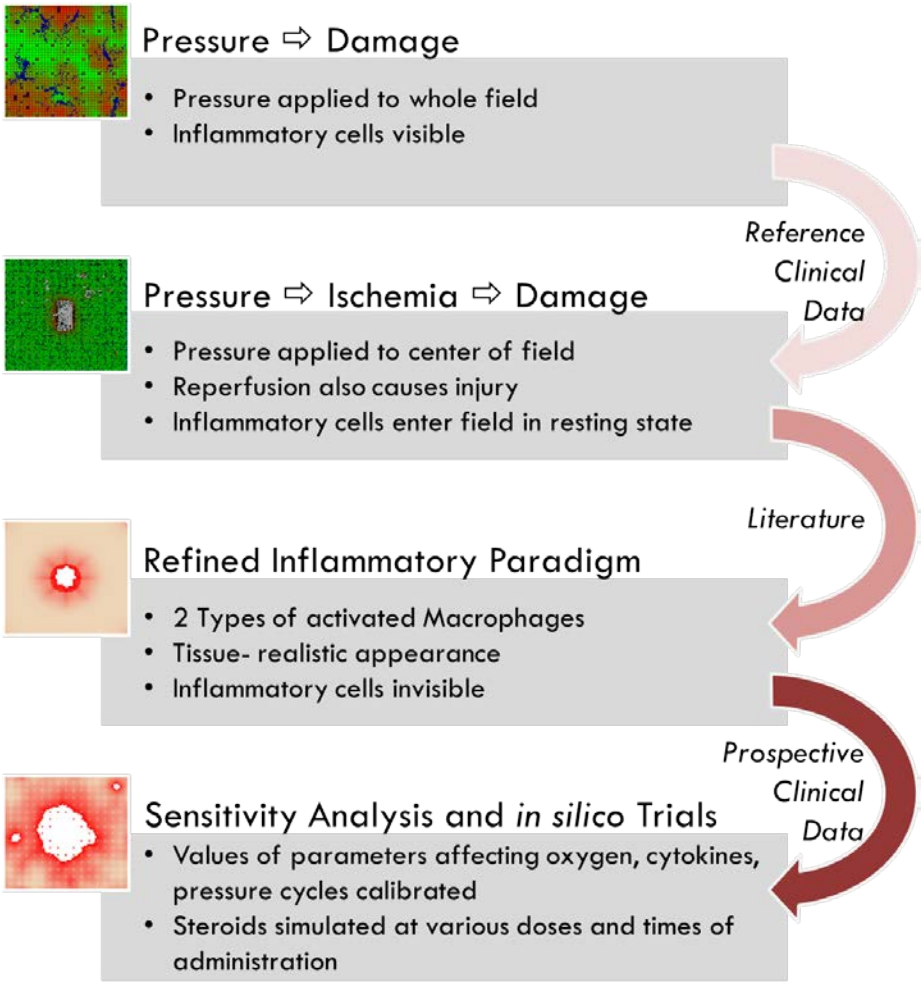

Figure 2.2. Work Flow.
The ABM was built iteratively, incorporating domain knowledge and data from the literature, then calibrated to clinical data. Initially, pressure directly injured tissue, thereby inciting inflammation. Ischemia/reperfusion injury was next added as a cause of injury, and the complexity of the inflammatory response was increased. Clinical data were next used to calibrate parameters in the model, and the model was subjected to sensitivity analysis and *in silico* trials.

2.3.3 Rules: Homeostasis/ Baseline Architecture

See pseudocode in Appendix for details of all rules. The architecture of the PUABM is abstracted from healthy tissue. The PUABM consists of a layer of tissue cells fed by blood vessels throughout the tissue that carry oxygen and inflammatory cells. Instead of explicitly representing red blood cells, their presence is implicit as oxygen flows through blood vessels unaccompanied. Inflammatory cells arrive to the tissue in their native resting state and are not activated unless danger signals are released from damaged tissue. Resting inflammatory cells move randomly, but can be chemo-attracted to local mediators.

The agents in the PUABM represent either cell types or cellular structures: neutrophils, macrophages, tissue cells, and blood vessels. Data layers are employed to represent mediators in a computationally efficient manner (e.g., diffusible cytokines, free radicals, oxygen, xanthine oxidase, and exogenously-administered drugs). Each tick of the model represents 1 h of real clock time. On each tick, the agents behave according to rules specific to their type: they produce and consume oxygen and mediators, are chemo-attracted to and activated (undergo a state change) by mediators; and they die, according to their lifespans. Mediators, represented in data layers, can be consumed or produced by individual agents or in reactions with other mediators. They undergo diffusion and degradation at each tick.

Tissue health is determined by local concentrations of oxygen, TNF-α, and TGF-β1. The inflammatory mediators have straightforward effects on increasing or decreasing tissue health. Oxygen can be both beneficial and detrimental, depending on whether its concentration is above or below a threshold.

To mimic natural patient-to-patient and cell-to-cell variability, some random variables were built into the model. These values were chosen from a given distribution as necessary as

simulations progressed. Some examples of random variables are size of each blood vessel agent (the blood vessels are all sized within a range but not exactly the same), and macrophage state change probability (if the concentration of a mediator is high enough and the random variable is in the right range then the agent changes state).

2.3.4 Rules: Pressure On/Off

The turning of people with SCI in bed was simulated as alternating cycles of pressure on/off. In the PUABM, pressure is simulated by constriction of blood vessels, decreasing the amount of material that can flow through them. Without oxygen, tissue cell health begins to decline. Ischemic tissue cells accumulate xanthine oxidase enzymes, which represent the capacity of the cell to produce damaging free radicals upon reintroduction of oxygen.

When pressure is released and oxygen again perfuses these cells, reactive oxygen species (ROS) are formed proportionally to the concentration of xanthine oxidase present in that cell. Free radicals cause damage to the immediate cell and those they encounter via diffusion, but they do so in a stepwise manner: tissue cells show no sign of damage from radicals until they have accumulated a certain threshold of insults. At that time, their health is reduced drastically.

2.3.5 Rules: Tissue Damage

Tissue cells that are stressed (have decreasing health) release diffusible danger signals (Damage-Associated Molecular Patterns [DAMPs]) that stimulate the inflammatory response by triggering the secretion of cytokines by inflammatory cells. Three diffusible mediators represent the canonical early pro-inflammatory response, the canonical slower pro-inflammatory response, and

the canonical anti-inflammatory response, each of which is secreted by activated neutrophils or M1 or M2 macrophages. Neutrophils and macrophages are initially in a resting state, and are activated by local concentrations of mediators in a threshold-dependent manner. A local concentration of DAMPs above a certain value will activate nearby neutrophils to produce early pro-inflammatory mediators (abstracted as the pro-inflammatory cytokine TNF-α). At a certain threshold of local TNF-α concentration, resting macrophages will be activated to a M1 phenotype and begin secreting longer-acting pro-inflammatory mediators (abstracted as IL-1β). TNF-α also causes damage to nearby tissue cells, thus re-stimulating the pro-inflammatory response. Local concentration of IL-1β above a threshold will activate macrophages to a M1 (pro-inflammatory) phenotype and, above a higher threshold, IL-1β will induce macrophages to a M2 (anti-inflammatory/reparative) phenotype. These phenotype changes are reversible, meaning a M2 macrophage could be induced to switch to a M1 phenotype if it encountered the right conditions, and vice versa. Active M2 macrophages produce anti-inflammatory mediators (abstracted as TGF-β1), which above a threshold will cause further activation of M2 macrophages (Fig. 1b). TGF-β1 also increases health of nearby tissue cells.

2.3.6 Implementation: Simulated Clinical Trials

Treatments with corticosteroids or neutralizing anti-DAMP antibodies were simulated as *in silico* clinical trials. These trials consisted of sets of model simulations in which parameters controlling drug dose and timing and tissue response were varied, each independently.

Corticosteroid administration was simulated as an IV injection. Therefore, steroid molecules (implemented as a data layer) were introduced to the tissue via blood vessels (and were restricted when pressure was applied). The mechanism of steroid action was to kill

inflammatory cells, regardless of their state (active/resting). When neutrophils were killed, some ROS was released by the dying cell.

Anti-DAMPs were simulated as a topical cream administration. A uniform layer of this molecule was introduced onto the field as a data layer at the tick specified by the parameter designating time of onset. The antibodies' method of action was controlled by a quenching reaction, where local concentrations of DAMPs were reduced by an amount proportional to the smaller concentration of the two molecules present: antibody or DAMPs.

2.3.7 Model Calibration

Parameter values were tweaked until the model gave qualitative behavior that was clinically applicable. The first test was to ensure that the "healthy" tissue was stable, i.e. when unperturbed the tissue was able to remain healthy. Clinical data was used as the baseline "reality," and consequently the PUABM is calibrated to SCI tissue, which has some unique properties. For uniformity of appearance, only visual properties of sacral ulcers within the clinical cohort were considered. The default parameters in the PUABM are calibrated to the tissue properties of these ulcers specifically, but the model has the capability to take on new tissue properties by altering a subset of the parameters. In examining the inflammatory dynamics of the PUABM, some adjustments were necessary to compare the numbers of cells. Because the agents in the model are not calibrated to specific numbers of cells, absolute population sizes from the PUABM are meaningless. Instead, each population of cells was normalized to bring the cell populations all into comparable range. For a given cell type at time t, its population count was normalized by dividing by the Euclidean norm of the vector containing counts of that cell type for each tick throughout that simulation. This procedure allowed us to compare the relative timing of the

peaks of each population. Presumably it is not only the number of cells present that determines the level of the response, but also how sensitive those cells might be to their environment, and vice versa. Therefore instead of calibrating for total number of cells, we focused on achieving reasonable qualitative behaviors.

2.3.8 Sensitivity Analysis

Because there are more than 50 free parameters in the model, it was impractical to examine the sensitivity of key model outputs to all of parameter space at once. Instead, modules of rules in the model that impacted tissue health were identified and used to create groups of parameters. Parameters within these groups were then prioritized according to the mathematical degree of their effect on the system. For example, a parameter that set the value of an exponent produces a more dramatic effect than one that sets a scalar multiple. Therefore, the first parameters varied were those controlling threshold values. Simulations initially varied over coarse grained and then finer grained threshold value ranges (100 simulations per parameter value). Total tissue damage by time t served as a quantitative output measure. From this a sensitivity index could be calculated for each parameter, taking the ratio of change in damage to change in threshold value.

A second level of sensitivity analysis was designed to examine the interplay between two potentially related parameter values (figs. 2.10-12). This allowed direct comparison of the sensitivities of two parameters and also revealed any secondary effects that occurred when the two changed in a combinatorial way. Parameters were chosen from the same “damage module” in order to get a sense of the relationships between “sub-processes” in each module. Snapshots of the tissue layer in the model across several fixed time points served as the output in order to

assess overall damage, presence and size of ulcer, and other qualitative features (data shown for only one time point per analysis, other time points not shown).

2.4 RESULTS

2.4.1 Model Properties: Overall Description of the PUABM

The PUABM represents vascularized soft tissue (skin, fat, muscle, or a composite thereof) overlaying a bony prominence. The tissue remains healthy as long as it is unperturbed and oxygen continues to flow to the field. Pressure-- such as that created by shifting a person's weight-- causes damage to the tissue by compressing the tissue and vasculature over the bone, restricting the flow of oxygen to the tissue and secondarily by formation of reactive oxygen species (ROS) upon reperfusion (when pressure is relieved). Injured tissue incites activation of inflammatory cells, which bring mediators to the field, some of which injure the tissue further. The molecular and cellular components of the model are enumerated in Table 2.1. The PUABM's mechanistic performance was compared to experiments from the literature, as described in Section 2.4.2.

Next, default parameters were set by comparing the visual output of the model to clinical images of PU developed during acute care or inpatient rehabilitation. These images were acquired following IRB approval from patients recruited to the study by the University of Pittsburgh Rehabilitation Engineering Research Center (RERC) on Spinal Cord Injury. Sensitivity analysis was performed, and finally the PUABM was used as a platform for *in silico* trials of strategies to prevent and slow the development of pressure ulcers. The process of model

development and implementation is shown graphically in Figs. 2.1 and 2.2 and detailed in the *Materials and Methods.*

2.4.2 Model Verification against tabular data: the PUABM recapitulates mechanistic dynamics of PU formation

The rules governing inflammatory mechanisms in the PUABM are based on dynamics of acute inflammation. These dynamics were initially tested in a simulated acute wound without repeated pressure cycles. Because the mediators in the simulation represent amalgams of several mediators, the dynamics were tabulated at the cellular level. In a successful implementation of these mechanisms, tracking activation of neutrophils and macrophages would reveal cellular dynamics similar to those found in settings of acute inflammation.

Two characteristic patterns of inflammatory cell dynamics spontaneously emerged from the same set of default parameter values. The timing of peaks was always the same, but that is where the similarities end. Every inflammatory cell count in the first pattern was at its maximum and still increasing at the end of the simulation (Fig. 2.3). In the second characteristic pattern, every cell type except M2 macrophages peaked well before the end of the simulation in the second pattern (Fig. 2.4). In fact, neutrophil counts dropped to zero relatively early in the time course and did not rise again. Tissue cell counts from simulations corresponding to each of the characteristic patterns suggested that every simulation that had the first pattern of inflammatory dynamics resulted in an ulcer, while all simulations corresponding to the second pattern did not. This was also verified by qualitative spatial pattern matching of visual outputs from simulations with both types of inflammatory dynamics.

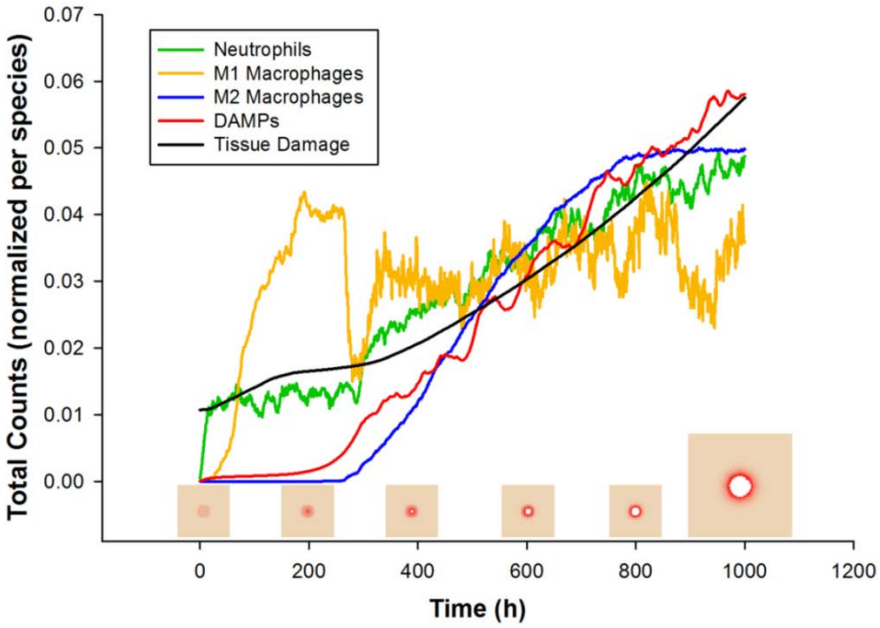

Figure 2.3. Ulcerative Inflammatory Dynamics.
A 35% initial injury without pressure is sufficient to induce self-perpetuating, damaging inflammation, leading to an ulcer. The relative dynamics of the response are as expected from the literature: an initial influx and activation of neutrophils, followed by M1 macrophages, and then followed by M2 macrophages.

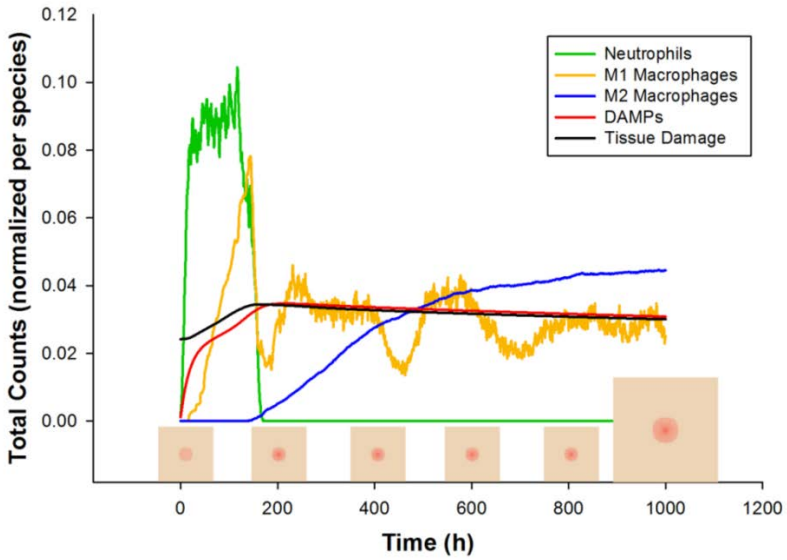

Figure 2.4. Non-progressing Inflammatory Dynamics.
In 10-20% of simulations with the same parameters and starting conditions, though the inflammatory response was incited, it did not become self-sustaining and consequently no ulcer formed. The trajectories of inflammatory cells are characteristic of each of these outcomes. Data were normalized per cell type, and so quantities are not relative.

If tissue damage was indeed caused by both ischemia *and* reperfusion, then all else being equal, a period of ischemia would be expected to cause less tissue damage than the same period of ischemia followed by reperfusion. This mechanistic knowledge might be important when designing prevention and treatment strategies. This I/R-damage hypothesis was confirmed by varying the length of pressure cycles (turning rate) while measuring total tissue damage (Fig. 2.5). As expected, both ischemia and reperfusion caused tissue damage. Holding the amount of ischemic time constant while increasing the number of reperfusion events led to earlier ulceration. However, the amount of damage incurred long term with a lower turning frequency (and thus longer ischemic periods) reached a level similar to that predicted by simulations of higher turning frequency (Fig. 2.5, inset).

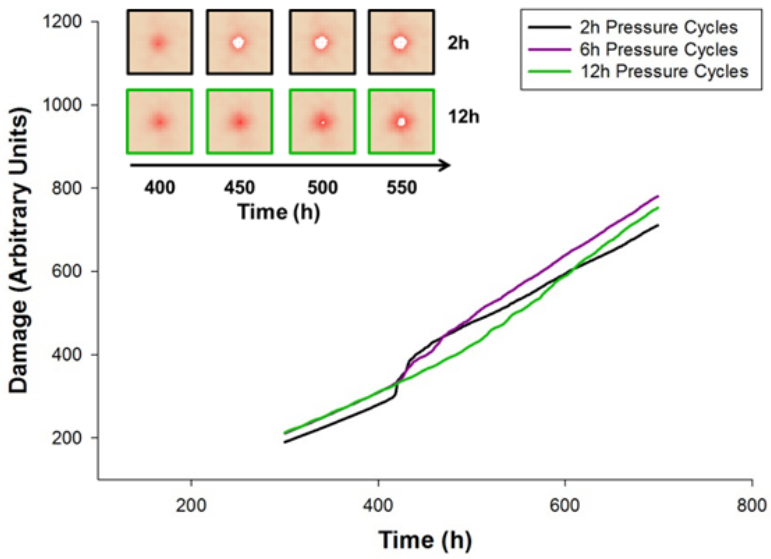

Figure 2.5. The ischemia/reperfusion injury mechanism was confirmed by varying the period of pressure (on/off) cycles.
Increasing the length of a pressure cycle allowed us to decrease the number of reperfusion events over the same length of ischemia. Pressure switched from on to off (or vice versa) once every 2, 6, or 12 hours. y-axis is total damage, x-axis is time (h). Pressure cycle length did not seem to affect the total amount of damage until just after t = 400 h. At that time point, the simulations with the shortest cycles (black) show a sudden increase in damage, which visually corresponds to the formation of an ulcer (see inset). Eventually, ischemic injury in simulations with the longest cycle length (green) causes these simulations to incur more overall damage. Periods of 4, 8, and 10 h yield intermediate curves (data not shown).

It was important to verify that the damage accumulated throughout a simulation is in fact due to the mechanisms of injury encoded in the model, and not to other spurious mechanisms. Unperturbed, the tissue remained healthy for thousands of simulated hours (Fig. 2.6 "No Pressure" data shown up to 1000 h; this behavior remained unchanged up to 5000 h [data not shown]). Some damage was observed when tissue was subjected to 12 h of simulated ischemia (Fig. 2.6 "12 hrs constant pressure"), but no further injury to the tissue was observed after release of pressure. By comparison, starting with a 35% injury over a patch of tissue at time 0 h (Fig. 2.6 "35% Initial Injury") was sufficient to incite the inflammatory response, ultimately leading to PU formation. However, this injury was not as damaging as repeated cycles of ischemia and reperfusion carried out over the complete time course (Fig. 2.6 "Default Parameters").

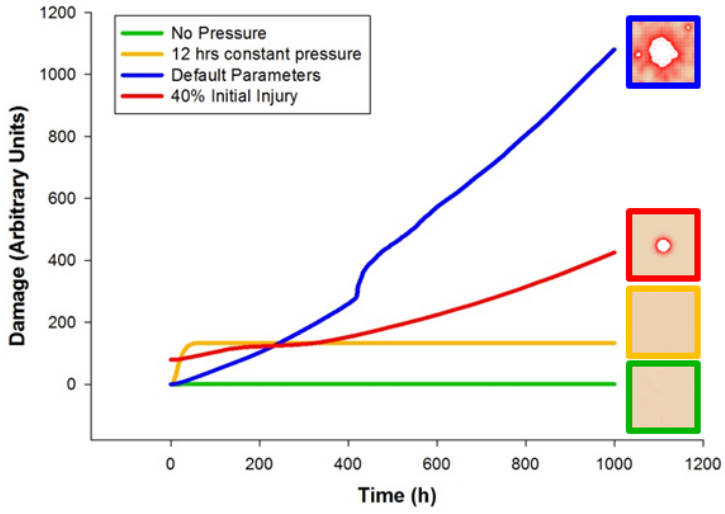

Figure 2.6. Negative controls verify that the model behaves as expected in various situations. Green: undisturbed, tissue health is stable for >5000 hours (data past 1000 h not shown). Yellow: an initial period of 12 h of ischemia causes damage to the tissue, but after release no further damage was incurred. Red: a characteristic damage curve for an ulcer caused by acute inflammation after 35% initial injury (similar to 2.3). Blue: a characteristic damage curve for a pressure ulcer resulting from the default parameters for the model.

2.4.3 Model Verification against spatial data: the PUABM recapitulates visual patterns from clinical images

Tissue health begins to decline in the area directly over the bony prominence within the first few hours of pressure cycling in the PUABM. This is manifested by a change in color, from peach to red (similar to the erythematous appearance of inflamed tissue). The tissue is able to recover some health in the first few rounds of pressure, during periods of reperfusion (data not shown). However, after a certain point, the tissue remains red (damaged) despite reflow of oxygen and leukocytes to the region. This is comparable to a region of unblanchable skin erythema that is the diagnostic criteria for a Stage I PU (*31*). Tissue health declines further as the simulation progresses, increasing the intensity and radius of redness. Tissue cells eventually begin to die, leaving behind a white patch to indicate lack of cellular activity at that position. This phenotype was considered to be the opening of a PU. From this point onward, the PU grows outward while cells near its edge continue to decline in health.

Simulations of the PUABM were initially compared to reference clinical images of PU severity (see Fig. 2.7). The National Pressure Ulcer Advisory Panel (NPUAP) has issued guidelines classifying ulcer severity by depth (18), i.e. type of tissue affected. In fact, the prevailing notion is that some ulcers begin as deep tissue injury before opening to the epidermal surface (17). While the PUABM is two-dimensional, simulations were nonetheless able to capture the appearance of a variety of PU of various degrees of severity. Furthermore, detailed features such as irregular shapes, jagged edges and secondary ulcers were also recapitulated. Specifically, the pattern of damaged tissue surrounding the ulcers was similar in simulations and clinical images. Also, as in clinical images, as PU severity increases, the size of the affected area

does as well. As shown in Fig. 2.7, simulations could achieve appearances similar to all four stages of ulcer progression.

The simulations also recapitulated evolution of PU development seen in a prospective patient cohort. The average time to ulceration post-injury was 20 ± 12 days among the RERC subjects, and with default parameters in the model the time to ulceration was 405 ± 6 hours (17 ± 1 days); there was no statistically significant difference between the simulation predictions and the actual RERC ulceration times ($p = 0.606$ by Mann-Whitney comparison on Ranks). The timing of ulceration in the PUABM was a result of model dynamics, since time of ulceration was not explicitly encoded to match the clinical data. By choosing parameter values that yielded reasonable inflammatory dynamics while obeying constraints for relative lifespans etc., the behaviors described here resulted as emerging phenomena.

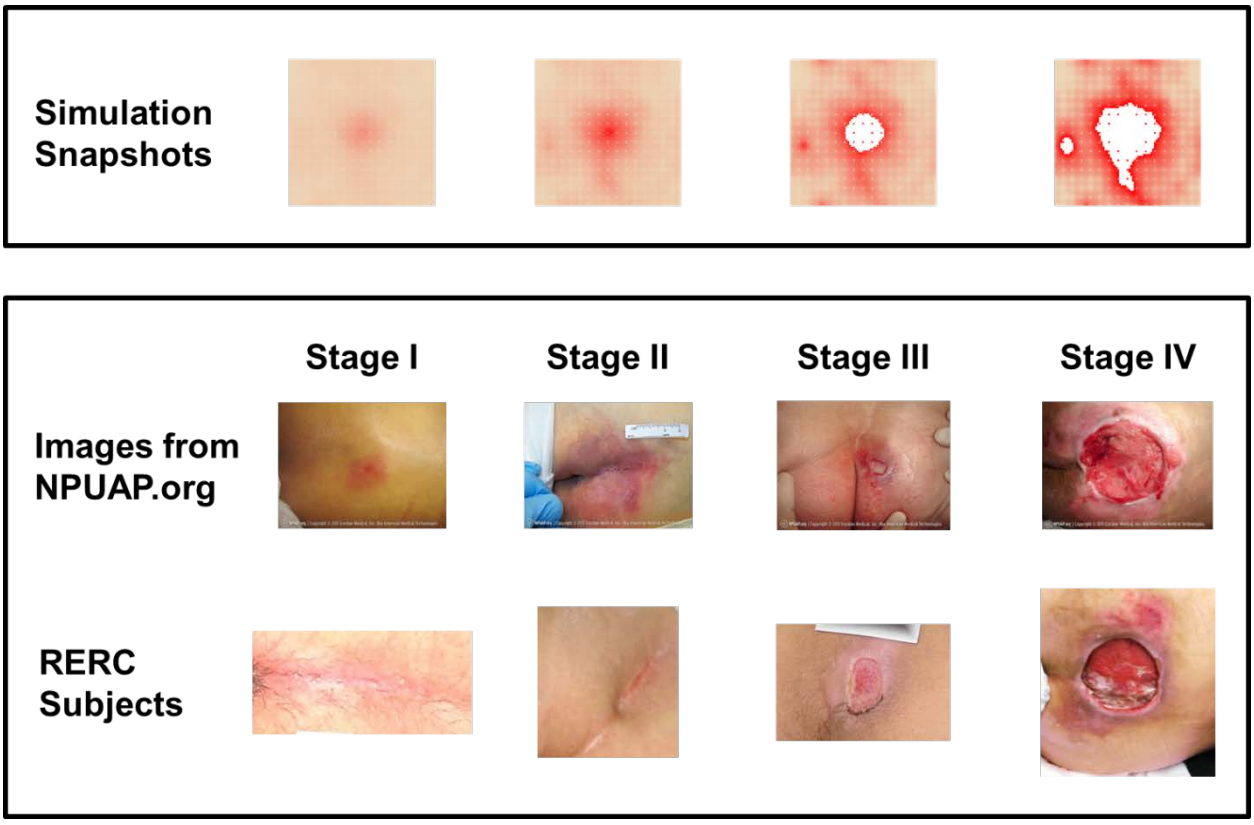

Figure 2.7 Simulations and Clinical Images.
Simulations achieved visual appearances with characteristics similar to each stage of PU development. The first row of clinical images come from the National Pressure Ulcer Advisory Panel (npuap.org, used with permission) and are of different subjects. Images in the second row are from people with SCI enrolled in a prospective study of PU at each stage. Irregular shapes and increasing nearby damage are observed in both sets of clinical data.

The reference clinical images are static snapshots of a dynamic process; moreover, the images are from different individuals. Accordingly, individual simulations of the PUABM were compared to the dynamics of PU formation in a single individual. Fig. 2.8 shows snapshots from a single simulation in which PU reached visual appearances with striking similarities to time courses of individual patients. Key characteristics of the PU arise in both simulations and patients. Though the simulated bony prominence is circular and the sacral pressure area is approximately a triangle, both time courses evolve ulcers with irregular shapes. Furthermore, in both simulations and real patients, once an ulcer formed, a second nearby ulcer was more likely

to develop. This phenomenon may be due to reduced tissue health and therefore increased vulnerability in the immediate vicinity of the ulcer.

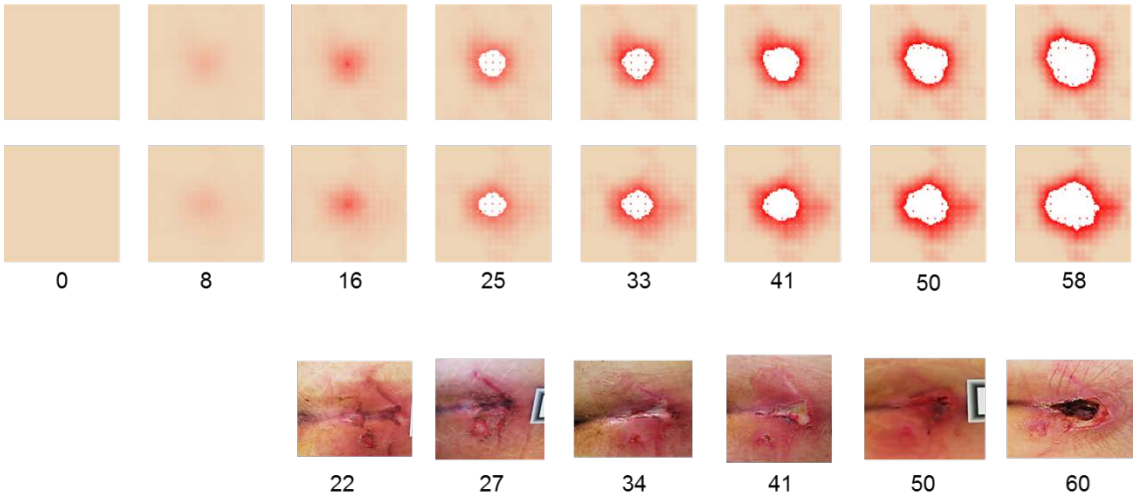

Figure 2.8. Time courses of simulations versus a clinical time course.
Numbers indicate days post-injury. Simulated ulcers evolve with visual characteristics that match PU progression observed in people with SCI. Two simulation time courses are matched against one patient from our study. We match key features: irregular shapes, nearby satellite ulcers, and decreasing tissue health across the field.

2.4.4 Parameter Sensitivity Analysis: the most sensitive parameters in the PUABM are those related to oxygen and TNF-α

It is important to understand the range of behaviors that a computational model can achieve, under what conditions these behaviors appear, and the likely mechanism by which those outcomes are achieved. While the structure of a given computational model can, of course, dictate its ultimate behaviors, much of the behavior of a model can be determined by the values of its parameters (22; 59; 74; 81; 83). Accordingly, parameter sensitivity analysis was carried out in order to gain an understanding of how variations in parameters (including initial conditions, rates, thresholds, etc.) relate to variations in output (time-evolving health of tissue). Since global

parameter estimation can be a computationally daunting task, especially in the setting of stochastic ABMs, the parameter sensitivity analysis herein was focused on defined modules of the PUABM (Fig. 2.9).

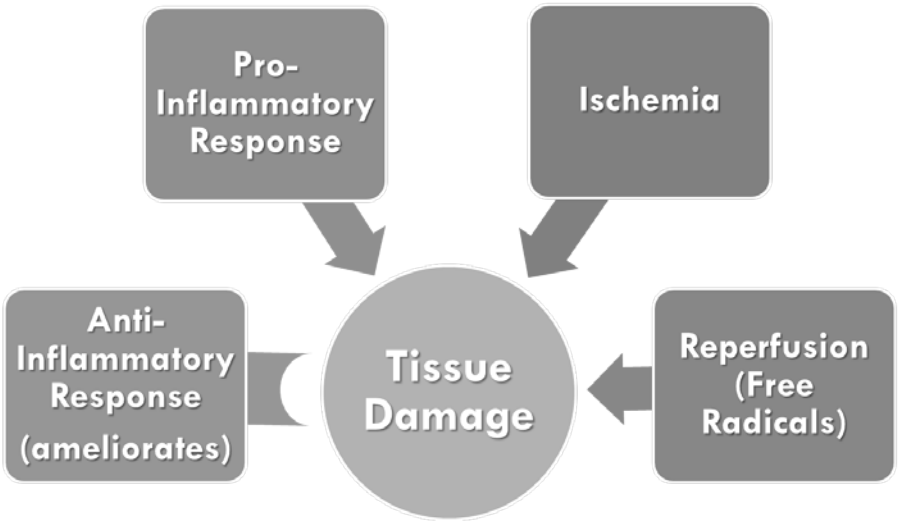

Figure 2.9: Modules for Sensitivity Analysis.
We partitioned parameter values according to which damage mechanism they affected.

Since in the PUABM injury is initiated by repeated pressure cycles, the sensitivity of the model to pressure (Fig. 2.10) was examined first. To do so, the maximum intensity of pressure (applied to the center of the tissue) was varied along with the length of the pressure interval (this number indicates for how many consecutive ticks pressure is applied, equal to the number of ticks during which pressure is removed). At t = 400 h (16 d) of simulated time, very little effect of pressure interval length was observed. However, a slightly lower degree of damage was discerned in the medium-length pressure interval. Pressure intensity appeared to affect tissue health negatively.

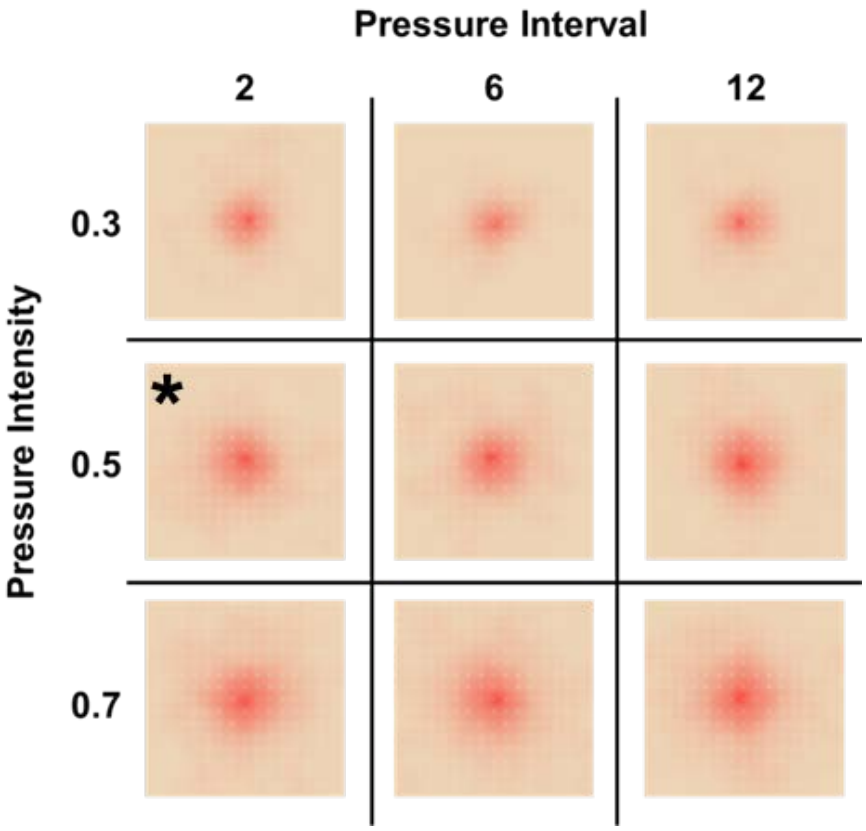

Figure 2.10 Tissue sensitivity to pressure intensity and period.
All sensitivity analyses are shown with model snapshots at time t = 400 h (approximately 2.5 weeks). Pressure intensity varies in each row. Each column represents a value of pressure cycle length. As the cycle length increases, the number of reperfusion events decreases for the same period of ischemia. Increased pressure leads to more damage, while fewer reperfusion events lead to lower damage at t=400 h. Default parameters are marked with asterisks.

Pressure affects tissue oxygen in the PUABM. The impact of oxygen on tissue health was therefore investigated by varying parameters controlling oxygen production (how much oxygen is released from a blood vessel at each time interval) and tissue sensitivity to oxygen (a scalar factor determining the degree to which epithelial cell health is impacted by local oxygen concentrations) (Fig. 2.11). This analysis suggested that when oxygen production is low (or zero), tissue health is severely affected, but in a manner that scales with sensitivity to oxygen. At high oxygen production levels, however, sensitivity to oxygen concentration was not apparent.

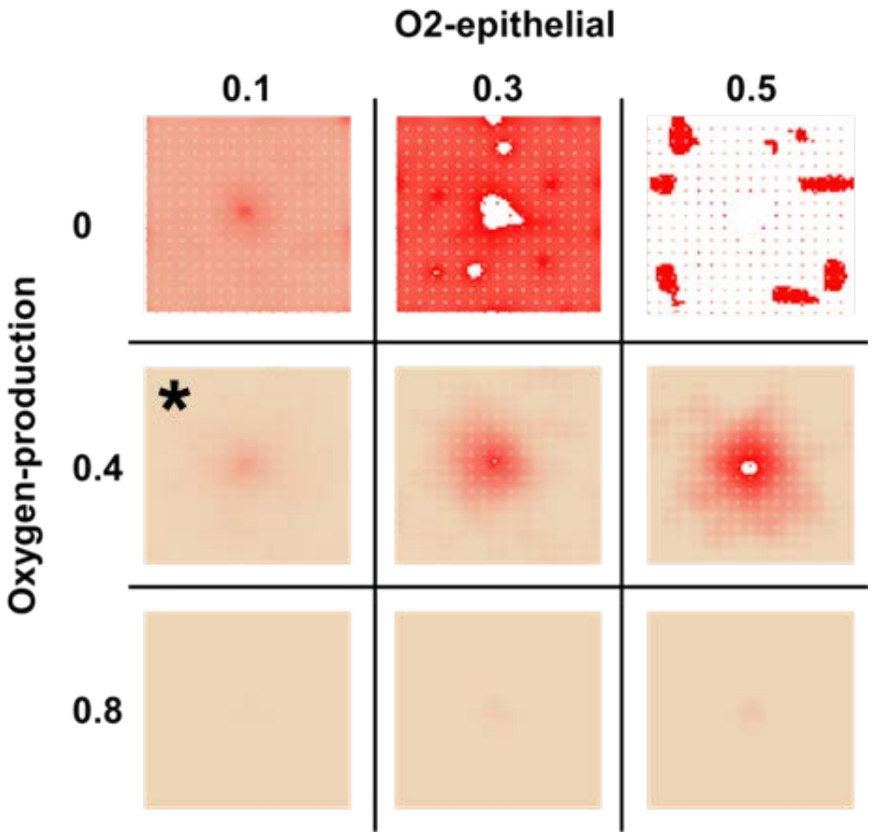

Figure 2.11. Tissue sensitivity to oxygen parameters.
All sensitivity analyses are shown with model snapshots at time t = 400 h (approximately 2.5 weeks). The parameter governing oxygen production varies in each row. Each column represents a value of the parameter controlling how sensitive the tissue is to local oxygen concentrations. When oxygen production is plentiful, the simulated tissue becomes insensitive to other oxygen parameters (bottom row). Default parameters are marked with asterisks.

In a two-way sensitivity analysis, tissue sensitivities to two inflammatory mediators were compared to each other (Fig. 2.12), namely the parameter controlling the model's sensitivity to TGF-β1 (the canonical anti-inflammatory mediator) and the parameter controlling sensitivity to TNF-α (the canonical early-acting pro-inflammatory mediator). Although all simulation snapshots are taken at the same time point, with higher sensitivity to TNF- α, PU appear by t =

400 h (16 d); this does not occur at lower sensitivity to TNF-α. The effect of TGF-β1 is less pronounced, though there is overall less damage as the sensitivity to TGF-β1 increases.

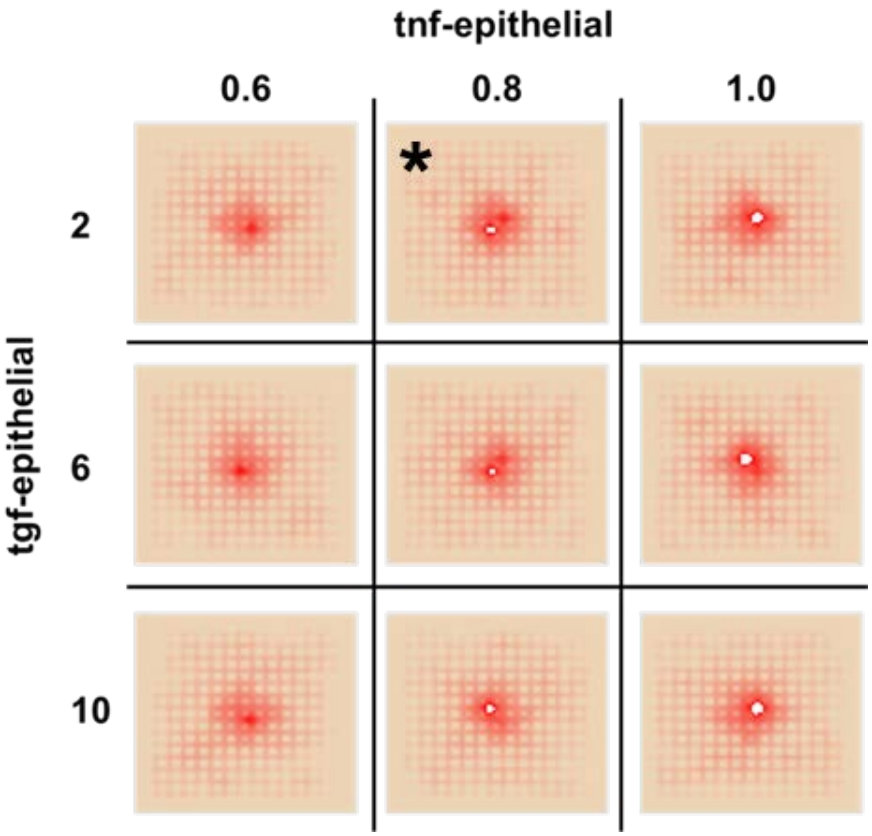

Figure 2.12. Tissue sensitivity to inflammatory mediators.
All sensitivity analyses are shown with model snapshots at time t = 400 h (approximately 2.5 weeks). Each column represents a value of the parameter controlling how sensitive the tissue is to local TNF-α concentrations. The parameter controlling tissue sensitivity to TGF-β1 varies in each row. Increasing sensitivity to TNF-α leads to earlier ulceration and more damage, while increased sensitivity to TGF-β1 leads to decreased tissue damage. Default parameters are marked with asterisks.

The inflammatory response, like most biological processes, is regulated in part through signaling mechanisms that, in essence, define thresholds of activation (67). Accordingly, various thresholds in the PUABM control state changes of inflammatory cells (e.g., when local TNF-α concentration is above threshold, macrophages convert to M1 phenotype.) There is a different

threshold for each state change, as illustrated in Table 2.1 and Fig. 2.2. Sensitivity analysis suggested that the most sensitive threshold was the concentration of DAMPs necessary to activate neutrophils (Fig. 2.13). Most thresholds had a small range over which the output was sensitive to the threshold value, and outside of this range the dynamics were stable. This was not true for thresholds controlling activation of M2 macrophages. For activation by both IL-1β and TGF- β1, as the threshold value increased, so did predicted damage (as expected). However, from the number of simulations we performed (100 per parameter value), there seemed to be a nonlinear relationship between the thresholds of M2 activation and total damage acquired. There were regions in which the output stabilized over a range of parameter values and then at the next higher parameter value, the total damage suddenly rose (Fig. 2.13). This phenomenon could be an artifact of under-sampling, but if not, it suggests a more complex relationship between the number of M2 macrophages and overall damage in the model.

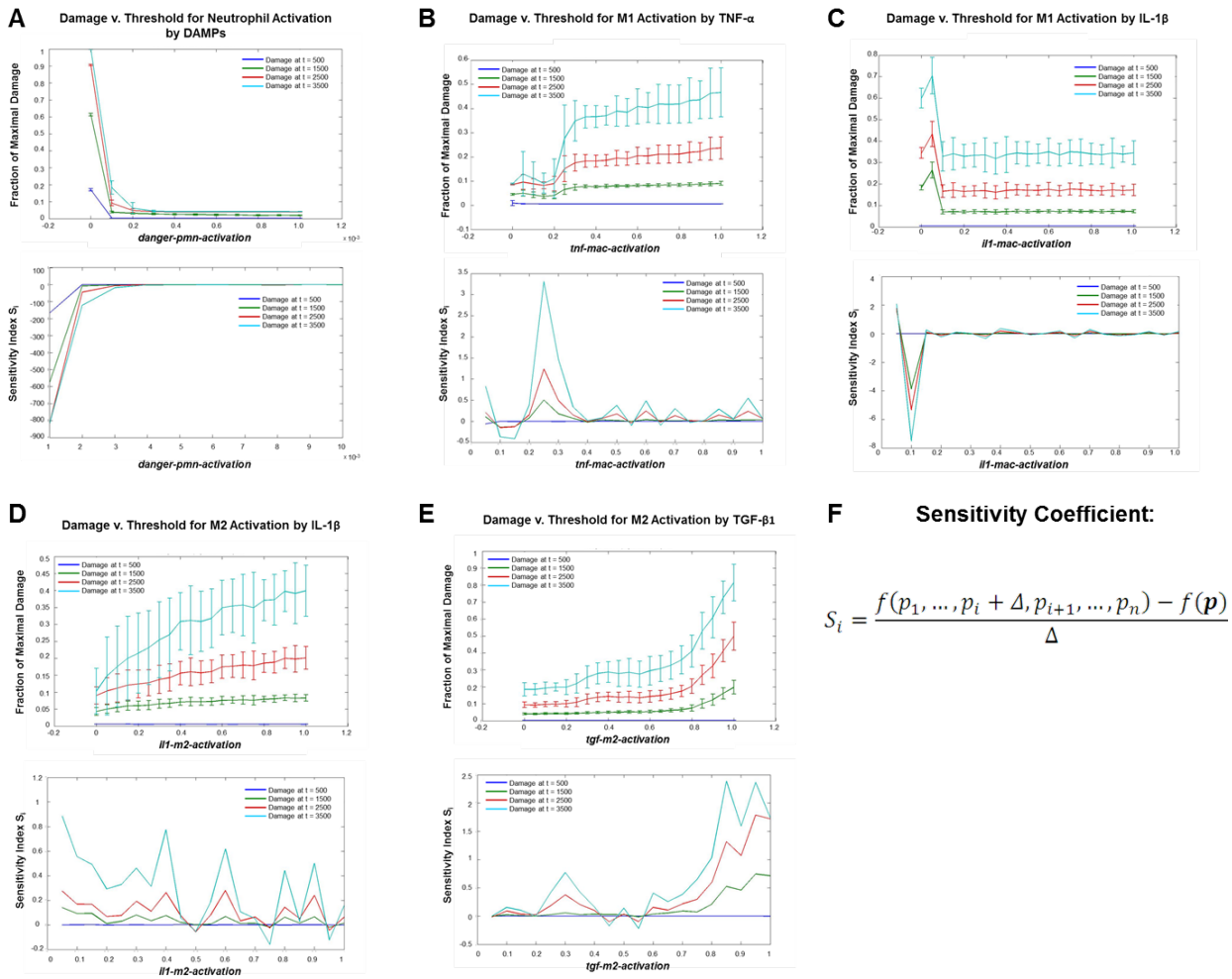

Figure 2.13. Sensitivity Analysis of Inflammatory Activation Thresholds.
(A-E) At every value of each parameter, plotted are data from 100 simulations, each run for 4000 ticks. Values of total damage at four time points in each simulation were normalized by dividing by the maximal possible damage value. Then the mean and SEM was calculated for each parameter value at all four time points. This is plotted in the upper graph of each panel. Sensitivity coefficients were calculated according to the formula given in panel (F). The Sensitivity Coefficient is defined to be the average change in total damage between consecutive values of the varying parameter, divided by the amount by which the parameter changed.

2.4.5 *In silico* Clinical Trials: Reducing inflammation reduces overall Damage, but does not prevent ulceration in the PUABM

In silico (simulated) clinical trials are an emerging means of gleaning translational knowledge from computational models (4; 27; 48; 64). Accordingly, this methodology was utilized to test both current and hypothetical or emerging therapies for inflammation in the setting of post-SCI PU. The feasibility of corticosteroids as a treatment was examined for this indication, varying dose and timing of corticosteroids to investigate whether reducing inflammation could delay ulceration and/or lead to less tissue damage (Fig. 2.14). Corticosteroid administration was simulated as suppressing all inflammatory mechanisms. This was implemented by the following rule: any activated macrophages or neutrophils die upon encountering at least a threshold amount of steroid in their local vicinity of steroid. Corticosteroids led to a reduction of the total damage incurred in a simulation when administered early enough and at high enough doses. However, with pressure cycling PU still formed, suggesting that the lack of inflammation was insufficient to ameliorate the damaging effects of ischemia and reperfusion (Fig. 2.14A).

By comparison, simulations with an initial acute injury but without pressure responded more favorably to steroid intervention (Fig. 2.14B). From qualitative spatial pattern matching, it appeared that any dose of steroid greater than zero was sufficient to achieve the full effect in both cases. There was, however, more damage incurred when the steroid was applied at later times. While overall damage was still less than simulations without steroids, there was noticeably more damage in simulations with later onset of steroids, no matter the method of injury.

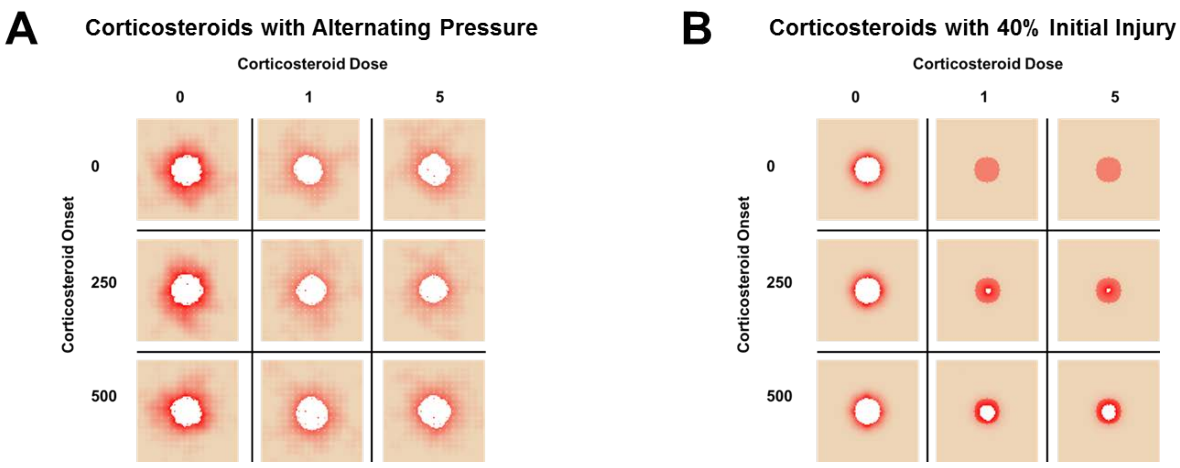

Figure 2.14: *in silico* Corticosteroid Trials.
Simulations are shown at t = 700 h. We varied both the dose and timing of corticosteroid administration, simulated as an injection into the bloodstream, under (A) alternating pressure and (B) 40% initial injury conditions. When inflammatory cells were neutralized early enough but pressure continued, overall damage decreased, but ulceration was not prevented. Without continuous pressure cycles, the earliest dose of steroids was successful in stemming ulcer formation, but later applications did not.

DAMPs such as HMGB1 have become leading therapeutic targets for inflammatory indications (11; 105). Accordingly, dose and timing of anti-DAMPs administration were varied over wide ranges using the PUABM; however, no apparent effect was observed (Fig. 2.15A). This lack of predicted efficacy may be due to a secondary mechanism of neutrophil activation encoded in the model wherein damaged tissue cells can activate neutrophils directly, compensating for the lack of DAMPs. Again, the same treatment was simulated on an initial acute injury without pressure cycles (Fig. 2.15B), yielding similar results.

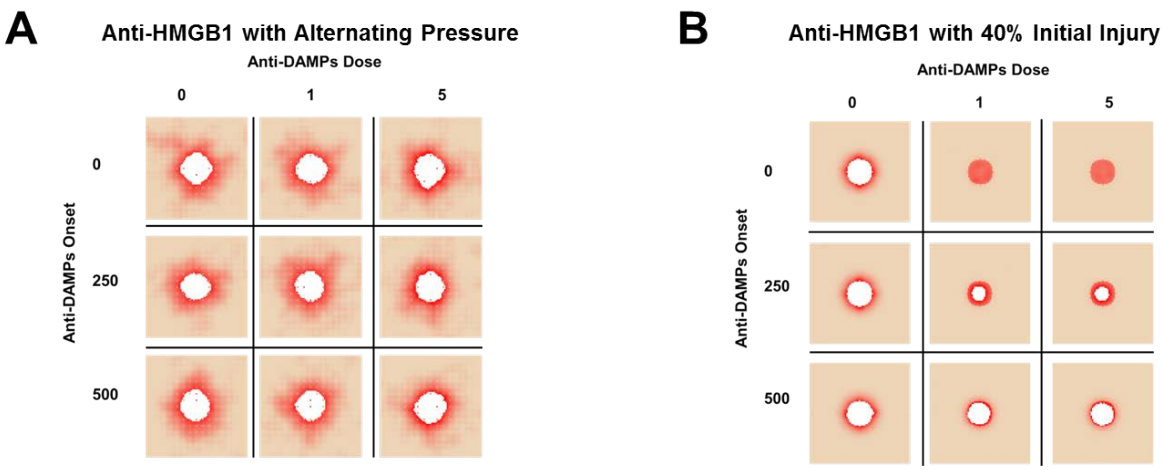

Figure 2.15: *in silico* Anti-HMGB1 Trials.
We then varied both the dose and timing of administration of a neutralizing antibody to HMGB1, simulated as a topical cream applied to the entire field. This targeted approach had (A) no apparent effect during simulations with alternating pressure, but (B) was able to slow ulcer formation after a 40% initial injury without pressure.

2.5 DISCUSSION

The "translational dilemma" centers, in large part, on the inability of traditional, reductionist approaches to yield drug targets for the complex diseases that affect today's patients (5; 10). Systems biology ("-omics") approaches may help identify global system properties and suggest dysfunctional biological pathways that may be serve as therapeutic or diagnostic targets. However, these approaches are limited in the setting such as wound healing. A key limitation is related to the need to obtain material from the affected tissue, and thereby possibly compromise the underlying biological process and impair wound healing. A further limitation is due to the purely associative nature of the bioinformatics tools used to analyze "-omics" data, which limit the ability to extrapolate beyond the conditions used to obtain the data, and also cannot be used to predict the effects of perturbations/therapies (8; 90). Mechanistic computational modeling

offers the possibility of overcoming this limitation, but traditional, equation-based mechanistic models are typically difficult to implement with the kind of spatial realism that could facilitate non-invasive comparison to easily obtained image data. Thus, the ability of ABMs to represent spatial relationships and tissue patterning effects makes this class of models an appealing approach for modeling the biology of wound healing in the context of post-SCI PU. As with other applications of biomedical agent-based modeling, simulations generated by an ABM concerning wound formation and evolution are marked by global, system-level morphological outputs, i.e. spatial patterns with identifiable temporal trajectories. Tracking these morphological features – along with numerical data concerning both the temporal trajectories of individual components (mediators and cell populations) and "experimental/epidemiologic" output derived from performing a series of simulation runs – provide a rich space of output features to which hypotheses can be examined, evaluated, and falsified. This process can lead to the generation of novel, clinically-relevant hypotheses that can then be further examined in an iterative investigatory loop (5; 7).

Herein, we report for the first time on a tissue-realistic ABM of inflammation and wound healing that leads to visual patterns, in a manner that is highly consistent with data obtained from PU in people with SCI. We suggest that this approach of using extensive simulations calibrated against highly-focused clinical data holds the potential to streamline subsequent *in vitro*, *in vivo*, and clinical studies (9).

Tissue-realistic simulations incorporating mechanistic information present multiple possibilities at the bedside. The visual output of models such as this one, along with the capacity to use the models for *in silico* clinical studies as we show here, lends itself naturally to both diagnostic and drug development applications in which the outcome is often a visual pattern

(wounds and other skin lesions [e.g. psoriasis, melanoma], histological and immunohistological biopsies, and other medical imaging modalities [e.g. MRI, CAT scan]). After augmentation and appropriate additional verification (see below), the model may eventually be used to identify individual wound healing phenotypes and trajectories, determine appropriate treatment course, and design and test new treatment regimens.

The design and execution of clinical trials involving multiple concurrent interventions all being evaluated at differing dose and dosing levels, is extremely challenging at best, and logistically unfeasible in most cases. For complex inflammatory diseases, *in silico* clinical trials could help guide and streamline the selection of therapies and their implementation in randomized clinical trials (91; 93). Herein, clinical trials of an established anti-inflammatory agent (corticosteroids) as well as a novel therapy currently in clinical trials (neutralizing anti-HMGB1 antibodies) were carried out *in silico*. Though leukocyte inhibition has been shown to reduce I/R injury and PU formation in rats (71), these *in silico* studies suggest only a limited efficacy for corticosteroids, in line with prior studies (31; 56). Neutralizing anti-DAMP antibodies have also been suggested as potential therapies for acute inflammatory diseases, though not for wound healing disorders. In the setting of post-SCI PU, our studies suggest that anti-DAMP antibodies are unlikely to be efficacious for this indication, as may be anticipated from the known role of DAMPs such HMGB1 in promoting wound healing (73; 88; 104). Our preliminary results based on sensitivity analysis do, however, point to wound oxygenation as a potentially efficacious therapeutic approach for post-SCI PU. Hyperbaric oxygen therapy has been shown to be beneficial in healing many types of chronic wounds (47). Paradoxically, however, in studies with PU, hyperbaric therapy has not shown significant effects (47). It may be that the damage incurred in the settings PU also affects vasculature to the point that they are

unable to take up oxygen from the environment. In this case, alternate strategies to deliver oxygen to the wound—perhaps a more directed, local application rather than hyperbaric oxygen to be delivered via the overall circulatory system-- could be considered.

There are various limitations to this study. An inherent limitation to modeling is the resolution of detail included in the model. The mechanistic information used to inform the rules of the PUABM was relatively high-level. For example, we used single mediators to represent the actions of entire pathways. These choices were made because the nature of ABMs is such that each mechanism could be computed in any given cell at any given tick. It is the sum of these parsimonious mechanisms as they are simulated across space and time that gives rise to the behaviors of the model. Including too much detail causes simulations to run slowly and on the whole may not add much insight on the whole-tissue level. Furthermore, the more details, the more difficult the calibration process is. It is a delicate balancing act for the modeler to include enough mechanism for the model to be relevant without including too much noise. A related limitation concerns the fact that the PUABM is a two-dimensional abstraction of a three-dimensional layer of tissue above a bony prominence (17; 19) (i.e. simplifying the complex environment thought to lead to PU formation). Studies have shown that various tissue layers (skin, muscle, bone) have differing susceptibility to nutrient deprivation and other adverse effect of pressure loading (e.g., muscle is more susceptible than skin) (17; 19). However, the tissue simulated in this model represents an abstracted, composite tissue which responds in a way that is more general than any individual layer, but still produces the same dynamics observed clinically. Recent work has also suggested an important contribution of strain and tissue deformation in the development of pressure ulcers and deep tissue injuries (20; 51). The two-dimensional nature of the PUABM prevents full exploration of these phenomena, though they

are necessarily linked to ischemia/reperfusion events. Nonetheless, the simulated tissue was able to achieve a range of appearances matching the appearance of ulcers at various severities in clinical photographs (Fig. 2.7).

Another limitation concerns the availability and frequency of clinical data, especially in the earliest stages of ulceration. Given the fleeting nature of tissue edema/redness, it was very difficult to obtain images of ulcers in Stage I. Therefore, we cannot be as confident regarding the validity of the dynamics of our model in the early phases of each simulation. Complicating matters further is the fact that the people with SCI in our study received care for their wounds, including debridement of necrotic tissue and thus removal of inflammatory stimuli, as well as the presence of other injuries sustained or complications of traumatic SCI. In parameterizing the PUABM, we utilized population averages regarding time to formation of PU, and some of our parameters may reflect these treatments. This may also explain why other studies tend to find a shorter average time to ulceration (3; 40). Another contributing factor is that we defined "ulceration" as the moment when the first tissue cell dies, signifying opening of the PU. In reality, this could represent a partial thickness Stage II ulceration, but may be more consistent with a full thickness Stage III PU with loss of dermal cells. Thus, either a Stage I PU or even a deep tissue injury could have already been present. Indeed, the time required to develop a Stage I ulcer is quite short (12 ± 5 h) in our simulations, and thus may, in actuality, match reported time scales. In the model, any small amount of damage – whether or not this damage is sufficient to incite inflammation – does not heal. In the clinical setting, this small amount of damage may not be severe enough to stimulate intervention, and as a result may progress or fail to heal.

The PUABM could be augmented to increase its realism and translational utility by simulating standard interventions such as debridement (as we have done in our diabetic foot

ulcer ABM) (64), as well as routine complications such as bacterial colonization or infections. In addition, the emergent/stochastic phenomenon yielding the possibility of worsening or non-worsening inflammation subsequent to a single injury from one set of parameter values is promising for several reasons. First, this variance mimics the variability observed clinically, wherein two patients may present with similar disease states, receive the same treatment, but have quite different ultimate outcomes. The PUABM allows us to query the cause of this bifurcation, which may yield further diagnostic or therapeutic utility.

In conclusion, our studies demonstrate the potential utility of tissue-realistic ABMs as a platform for mechanistic inquiry and translational application. Given the dire need for new therapeutic avenues for complex diseases, we suggest that a platform combining *in silico* approaches with clinical samples, especially images that can be obtained readily and inexpensively, may yield novel diagnostic and therapeutic modalities.

3.0 ANALYSIS OF AN AGENT-BASED MODEL TOWARD CLINICALLY–RELEVANT INSIGHTS

3.1 ABSTRACT

As a wound progresses, it develops morphological features that may be indicative of the wound's trajectory. In an ABM, wound formation and evolution is marked by morphological outputs of the model. These morphological features -- along with numerical data also generated during simulations -- provide a rich space of output features to which hypotheses can be linked. In this chapter, we explore methods to take advantage of model outputs to learn how and when outcomes are determined. From this information, new treatment strategies can be designed.

3.2 INTRODUCTION

To design treatment strategies for pressure ulcers, we sought a more specific understanding of pressure ulcer formation aided by the pressure ulcer ABM described in Chapter 2. We have shown that in total, the two mechanisms we encoded in the model (I/R injury and acute inflammation) are each capable of inducing significant tissue damage. From a clinical standpoint, however, a good treatment strategy targets one specific piece of a given mechanism. To identify which individual parts of the model have the most influence over its outcome, we examined the

effects of individual model parameters including initial conditions, rates, thresholds, etc. We next wanted to relate the model parameters to outcomes in an analytical way, so that we have a quantitative basis for comparing the effects of each parameter. Understanding the space of parameters that leads to one outcome or another also gives information about the mechanism by which those outcomes were achieved. Similarly, the parameters that can account for the greatest portion of variance in model outputs either are linked to the dominant mechanism of action in the model or are encoded in a way that places undue emphasis on that mechanism. It is important to understand the range of behaviors that a computational model can achieve and under what conditions they appear. It is important to identify these parameters and then make the determination as to whether or not the rules are 'fair.' If so, then we can have more confidence that the outcomes are realistic. Because all models are abstractions of reality, formal model analysis is essential to measure confidence in model predictions. We would like to understand how variations in parameters (including initial conditions, rates, thresholds, etc.) relate to variations in outputs (time-evolving health of tissue). Therefore, we would like to develop a quantitative mapping from model inputs to model outputs, estimating the range of output values given the range of input values.

Stochastic models bring with them an extra layer of uncertainty (given the same set of parameters, we may have a distribution of outputs due to stochasticity in the model). This is termed aleatory uncertainty, while the variation caused by varying inputs is epistemic uncertainty. To characterize this relationship, it is necessary first to separate aleatory from epistemic uncertainty. Then, we can characterize each of these phenomena separately, proceeding with the epistemic uncertainty as we would with a deterministic model. As we have

already explored epistemic uncertainty in the previous chapter, this chapter will focus on aleatory uncertainty.

The fact that we see not only a range of outcomes but two distinct phenotypes arising from a singles set of parameter values suggests that the aleatory uncertainty not only introduces noise, but also causes meaningful transitions between health states. We will harness this stochastic bimodal variation as powerful information content to understand the dynamics of the system and design effective treatments. This variation mimics variation in a population of patients who may present with the same intensity of disease, receive the same treatment, but experience very different disease progressions. We have found that the two types of outcomes we observe *in silico* strongly correlate with characteristic simulated trajectories of inflammatory cells. In figures 2.3-4, notice that the simulation with a resolved inflammatory response has almost no active neutrophils in the second half of the simulation. By contrast, in the simulation with maladaptive inflammation, after being initially activated all of the inflammatory cells remain engaged throughout the remaining time course. This observation could be key to understanding the divergence between resolving and maladaptive inflammation in our simulations. Indeed, there is evidence of existence of "tipping points" in other settings of acute inflammation, where a system crosses some threshold and becomes committed to one outcome or another, even before physiological symptoms would predict such inevitability (8; 30; 68). According to the inflammatory cell trajectories mentioned above, it would seem that the model is already committed to its severity of outcome well before an ulcer forms.

To examine how this might arise stochastically in the model, we collected inflammatory trajectories and other data from simulations, and used this as a feature set to train a classifier for tissue health outcomes. We wanted to use sequences of state variable values to predict which

outcome a simulation would reach. Next we wanted to know how early in a simulation that prediction could be made without loss of accuracy. With this determined we tested our classifier by determining at what point the decision had really been made. Saving all internal model variables allowed re-simulation under precisely the same conditions from any arbitrary point in a time course. By starting at various points along the way, we could see how early every single re-simulation reached the same outcome class as the original simulation. This greatly narrows the time window in which the divergence decision is made, limiting the number of features necessary to consider when determining a predictor. This is helpful because the predictor is likely more nuanced than the total concentration of one or two state variables; more detailed spatial and/or temporal features may play a role.

At the end of this chapter, we also begin the exploration of global sensitivity analysis by examining the qualitative effects of three injury mechanisms: ischemia, reperfusion, and acute inflammation. We develop some surprising insights about how each mechanism affects qualitative outcomes.

3.3 RESULTS

3.3.1 Quantitative Characterization of Bimodal Behavior

In Chapter 2, we observed that simulations could reach two distinct endpoints, even when initiated with the exact same parameter values. This behavior, we reasoned, must arise due to stochasticity within the model. The behavior was most prominent in simulations of the acute

inflammatory response in the absence of pressure, but was also noticeable when pressure cycles were applied (Fig. 3.1).

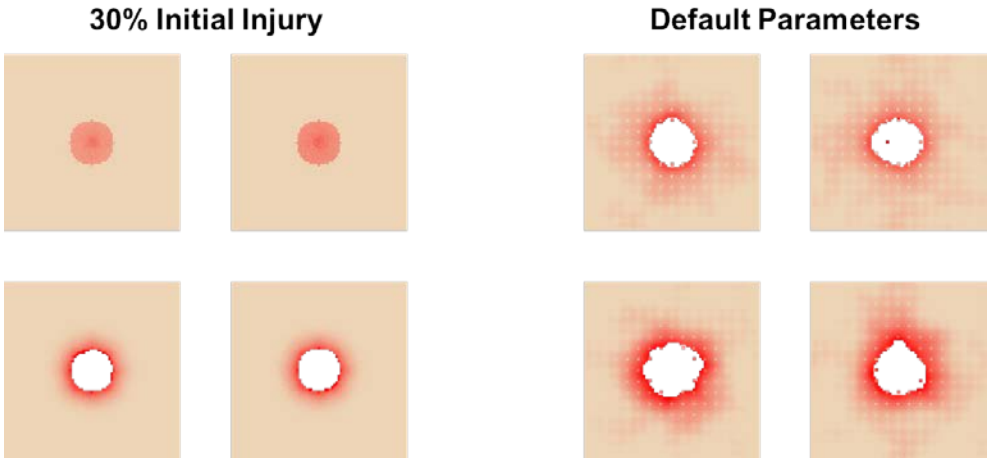

Figure 3.1. Snapshots at t=1000 showing two distinct outcomes for each set of parameter values.
Eight independent simulations are represented here. Snapshots are arranged with lower damage simulations in the top row, for visual impact. All 4 snapshots on the left arose from the same set of parameters involving 30% initial injury to the center of the tissue and no pressure cycles. Similarly, all four simulations on the right arose from the same set of default parameter values, including pressure cycles and no initial injury.

3.3.1.1 Acute Inflammation Incited by Initial Injuries of Varying Degree

In simulations of acute inflammatory dynamics, the intensity of initial injury was correlated to the frequency of ulcerative inflammation (as opposed to resolving inflammation). With a 40% initial injury, ulceration was virtually guaranteed whereas a 25% injury only led to ulceration in approximately 10% of simulations (Fig 3.2). In order to study the dynamics controlling this switch, we focused on simulations with a 30% initial injury, which yielded ulcerative inflammatory dynamics in almost 50% of simulations.

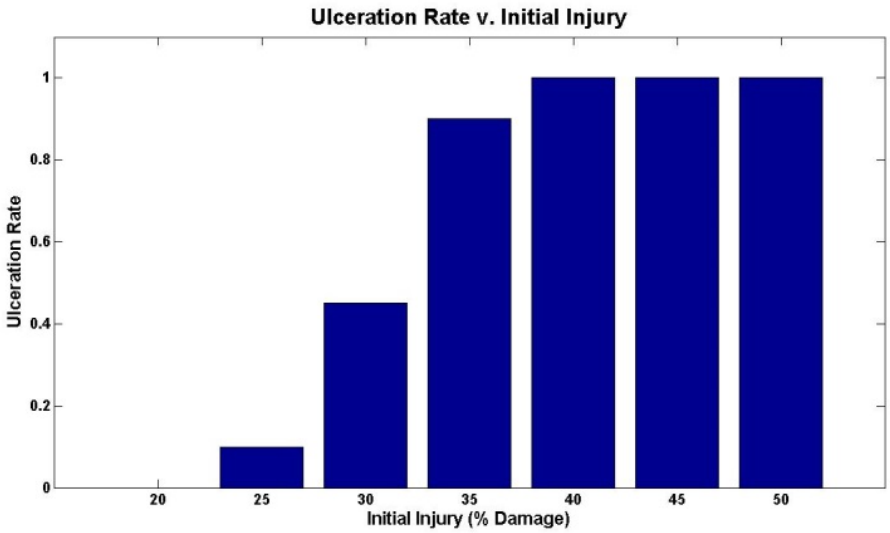

Figure 3.2. Ulceration rate for various amounts of initial injury, without pressure.

3.3.1.2 Acute Inflammation Incited by a 30% Initial Injury

Ulceration was defined as having at least one dead tissue cell. Therefore, counting live tissue cells gave an indication of whether a simulation had reached ulceration or not. With these simulations where the two endpoints are so drastically different, tissue damage levels were also indicative of ulceration status.

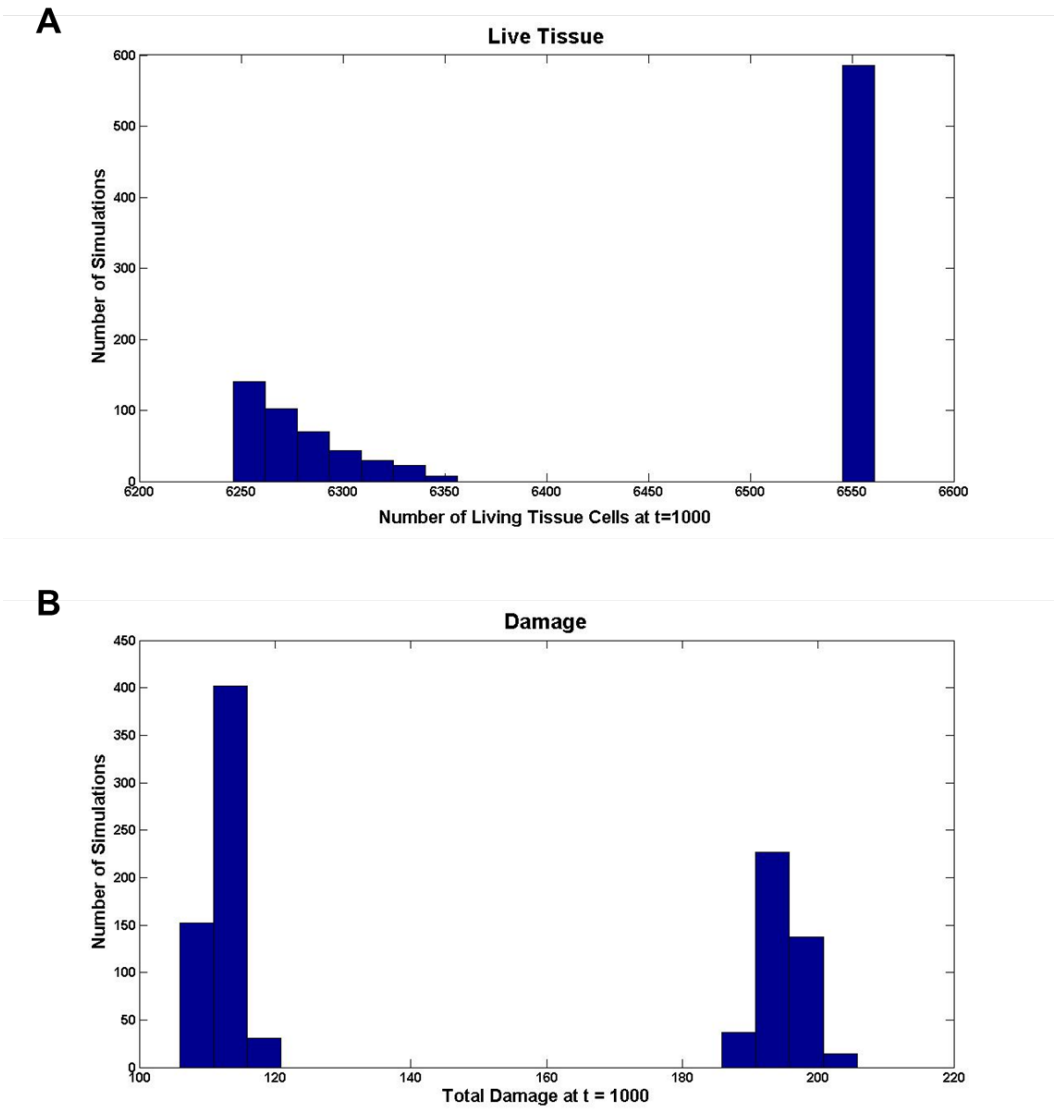

Figure 3.3. Histograms of number of live tissue cells and total tissue damage at t=1000.

The distribution of simulations reaching each endpoint was approximated using the damage distribution as the input to the Matlab® function, *gmmfit*. This step is unnecessary with two peaks that are so cleanly separated, but becomes necessary with default parameters, where the endpoints are not so far from each other. Using the Expectation-Maximization (E-M) algorithm, a mixture of two gaussians was approximated using 500 measurements of tissue

damage at t=1000. For visual comparison, the probability density function (PDF) estimated by kernel smoothing (using uniform bandwidth) was overlaid on the Gaussian Mixture Model (GMM) result.

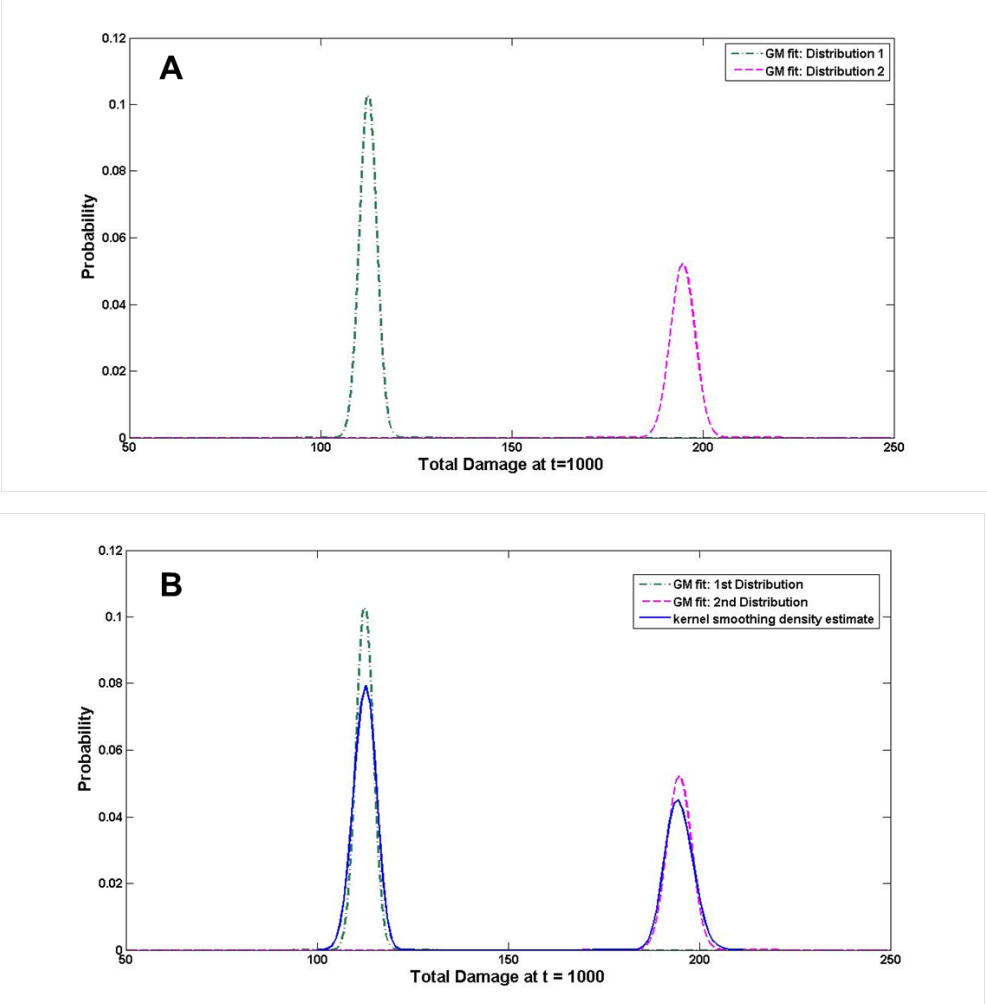

Figure 3.4. Approximation of PDF of Damage using Gaussian Mixture Models and Kernel Smoothing Estimation.

3.3.1.3 Bimodal Behavior in Simulations with Pressure Cycles and Default Parameter Values

Qualitative visual comparison suggested that the multiple-endpoint phenomenon was also present in simulations where pressure was applied. The endpoints were not as discrete as above, due to addition damage caused by ischemia/reperfusion injury. Therefore, ulceration was no longer a defining outcome, as all simulations under these parameters led to an ulcer. What appeared to be different, however, was the amount of damage to the tissue surrounding the ulcer. Reducing this damage would be a desirable clinical outcome because it may protect a patient against further spread of that ulcer and/or lower the risk of developing secondary ulcers in nearby tissue. Histograms of live tissue and total damage at t=1000 illustrate the complexity of this problem (Fig 3.5).

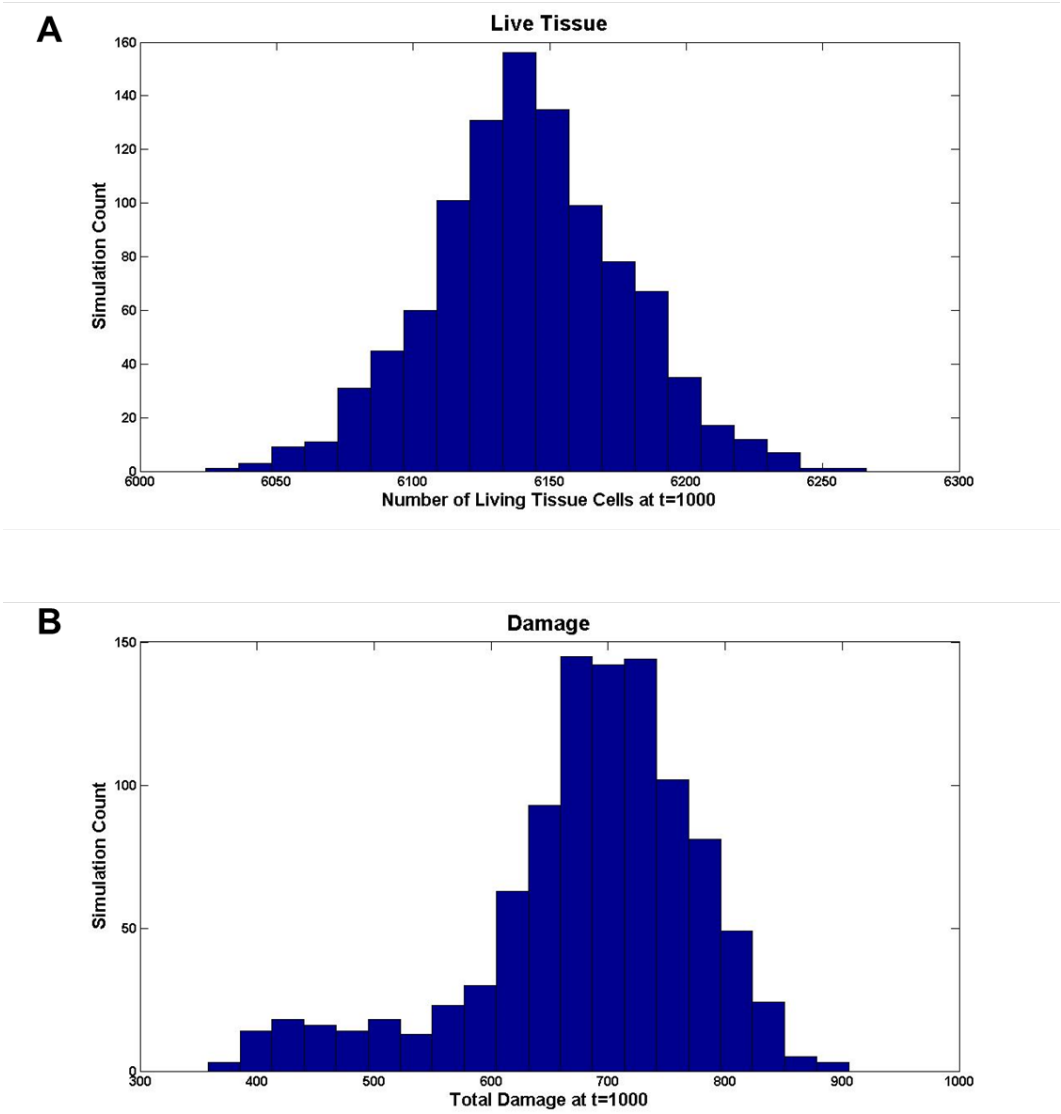

Figure 3.5. Histograms of Live Tissue Cells and Total Damage at t=1000 with default parameters (including pressure cycles).

We first needed to determine the best estimate for how many separate endpoints are represented in the histograms above. We again used E-M to fit GMMs to the data. This time, however, we allowed the number of Gaussian distributions in the mixture model to vary from 1 to 4. We selected the model that was a mixture of two independent Gaussian distributions

because it yielded the lowest scores for both Aikikae Information Criteria (AIC) and Bayesian Information Criteria (BIC), shown in Table 3.1.

Table 3.1. Information Criteria for fitting a mixture of 1-4 Gaussians to the Total Damage data for Default Parameters.

	Number of Independent Gaussians			
	1	**2**	**3**	**4**
AIC	11959.9	11723.8	11728.9	11735.1
BIC	11969.7	11748.4	11768.2	11789.1

Plotted below are the peaks estimated by the mixture of 2 Gaussians model, and on the right the kernel-smoothed estimate is overlaid for visual comparison (Fig 3.6). Notably, the mixing proportions of these two distributions are different than for the acute inflammation simulations. The smaller damage outcomes occur in only approximately 10% of the simulations.

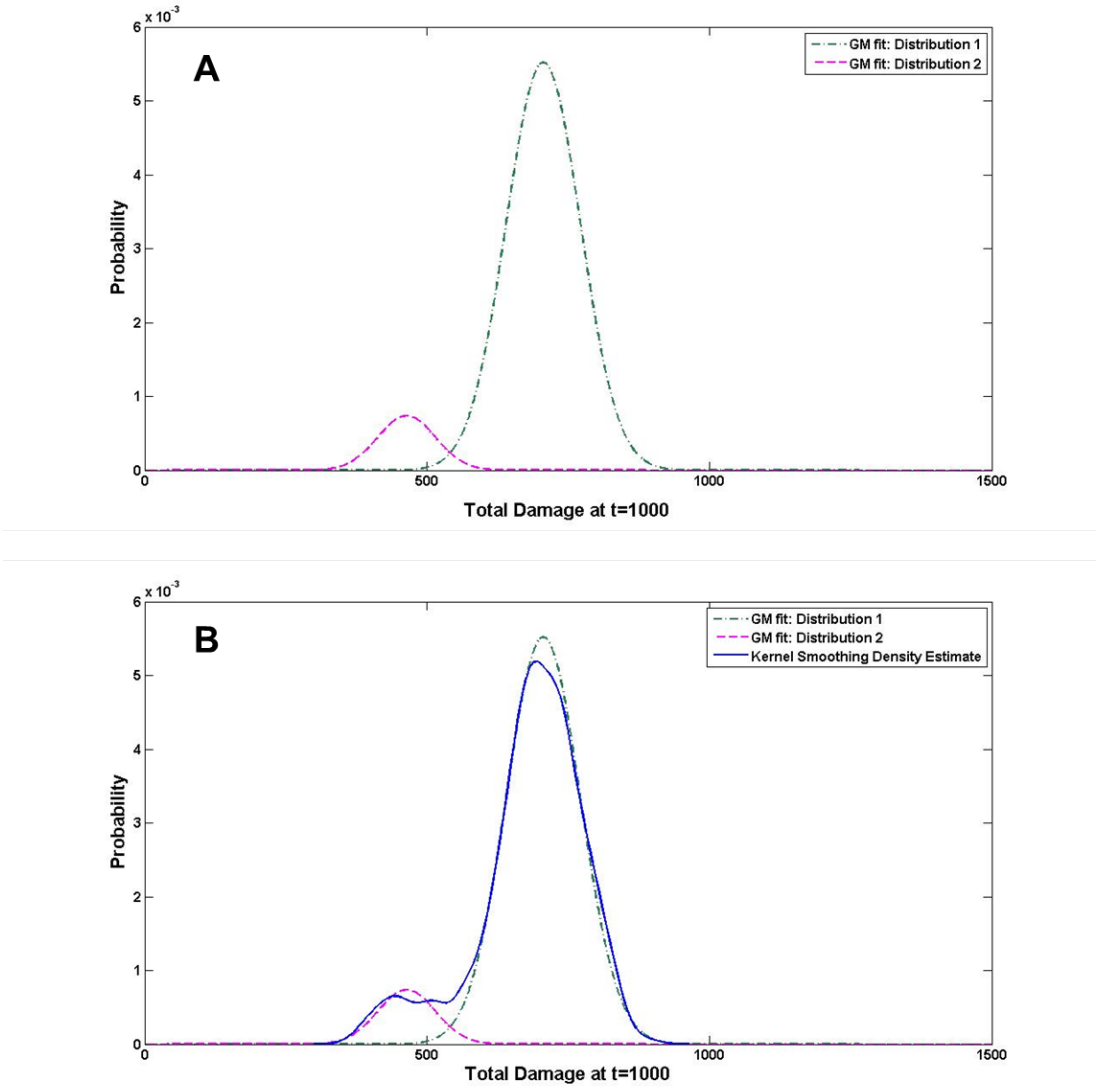

Figure 3.6. Approximate pdfs of Damage, as estimated by GMM and Kernel Smoothing.

3.3.2 Source of Bimodal Behavior

3.3.2.1 Problem and Approach

Now that we verified that the bimodal behavior is quantifiable, we would like to determine which variables in the model are most predictive of outcome. Our first approach was to take advantage of the time-dependence of our data by framing the problem as a sequence

classification problem. Following the work of Xing et al., (101; 102) we employ a 1-nearest neighbor approach. We measure the distance between two sequences by summing the Euclidean distances between corresponding time points on the two sequences. A new unlabeled test sequence is assigned the same class label as the training sequence that is closest in distance to it. With sequences the length of a full simulation (1000 ticks), a relatively good prediction accuracy can be expected. The goal of the work of Xing et al. was to determine the "minimum prediction length" or the time point before which accuracy begins to decrease. We also look for this time point, and use it as an indication of the time by which the simulation is committed to one outcome or another. One last modification was to consider shorter prefixes. Because the simulations are not committed from the very beginning, the early parts of a time course might add unhelpful noise. We compare performance of the 1NN classifier using full length prefixes to the same using prefixes less than or equal to 50 ticks in length.

3.3.2.2 Feature Selection

The data on which we hope to base a classification was collected during simulations of acute inflammation, without pressure. At each tick, recordings were made of total amounts of each mediator, oxygen, and tissue damage, counts of each type of activated cell, etc. We also recorded spatial information for these variables—a lower resolution grid with local concentrations of each of the total measurements mentioned above. Figure 3.7 shows time courses of the total variables, color coded for simulation outcome. These time courses revealed distinct patterns for simulations leading to either endpoint.

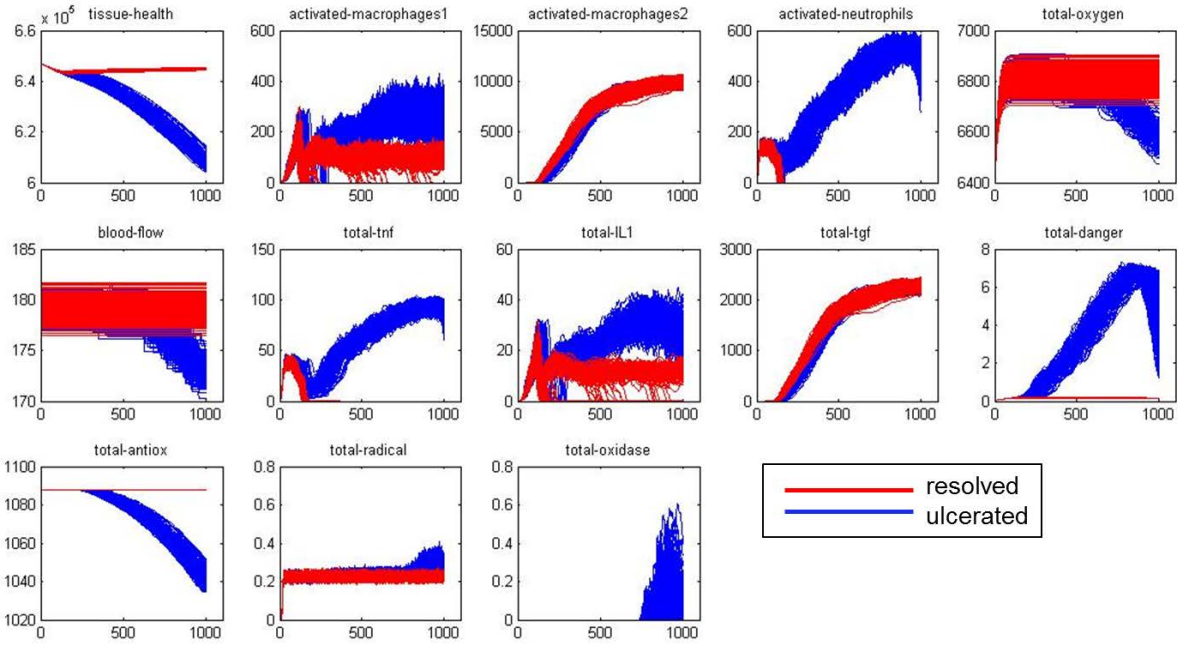

Figure 3.7. ABM state variables in resolving and ulcerating simulations (full timecourse). Features plotted for simulations starting from 30% initial injury that resolved or resulted in an ulcer.

Before endeavoring to extract features from time courses of spatial patterns, it seemed prudent to see how well the classifier could perform using the lower dimensional time courses of total counts. These are the time courses plotted above and below. We notice that a few features have patterns that differentiate between ulcerated and resolved simulations early in the time course. Re-plotting the features for only the first 200 ticks, it becomes more apparent that some features will be more informative than others, especially in making predictions as early as possible. The features: total-oxygen, blood-flow, total-antiox, total-radical, and total-oxidase do not appear to differentiate between endpoints at all, while activated-neutrophils, total-tnf, and total-danger seem promising, especially between 100 and 200 ticks.

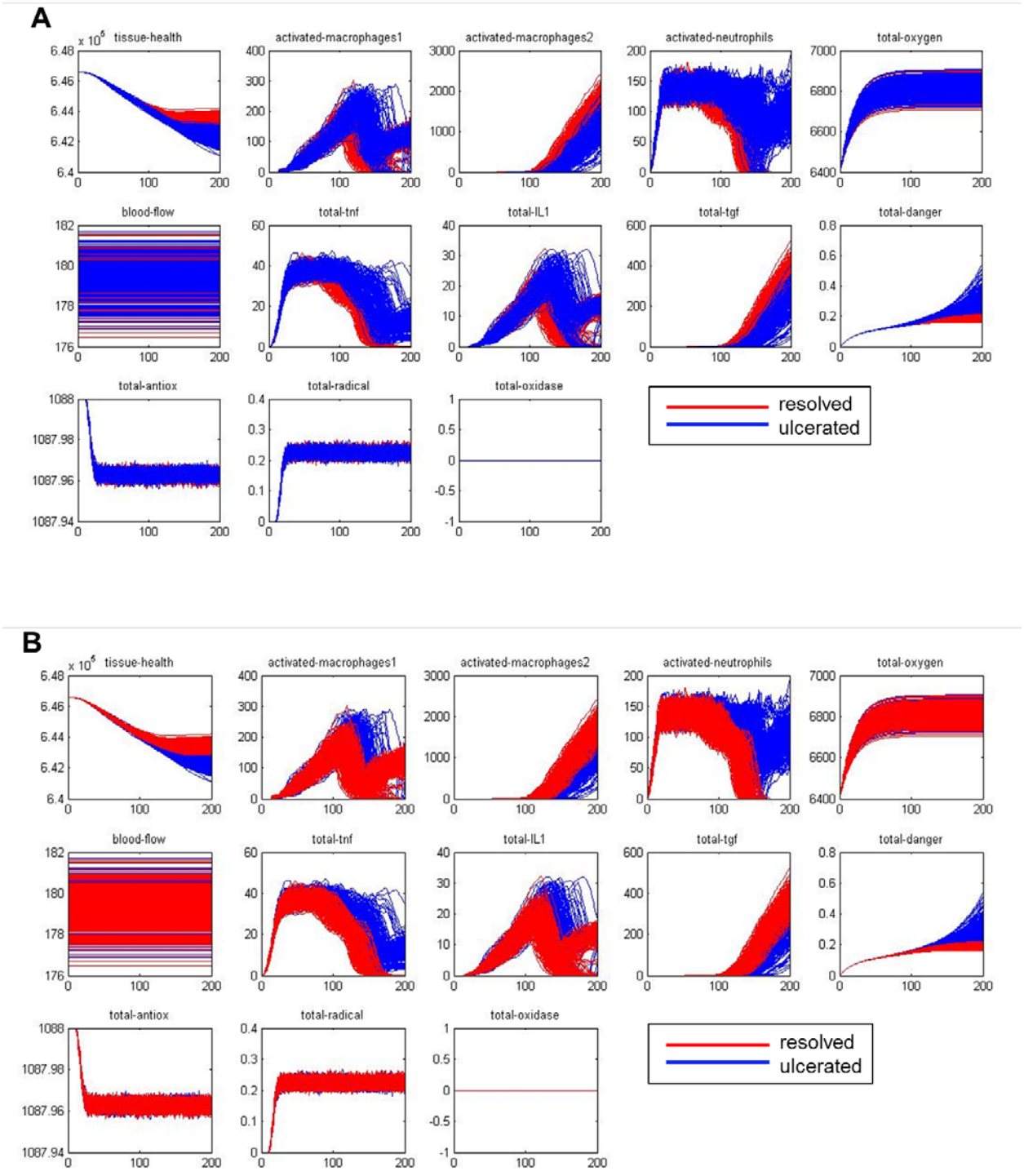

Figure 3.8. ABM state variables in resolving and ulcerating simulations (t = 0-22).
Features plotted for only first 200 ticks. Upper panel A plots ulcerated simulations in front of resolved; lower panel B plots resolved simulations in front of ulcerated.

3.3.2.3 Nearest Neighbor

To take advantage of the time dependence of the features, a nearest neighbor classification scheme was adopted. The training set consisted of data from 100 simulations, labeled according to which endpoint was reached. For each simulation in the test set, a pairwise distance was computed between itself and each simulation in the training set. The simulation in the training set with the shortest distance to a test simulation was called its "nearest neighbor" and the label was shared between the two. This method obviously relies heavily on the choice of distance metric, here Euclidean distance. The length of the vectors (number of time steps included) is called the prefix. When using this method to make predictions, the goal is to get the best possible classification with the shortest prefix. For univariate time series, we simply calculated the Euclidean distance between each pair of vectors consisting of measurements of a single feature through time. For multivariate time series, we calculated the Euclidean distance between two feature vectors at each time step and took the Euclidean norm of those distances to be the distance between the two simulations. To equalize the contributions of all features, their values were normalized to fall into similar ranges before calculating distance.

The following graphs show the classification error rate of the 1-Nearest Neighbor (1NN) Classifier trained on various subsets of the features for the first 200 ticks (fig 3.9). The first step was to assess the predictive power of each feature individually. While classification error ranged, it never stabilized, and no single feature achieved an acceptably low error rate. This figure also makes plain which features are not informative at all.

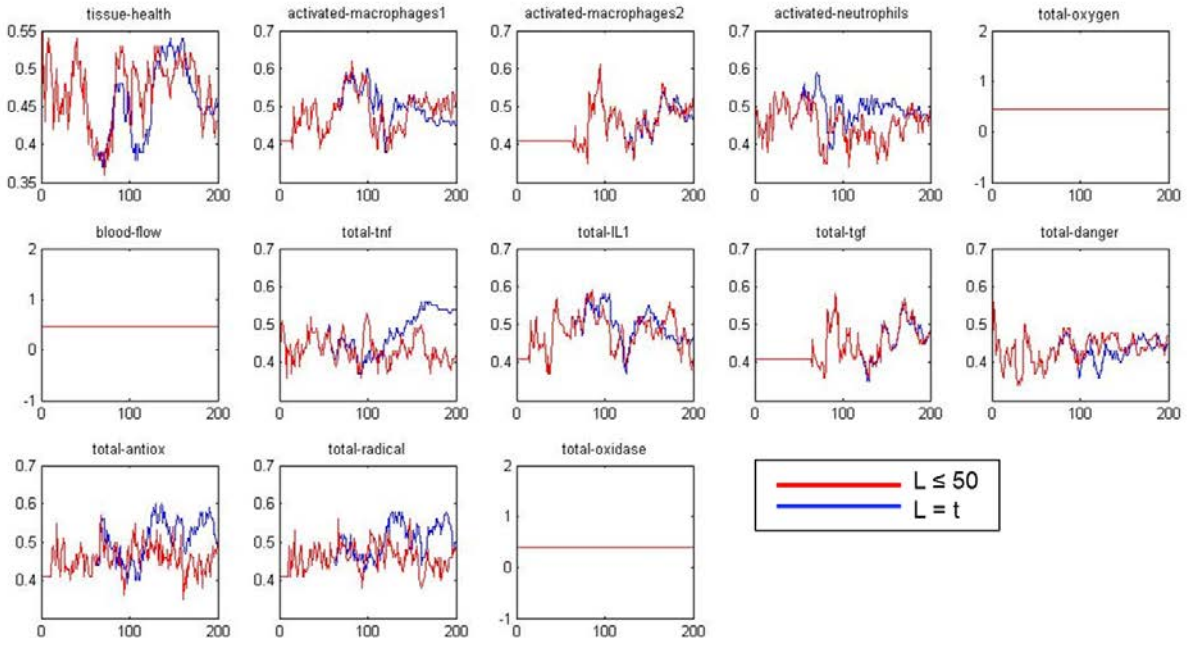

Figure 3.9. Classification Error of 1NN Using Univariate Time Series.
For each feature, there are two plots. In the foremost (red) the prefix was limited to 50 ticks, at most. For these cases, we included ticks [t-49, t]. In the blue, the prefix was left as long as the tick.

We next repeated the classification, incorporating information from multiple features into each time series (a multivariate time series). We assessed the performance of 1NN using a) all 13 features, b) 8 features that were not inert across the first 200 ticks (all but total-oxygen, blood flow, total-antiox, total-radical, total-oxidase), and c) 3 features that appeared to differ the most among the two outcomes before 200 ticks (activated-neutrophils, total-tnf, total-danger). While removing inert features did not appear to improve performance, pruning to only 3 features did (fig.3.10). We expected to achieve a perfect classification because there was complete separation between the two peaks and by 200 ticks we had achieved 0% error rate using 1NN with total-tnf, total-danger, and activated-neutrophils.

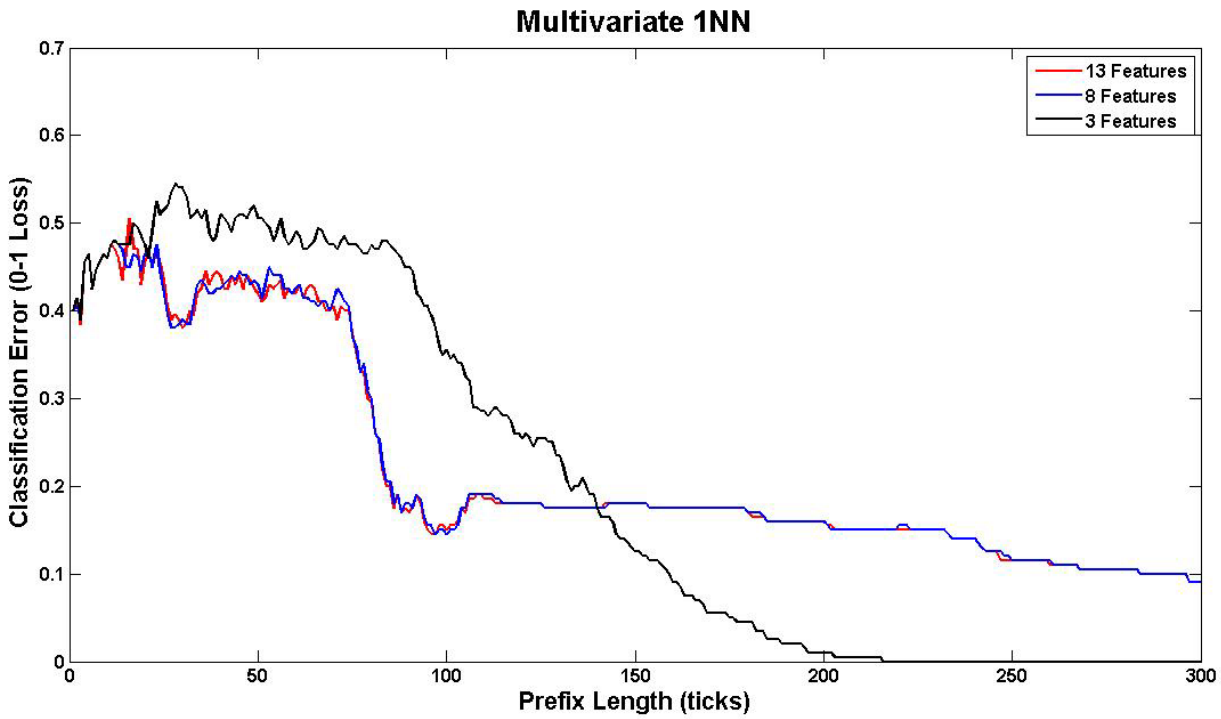

Figure 3.10. Classification accuracy of 200 simulations using a 1-Nearest Neighbor approach, trained on 100 simulations.
The features included in each classifier were as follows: Red – 13Features – all; Blue – 8 Features – total-damage, activated-macrophages1, activated-mcrophages2, activated-neutrophils, total-tnf, total-tgf, total-il1, total-danger; Black – 3 Features – activated-neutrophils, total-tnf, total-danger.

3.3.3 Verifying Earliest Decision Point: Re-simulations

To determine whether 1NN truly identified the decision point in the model, we used the power of simulation. For ten simulations (five resulting in ulcers and five resolving), we recorded all simulation variables every 25 ticks until t=200. Then, starting from each set of saved simulation variables, we initiated 20 simulations and carried them out for 500 additional ticks. In these simulations we recorded the same features as above. This yielded 100 simulations from each starting tick from variables in resolving simulations and another 100 simulations starting from each point in ulcerating simulations. The ulceration status of each of these new simulations was noted, and histograms were plotted for each starting tick (see Figs. 3.11 and 3.12). Contrary to

the results from 1NN, the simulations seem to be determined before t=125. In all but one source simulation, all re-simulations were correctly decided by t=100.

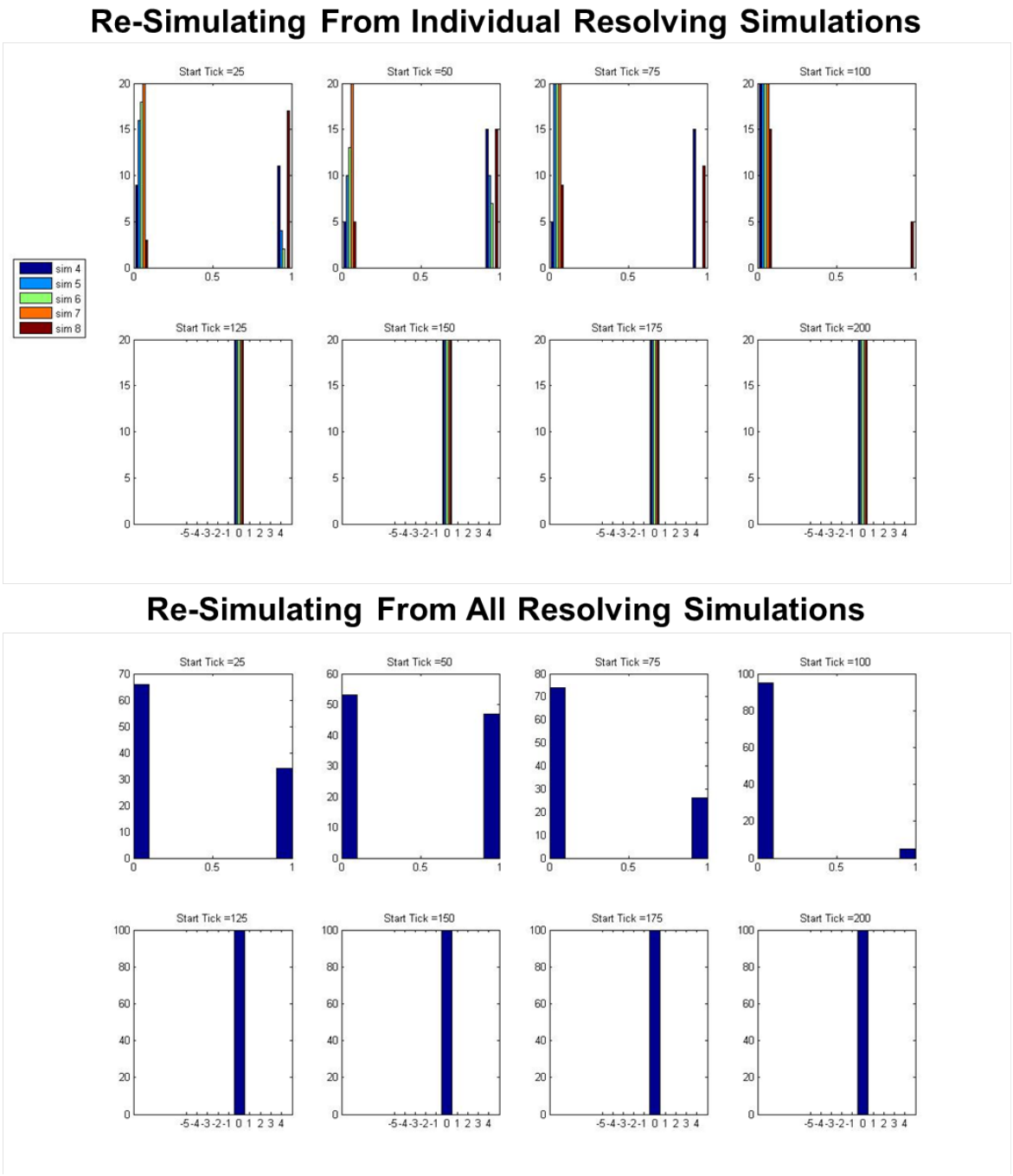

Figure 3.11. Histograms of Re-simulation Outcomes: Resolved.
Results of simulations starting from individual resolving simulations (upper panel) or all resolving simulaiton lumped together (lower panel). X-axis represents outcome: 0 = resolved, 1 = ulcerated.

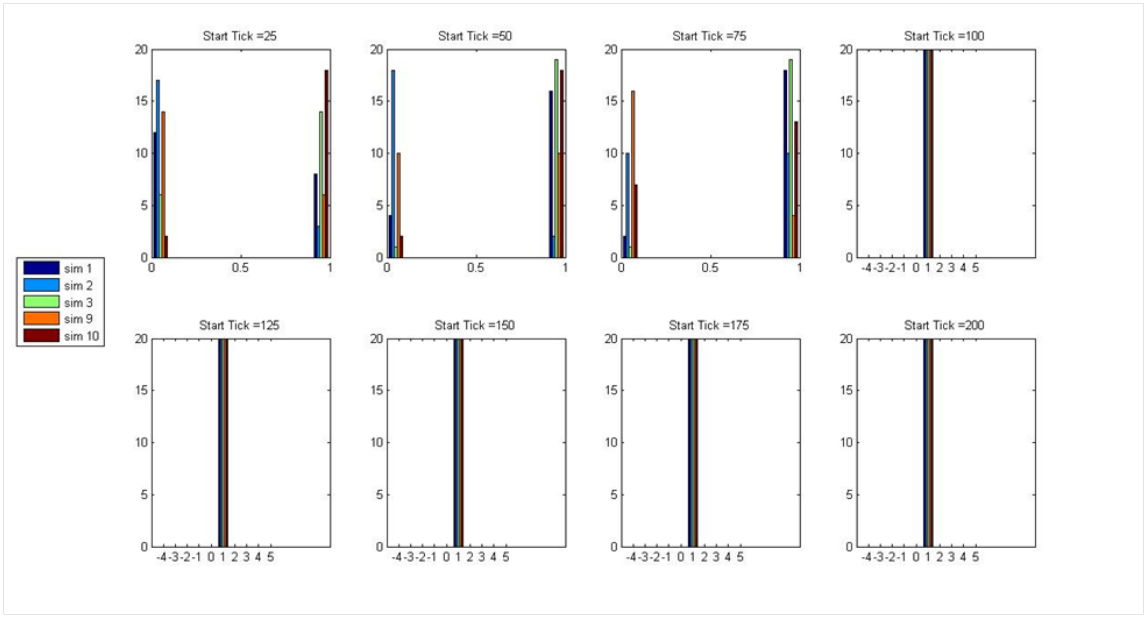

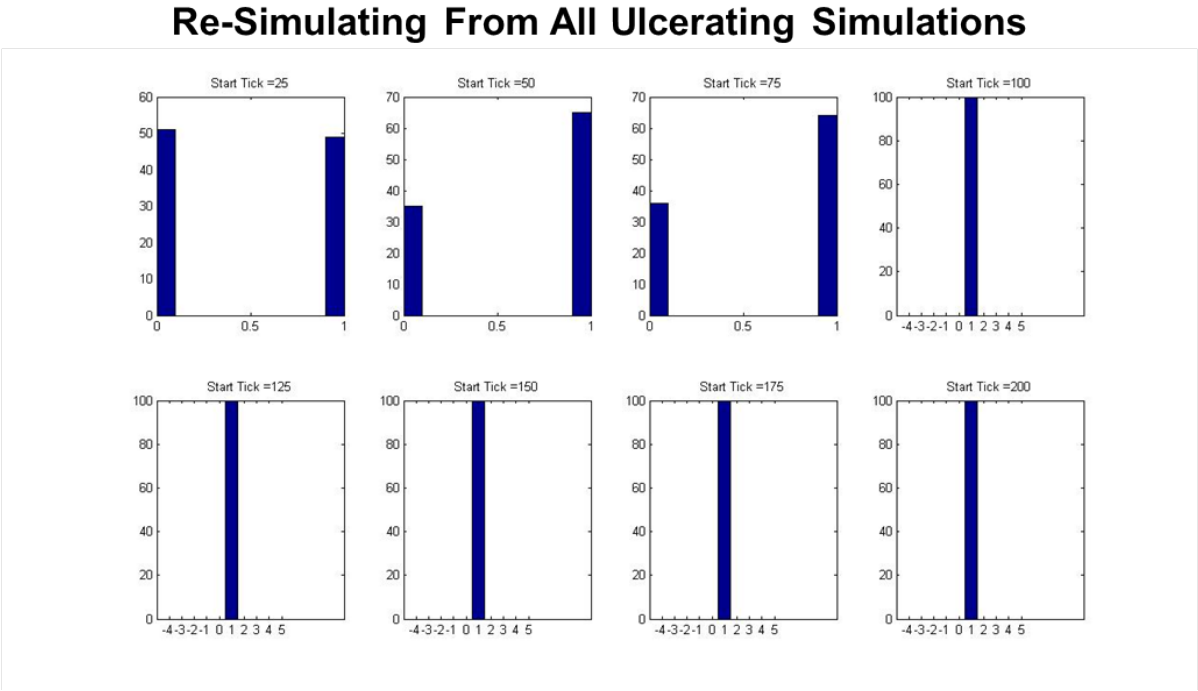

Figure 3.12. Histograms of Re-simulation Outcomes: Ulcerated.
Results of simulations starting from individual resolving simulations (upper panel) or all resolving simulaiton lumped together (lower panel). X-axis represents outcome: 0 = resolved, 1 = ulcerated.

3.3.4 Refining Source and Simulating Interventions

The above result, combined with the 1NN classification, suggests a course of action for preventing ulceration: prevent elaboration of TNF-α before and beyond t=100. It does not, however, point to the reason that some simulations achieve this outcome and others do not. In a future round of experiments, in order to infer what dynamics are critical to this tipping point, we would examine spatial time courses of mediators, cells, tissue health, and oxygen for ticks 50-150. This time, the outcome measure will be total TNF concentration. We could use information from the rules to inform the search. For example, distressed cells produce danger signals (which will activate neutrophils to produce TNF-a) except when there is a high enough local concentration of TGF-β1.

3.3.5 Global Sensitivity Analysis

The goal of a global sensitivity analysis is to understand how changing model parameter values affect the outcomes produced in simulations. An important part of this analysis is the question of how two or more parameters interact to produce compound results that would not be seen when changing one parameter at a time. This is the benefit to using a sampling scheme like orthogonal arrays: it allows you to maximize the number of interactions observed while minimizing the number of simulations necessary. However, this model has too many parameters to simulate a full analysis, even in an orthogonal array. Therefore, a model reduction would be necessary and unfortunately most methods of reduction rely on primary effects to choose important parameters. Therefore, before embarking on such a reduction, we sought to explore the amount of

interactions in the model by performing a sensitivity analysis aimed at observing the relative effects of each source of damage.

We previously identified three sources of damage: lack of oxygen, presence of TNF-α, and presence of ROS. These are the three broach mechanistic categories of damage, and for each there exists a single parameter that controls the magnitude of its effect in a simulation. These "big knobs" were used as the basis of a sensitivity analysis to explore how each mechanism contributed to damage and ulceration outcomes. The first level of analysis employed two levels: zero-effect and default (Fig 3.13). The zero-effect level of each parameter was defined as the value at which that source of damage no longer contributed to a simulation.

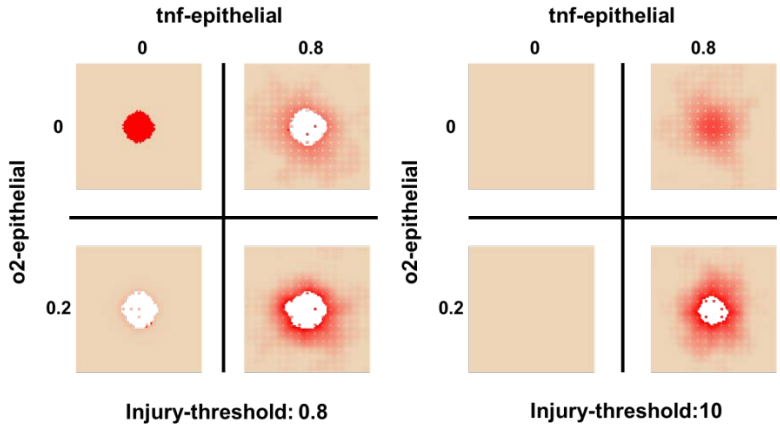

Figure 3.13. Qualitative SA: Big Knob Sources of Damage.
Here, we explore the relative effects of three sources of damage: ischemic injury, pro-inflammatory mediators, and free radicals. O2-epithelial controls the degree to which tissue cells respond to local oxygen concentration. Similarly, tnf-epithlial governs their response to tnf. Injury-threshold is the concentration of ROS required to damage a tissue cell, which occurs in a stepwise manner. The three parameters are set to either their default values or their zero-effect value (0 for o2-epithelia and tnf-epithelial, 10 for injury-threshold).

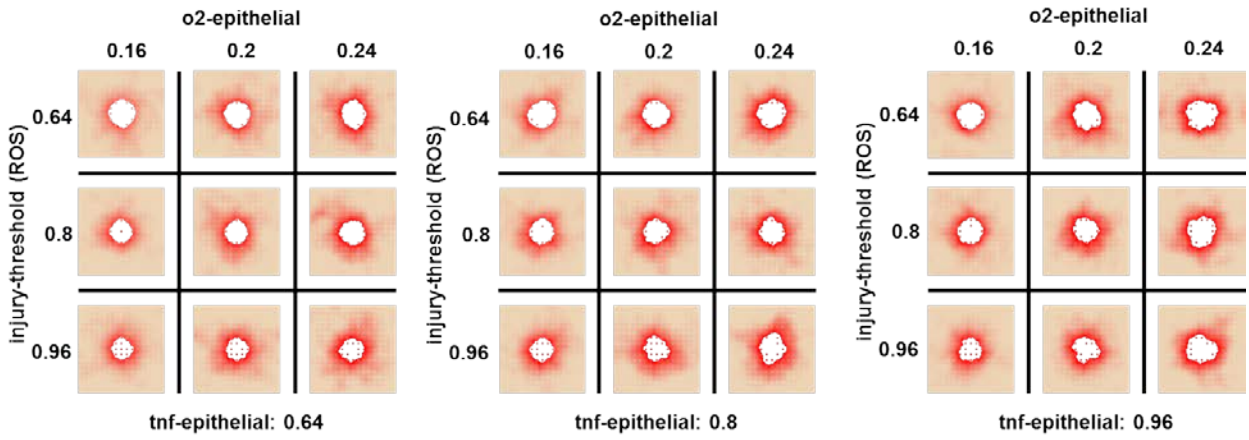

Figure 3.14. Qualitative SA: Smaller Parameter Ranges.
In this analysis, the same three parameters were varied in smaller ranges (default values ± 20%). The qualitative results are not very different, but it is evident that increasing sensitivity to oxygen leads toqualitatively more irregularly shaped ulcers.

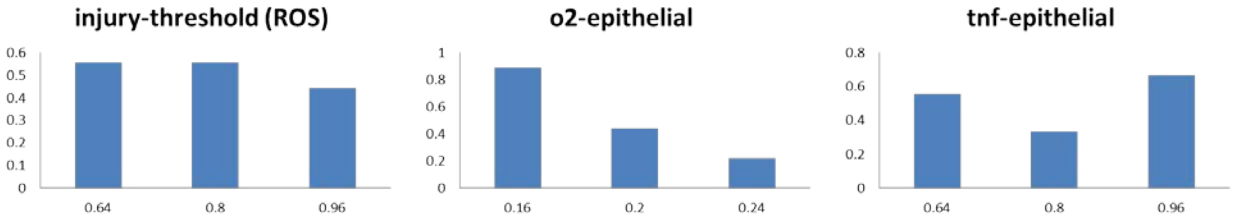

Figure 3.15. Examining Bimodality Among Big Knob Parameters.
X-axes are the values of each parameter and y axis is the number of simulations that incurred the smaller amount of damage (reached the second outcome) per ten simulations.

In earlier analyses, we examined instances of bimodality wherein simulations with the same parameters produced two levels of damage outcomes. With default parameters, we noted less damage in approximately 10% of simulations. Here, we examine the marginal effects of each big knob parameter on this bimodality. Interestingly, sensitivity to oxygen stands out as the best correlated parameter. With these results in mind, a reduced version of the model would make sure to include parameters that might have influences on both inflammation and oxygen.

3.4 DISCUSSION

ABMs are a class of models that are simple to construct and therefore accessible to people who would normally fall outside of the computational modeling community. This is an advantage of this class of model because it allows models to be built from a diverse set of perspectives. However, ABMs, like all computational models, require careful consideration of parameters when one is trying to model events that track in real time and space. Even with experience and awareness of these issues, it is easy for modelers to make mistakes. Sensitivity and uncertainty analysis can reveal any mistakes of this nature by showing aberrant behaviors that may not have been apparent at a local level. Adding quantitative analysis to what has mostly been a qualitative domain heretofore increases the utility of ABMs by increasing their reliability and their predictive power.

A major contribution of this work is the addition of statistical methods and machine learning approaches to aid in analyzing ABMs, which is an area that has received little attention. We employ these tools with the goal of inferring which mechanisms are most important when deciding clinical outcomes. We aimed to apply relatively basic techniques from statistics and machine learning to extract salient features from the model in an agnostic and meaningful way. We characterized dynamics in the model that appear to be input-independent yet very relevant to outcomes. Coupling this analysis with the parameter sensitivity analysis, both that of the previous chapter and the process outlined herein, we have developed a relatively thorough quantitative characterization of the model, which we could leverage to generate new clinically-relevant hypotheses. For example, the aleatory uncertainty analysis revealed early pro-inflammatory mediators and DAMPs as the factors critical determining resolving or ulcerative outcomes. However, a second iteration of this analysis should be performed to determine what

conditions are necessary to foster the appropriate environment for either stifling or inciting more pro-inflammatory activity. Once this is determined, a whole suite of *in silico*- and clinically-testable hypotheses will emerge. As another example, global sensitivity analysis suggested that decreased damage is associated with reduced sensitivity to oxygen, and reducing sensitivity to reactive oxygen species might slow or reduce ulceration. This leads to the hypotheses that treatment with antioxidants might be helpful in preventing ulceration, while oxygen should decrease cellular damage. While oxygen and antioxidants may not be new ideas for wound healing therapies, what is new is the information about how they contribute to pressure ulcer formation in different ways. Furthermore, as mentioned above, hyperbaric oxygen therapy has not shown promising results in pressure ulcer treatment, but these results indicate that wound oxygenation should still be explored as a therapeutic avenue. These hypotheses carry great potential for innovation because they are relatable to the overall system, testable in an *in silico* framework where variables such as population variability can be accounted for, and most importantly hold exciting potential for applications to patient-specific treatment strategies.

The quantitative analysis of the PUABM could, of course, extend further. A full characterization of global epistemic uncertainty could extend our insights from this model. However, it also may not. The PUABM is built at a resolution such that insights can only go so deep. To truly understand the dynamics between inflammatory mediators and the cells and binding partners in their environment, the time step of the model should be shorter than 1 hour of clock time. The biggest advantage of this model is its tissue-realistic output. Another approach to formal analysis of this model might be to treat the spatial output as high-dimensional images and use feature sets and learning techniques from image analysis to mine for useful diagnostic information.

4.0 CENTRAL ROLE FOR MCP-1/CCL-2 IN INJURY-INDUCED INFLAMMATION REVEALED BY *IN VITRO, IN SILICO,* AND CLINICAL STUDIES

This chapter comes from a manuscript that is currently under review at the journal *Critical Care Medicine*. (**Ziraldo, C.*;** Vodovotz, Y.*; Namas, R.A.; Mi, Q.; Barclay, D.; Almahmoud, K.; Jefferson, B.S.; Billiar, T.R.; Zamora, R. Central role for MCP-1/CCL2 in injury-induced inflammation revealed by *in vitro, in silico,* and clinical studies. Submitted) In this work, MCP-1 was identified as a primary driver of the inflammatory response in primary hepatocytes and then shown to correlate with outcomes in human trauma patients. MCP-1 levels predict levels of other important inflammatory cytokines, such as IL-6 and correlates with survival rates. My role in this work was to design, carry out, and interpret clustering analyses of time-dependent measurements of inflammatory mediators, seeking for patterns of dynamic behavior in hepatocyte lysates and supernatants.

4.1 ABSTRACT

The translation of *in vitro* findings to clinical outcomes is often elusive. Trauma/hemorrhagic shock (T/HS) results in hepatic hypoxia that drives inflammation. We hypothesized that *in silico* methods would help bridge *in vitro* hepatocyte data and clinical T/HS, in which the liver is a primary site of inflammation. Primary C57BL/6 mouse hepatocytes were

cultured under hypoxia (1% O_2) or normoxia (21% O_2) for 1-72 h, and both the cell supernatants and protein lysates were assayed for 18 inflammatory mediators. Statistical analyses, hierarchical and k-means clustering, Principal Component Analysis, and Dynamic Network Analysis suggested MCP-1/CCL2 and IL-1α as central coordinators of hepatocyte-mediated inflammation. Hepatocytes from MCP-1-null mice had altered dynamic inflammatory networks. Circulating MCP-1 levels segregated human T/HS survivors from non-survivors. Furthermore, T/HS survivors with elevated early levels of plasma MCP-1 post-injury had longer total lengths of stay, longer intensive care unit lengths of stay, and prolonged requirement for mechanical ventilation vs. those with low plasma MCP-1. This study identifies MCP-1 as a main driver of the response of hepatocytes *in vitro* and as a biomarker for clinical outcomes in T/HS, and suggests an experimental and computational framework for discovery of novel clinical biomarkers in inflammatory diseases.

4.2 INTRODUCTION

To inform mechanistic models, we seek a better understanding of the complex signals that drive the acute inflammatory response. The following study measured time-dependent levels of inflammatory mediators in cells that were stressed by hypoxia or normoxic cell culture over a period of 72 hours. From these data, we hoped to discern patterns of interacting cytokines that might be key regulators of the overall response.

Trauma/hemorrhagic shock (T/HS) results in hepatic hypoxia, resulting in a dynamic, complex inflammatory response both in the liver and systemically. To define this hepatic inflammatory response, primary C57BL/6 mouse hepatocytes were cultured under hypoxia (1%

O_2) or normoxia (21% O_2) for 1-72 h, and both the cell supernatants and protein lysates were assayed for 18 inflammatory mediators. Statistical analyses, hierarchical and k-means clustering, Principal Component Analysis (PCA), and Dynamic Network Analysis were utilized to define the most connected, and thereby possibly controlling, inflammatory mediators as a function of time and O_2 level. These analyses suggested MCP-1/CCL2 and IL-1α as central coordinators of hepatocyte-mediated inflammation. Hepatocytes from MCP-1-null mice exhibited an altered inflammatory response to cell stress. Circulating MCP-1/CCL2 levels naturally segregated T/HS patients, and patients with elevated early levels of MCP-1/CCL2 post-injury had longer total lengths of stay, longer intensive care unit lengths of stay, and prolonged requirement for mechanical ventilation. This study identifies MCP-1/CCL2 as a main driver of the response of hepatocytes *in vitro* and as a biomarker for organ damage in clinical settings of T/HS, and suggests an experimental and computational framework for discovery of novel clinical biomarkers in inflammatory diseases.

4.3 MATERIALS AND METHODS

4.3.1 Materials

Williams Medium E, penicillin, streptomycin, L-glutamine, and HEPES were purchased from Invitrogen (Carlsbad, CA). Insulin (Humulin®) was purchased from Eli Lilly (Indianapolis, IN), and calf serum was obtained from HyClone Laboratories (Logan, UT). Tissue culture dishes were from Corning Glass Works (Corning, NY). Unless indicated otherwise, all other chemicals and proteins were purchased from Sigma-Aldrich (St. Louis, MO).

4.3.2 Mouse Hepatocyte Isolation and Culture

All procedures involving animals were approved by the Animal Care and Use Committee of the University of Pittsburgh. Primary hepatocytes were harvested from wild-type C57BL/6 mice (Charles River Laboratories, Wilmington, MA) or MCP-1/CCL2-null (MCP-$1^{-/-}$) mice (The Jackson Laboratory, Bar Harbor, ME) (52) as previously described (62). Highly purified hepatocytes (>98% purity and >95% viability by trypan blue exclusion) were suspended in Williams' E medium supplemented with 10% heat-inactivated calf serum, 15 mM HEPES (pH 7.4), 16 units insulin, 2 mM L-glutamine, cell culture dishes ($3x10^6$ cells/6 cm dish or $5x10^6$ cells/10 cm dish) and cultured overnight at 37°C under normoxic conditions (5% CO_2). The old medium was then removed and cells were further incubated with fresh media containing 5% heat-inactivated calf serum. Hypoxic conditions were obtained by placing the cells into a modular incubator chamber (Billups-Rothenburg, Del Mar, CA) flushed with a hypoxic gas mixture containing 1% O_2, 5% CO_2 and 94% N_2. Hepatocytes incubated under normoxic conditions (21% O_2) served as controls.

4.3.3 Protein Isolation and Sample Preparation

At the end of each experiment, supernatants were collected and stored at -20°C until further analysis. The cell monolayers were then washed twice with ice-cold PBS and resuspended in ice-cold lysis buffer (Cell Lysis Buffer 10X from Cell Signaling Technology, Danvers, MA)

containing 2 mM Tris-HCl buffer (pH 7.5), 15 mM NaCl, 0.1 mM EDTA and EGTA, 0.1% Triton X-100, 250 μM sodium pyrophosphate, 100 μM β-glycerolphosphate, 100 μM Na_3VO_4, and the protease inhibitors leupeptin (0.1 μg/ml) and phenylmethylsulfonyl fluoride (PMSF, 1mM). After 5 min incubation on ice, the cells were scraped off the dish and transferred to microcentrifuge tubes. The cells were sonicated two times for 10-15 sec. with 1 min on ice between each sonication. Cell debris was then removed by centrifugation at 10,000 rpm for 10 min and the supernatant was used as cell lysate and stored at -20°C when necessary. An aliquot was used to determine protein concentration using the BCA Protein Assay Kit from Pierce (Rockford, IL) with bovine serum albumin as standard.

4.3.4 Western Blot Analysis

Protein samples (50 μg) were separated on 15% SDS-polyacrylamide gels and the gels were electroblotted onto PVDF nitrocellulose membranes. Immunodetection of MCP-1/CCL2 protein was done using a mouse specific rabbit polyclonal anti-MCP-1 antibody (Cell Signaling, Danvers, MA) at 1:1000 dilution, and the immunoreactive bands were visualized after incubation with the SuperSignal West Dura Extended Duration Substrate mouse kit (Thermo Scientific, Rockford, IL). Instructions for the kit were provided by the supplier. For normalization, the membranes were stripped and re-probed with an anti-β-actin antibody from Abcam (Cambridge, MA).

4.3.5 Measurement of Inflammatory Mediators

Mouse inflammatory mediators were detected in both cell lysates and supernatants using using the Milliplex™ Mouse Cytokine/Chemokine Panel I beadset (Millipore, Billerica, MA) and the Luminex™ 100 IS system (Luminex, Austin, TX) as per manufacturer's specifications. The antibody bead kit included: Granulocyte-Macrophage Colony-Stimulating Factor (**GM-CSF**), Interferon-γ (**IFN-γ**), Interleukin (**IL**)-**1α, IL-1β, IL-2, IL-4, IL-5, IL-6, IL-10, IL-13, IL-17,** Interferon-γ-inducible Protein 10 (**IP-10/CXCL10**), Keratinocyte-derived Cytokine (**KC/CXCL1**), Monocyte Chemoattractant Protein-1 (**MCP-1/CCL2**), Monokine induced by Interferon-γ (**MIG/CXCL9**), Macrophage Inflammatory Protein-1α (**MIP-1α/CCL3**), Tumor Necrosis Factor-α (**TNF-α**), and Vascular Endothelial Growth Factor (**VEGF**).

4.3.6 Cell Viability Assay

Cell viability was assessed by measuring the release of the cytoplasmic enzyme Lactate dehydrogenase (LDH) from damaged cells into the supernatant using a colorimetric assay Cytotoxicity Detection Kit (LDH assay; Roche Applied Science, Indianapolis, IN).

4.3.7 Statistical Analysis and Data-Driven Modeling

In an attempt to discern the main drivers of the cellular response and time-dependent changes in inflammatory mediators across experimental procedures, we carried out One-way and Two-way

ANOVA, hierarchical clustering over both raw data and fold changes, and k-means clustering after data was transformed into principal component space. In addition, Dynamic Network Analysis (DyNA) was utilized in order to define the principal (most connected and thereby possibly controlling) nodes as a function of both time and O_2 concentration. Before these analyses could be performed and in order to account for experimental variability in cell number, cell viability and protein concentration between individual experiments, the final mediator concentrations adjusted for protein content (C_F) were obtained from the Luminex analysis for each individual inflammatory mediator measurement (C) and its respective lysate protein concentration (as determined by BCA, see above) using the following formulas:

For cell supernantants: $$C_F = \frac{C\ (pg/ml)\ x\ V_{SN}\ (ml)}{BCA\ (\mu g\ protein/\mu l)\ x\ V_L\ (\mu l)}\ x\ 1000$$

For cell lysates: $$C_F = \frac{C\ (pg/ml)}{BCA\ (\mu g\ protein/ml)}\ x\ 1000$$

The final inflammatory mediator concentrations (C_F) are thus expressed in pg/mg total protein, where the supernatant volume (V_{SN}) and lysate buffer volume (V_L) values used were as follows:

Petri Dish	Medium Volume (V_{SN})	Lysis Buffer (V_L)
60 mm ($3x10^6$ cells)	3 ml	200 µl
100 mm ($5x10^6$ cells)	5 ml	400 µl

Experimental data are presented as mean ± SEM. Data analysis was performed by One-way or Two-way Analysis of Variance (ANOVA) followed by the Holm-Sidak *post-hoc* test, and

significance of differences in clinical outcomes was determined by Mann-Whitney *U* test using SigmaPlot (Systat Software, San Jose, CA) as indicated.

Before any dynamic analysis, the final inflammatory mediator concentrations (C_F) were first normalized for each inflammatory mediator, so that all inflammatory mediator levels were converted into the same scale (from 0 to 1). All measurements of a given inflammatory mediator from a single animal were normalized as a group, by dividing each value by the Euclidean norm of the group. In this way, any artifactual effects on variance due to the different ranges of concentration observed for different inflammatory mediators were eliminated.

4.3.8 Hierarchical Clustering

We employed hierarchical clustering to discern and compare dynamic patterns of inflammatory mediators in order to identify those inflammatory mediators that show similar behavior in production or secretion. This method creates groups (or clusters) of data points by comparing individuals according to a prescribed distance metric. The two most similar are clustered together and considered a single data point in further rounds. This process continues until all data have been joined into a single cluster. It is the order, or hierarchy, of additions to the cluster that determines the result. To capture dynamic patterns for each inflammatory mediator, we calculated the fold change values by dividing the difference between the later (x_2) and earlier (x_1) inflammatory mediator values by the earlier value: $(x_2-x_1)/x_1$, where $x_1 = 0$, we replaced 0 with a very small number (10^{-5}) to avoid division by zero. Mean fold changes across all animals gave a single fold change time course for each inflammatory mediator, which made up the columns of

the dendrogram. We employed several MatLab® functions to carry out this analysis: *linkage*, with average link and Pearson correlation distance was used to calculate the distances between all pairs of points, and *cluster* was used to build a hierarchical dendrogram resulting in 2-4 clusters to compare these dynamic patterns in both fold change and raw data (final inflammatory mediator concentrations adjusted for protein content vs. time, unaveraged, all animals included).

4.3.9 Principal Component Analysis and k-means Clustering

We employed Principal Component Analysis (PCA) to identify the subsets of mediators (in the form of orthogonal normalized linear combinations of the original mediator variables, called principal components) that are most strongly correlated with a given experimental procedure (e.g. normoxia or hypoxia), and that thereby might be considered principal drivers of each response. PCA is a statistical method that is widely used in data processing and dimension reduction. PCA achieves dimensionality reduction by finding new axes, called principal components that identify the linear combinations of signaling axes (in our study mediators). The principal components are defined by weighting signals with high covariance and de-emphasizing variance of signals that show little covariance with other signals. In this way PCA condenses measurements to highlight the global patterns in the data set as reflected by just two or three dimensions that capture the maximal covariance between all of the signals. In principal component space, the axes represent principal components, and each mediator is plotted as an ordered –tuple of its coefficients in each component. A mediator's covariance may align well with the first PC, lending it a high x value in PC space, but not contribute as much to the second PC, yielding a smaller y-value in PC space. Mediators with similar patterns of covariance should

project in similar directions in PC space. Normalized inflammatory mediator data (each measurement taken to be a single point in 18-dimensional inflammatory mediator space) were transformed into principal component space using the MatLab® function, *princomp*. We then examined projections of inflammatory mediators into principal component space by using the score coefficients for the first 2, 3, or 4 principal components. We employed k-means clustering using the MatLab® function, *kmeans*, using as a distance metric the cosine of the angle between a point and the origin. We computed clusters starting with k= 2, 3, or 4 random centroids. At each level of k, we repeated the clustering 10 times, resetting new centroids each time and taking the lowest mean distance between points and their nearest centroids as the best result.

4.3.10 Meta-Clustering

To compare the outcomes of the hierarchical and k-means clustering methods (see above), we calculated an Adjusted Rand Index (ARI) (44) to quantify to what degree any two clustering results were in agreement. This index has been used in gene expression analysis to assess the viability of various clustering schemes, including k-means clustering in PCA space, by comparing the clustering outcomes to a ground truth classification (97; 107; 108), but to our knowledge it has not been used with protein-level data previously. Since our goal was to compare the results of k-means clustering in PCA space vs. hierarchical clustering of fold changes vs. hierarchical clustering of raw data, we reasoned that we could use the ARI to assess the degree of similarity between each pair of clustering results. To do this, the first step was to select a single result from each method. For example, how many clusters should be considered, and, for PCA, how many principal components should be included? The ARI was first calculated

pairwise between clustering results including 2, 3, or 4 principal components. Our strategy was to choose the result that captured the most information with the fewest principal components. We then used ARI to compare hierarchical clustering results with k= 2, 3, and 4 to k-means clustering results with k= 2, 3 and 4 in a pairwise manner. The maximum Rand Index dictated the k of the hierarchical and k-means clustering results that were moved forward into further analysis. We compared PCA k-means clustering to each of fold change hierarchical clustering and raw data hierarchical clustering individually. The k was chosen for k-means clustering that maximized both ARI values.

To distill the most important information from three independent clustering results over 18 mediators for each of 4 experimental conditions, we filtered the results by discarding inflammatory mediators that showed inconsistent segregation patterns across the three analyses. The basis of comparison across different experiments was a consensus clustering containing only the mediators for whose coordination patterns we had confidence, as shown in detail in Fig. 4.4. The consensus clusters combine information from hierarchical clustering: which mediators have similar dynamic trajectories—and from PCA: which mediators have the strongest covariance with other mediators, and are therefore characteristic of the cells' response. Mediators that are consistently grouped together across all analyses should have strong, coordinated responses to cell stress. Briefly, a block of data was constructed with one mediator in each row and its corresponding cluster label for each of the three results in the columns using Microsoft Excel®. Sorting this block of data by each of the cluster label columns successively allowed us to compare the memberships of clusters across the three results and to identify corresponding clusters between results. These were clusters that contained a common set of mediators across all three results. We used the following heuristic to determine consensus: once a cluster from one

result was associated with clusters from the other results, (e.g. Cluster A from Raw Data was associated with Cluster 2 from Fold Change and Cluster IV from PCA clustering) it could not be associated with any other clusters. For example Cluster 1 could not associate with both Cluster A and Cluster B. Mediators that did not segregate into corresponding clusters across all results were deemed inconsistent and omitted from the consensus clustering result. This consensus outcome became the basis of comparison among experimental conditions (see Figure 4.4).

4.3.11 Dynamic Network Analysis (DyNA)

The goal of this analysis was to gain insights into dynamic changes in network connectivity of the cellular response to normoxia and hypoxia over time, and this analysis was carried out essentially as published previously (63). To do so, inflammatory mediator networks were created over time periods between consecutive measurements (1-3 h, 3-6 h, 6-24 h, 24-48 h, and 48-72 h) using Matlab® and Inkscape® software (http://inkscape.org/). In order to be included in the DyNA, a given mediator had to be statistically significantly different from its baseline value (no treatment [time = 1 h]; $P< 0.05$ by Student's t-test). Connections in the network were created if the correlation coefficient between two nodes (inflammatory mediators) was greater or equal to a threshold of 0.7 (based on a total of 12 samples with 10 degrees of freedom, $P<0.05$).

4.3.12 Human Trauma Patient Selection and Analysis

All human sampling was done following approval by the University of Pittsburgh Institutional Review Board and informed consent was obtained from each patient or next of kin as per

Institutional Review Board regulations. From a cohort of 493 blunt trauma patients admitted to Presbyterian University Hospital (part of the University of Pittsburgh Medical Center), we selected 62 patients (all survivors) separated into two groups matched on age, gender, and Injury Severity Score (ISS): 31 normotensive patients (19 males and 12 females; systolic blood pressure >90 mmHg, mean age: 44.4 ± 2.2 years, range: 24-75 years, mean ISS: 23.5 ± 1.3, range: 10-38), matched with 31 hypotensive patients (19 males and 12 females; systolic blood pressure <90 mmHg, duration of hypotension post-injury: 8 ± 1 h, range: 2-21 h, mean age: 45.1 ± 3.4 years, range: 20-89 years, mean ISS: 23.5 ± 2.2, range: 4-54). One to four blood plasma samples per patient were collected within the first 24 h post-injury, followed by additional sampling at 48, 72, and 96 h. All blood samples were stored at -80°C until analysis. MCP-1/CCL2 and IL-6 were measured using the Luminex™ 100 IS system and the Human 25-plex® Luminex™ beadset (BioSource, now Invitrogen) or the Milliplex^{TM} MAP kit (Millipore, Billerica, MA).

4.4 RESULTS

4.4.1 MCP-1/CCL2 is a central component of the dynamic, multi-dimensional response of hepatocytes to cell stress

To assess the response of hepatocytes to hypoxia, we subjected primary wild-type mouse hepatocytes to 1% O_2 for various periods of time (1, 3, 6, 24, 48, and 72 h), followed by Luminex™ analysis of 18 mouse cytokines and chemokines in both the supernatant and whole-cell lysate. Control hepatocytes were cultured under normoxic (21% O_2) conditions. To determine which mediators changed significantly across time, and under which experimental conditions, one-way ANOVA was performed over of the time courses for each inflammatory mediator in both lysates and supernatants (Table 4.1). The results showed significant differences in various inflammatory mediators, depending on experimental treatment, time point, and cellular localization: while in the normoxia control group only three mediators showed significant changes (MCP-1/CCL2, KC/CXCL1, and IP-10/CXCL10 in lysates, and MCP-1/CCL2, KC/CXCL1, and MIG/CXCL9 in supernatants), in the hypoxia group the number of mediators showing statistically significant changes increased (MCP-1/CCL2, MIG/CXCL9, IL-1α, IL-1β, IL-10, and IL-13 in lysates; MCP-1/CCL2, IP-10/CXCL10, IL-1α, and VEGF in supernatants). Notably, MCP-1/CCL2 was the only mediator that exhibited significant changes in all four conditions examined (Table 4.1). The experimental values for this mediator are shown in Fig. 4.1. These results suggested that MCP-1/CCL2 is a central player in the differential production of key cytokines and chemokines by hepatocytes in response to cellular stress.

Table 4.1: One-way ANOVA p-values (wild-type)
Significance levels ($P<0.05$) for production and release of inflammatory mediators from wild-type mouse hepatocytes cultured under normoxic or hypoxic conditions (1-72 h) as determined by one-way ANOVA. *For hypoxia time courses, the analysis was performed using as baseline the respective concentration values for normoxia at 1 h.

	Normoxia		**Hypoxia***	
	Lysate	**Supernatant**	**Lysate**	**Supernatant**
GM-CSF	0.721	1	0.753	0.086
IFN-γ	0.105	1	0.452	1
IL-1α	0.591	1	**0.023**	**0.007**
IL-1β	0.559	0.664	**0.026**	0.886
IL-2	0.126	0.929	0.24	0.919
IL-4	0.901	0.942	0.935	0.656
IL-5	1	1	0.123	0.101
IL-6	0.091	0.914	0.223	0.059
IL-10	0.346	0.947	**0.035**	0.832
IL-13	0.601	1	**0.002**	0.65
IL-17	0.98	0.921	0.958	0.999
IP-10	**0.045**	0.513	0.135	**0.046**
KC	**0.002**	**<0.001**	0.374	0.283
MCP-1	**0.001**	**<0.001**	**0.003**	**<0.001**
MIG	0.15	**0.002**	**0.016**	0.177
MIP-1α	0.636	0.416	0.081	0.543
TNF-α	0.987	0.685	0.056	0.999
VEGF	0.271	**<0.001**	0.073	**<0.001**

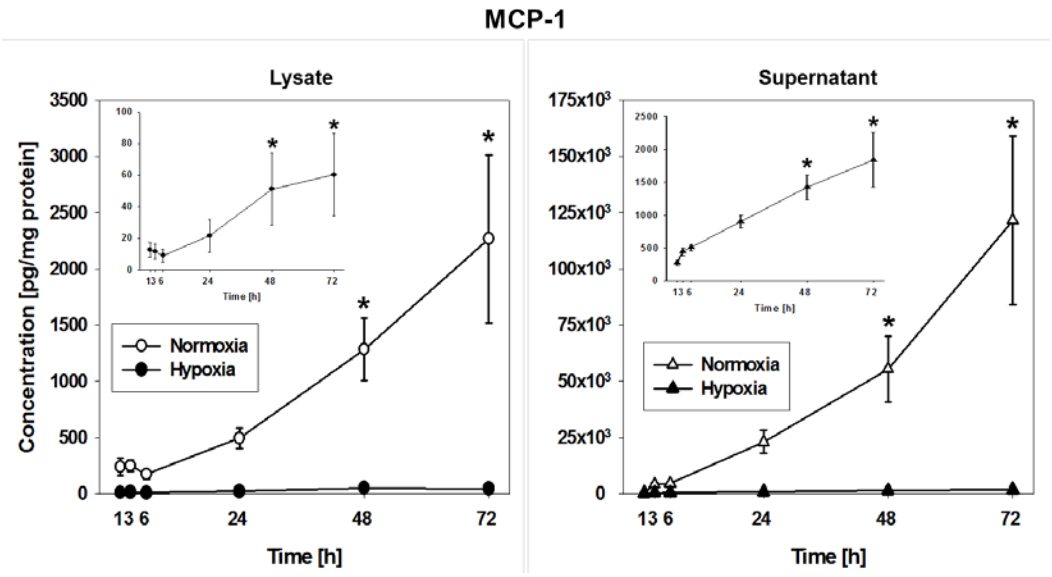

Figure 4.1 Inflammatory mediator production by normoxic and hypoxic primary mouse hepatocytes.
Freshly isolated hepatocytes from C57BL/6 (wild-type) mice were cultured under normoxic (control, 21% O_2, open symbols) or hypoxic (1% O_2, closed symbols) conditions for 1, 3, 6, 24, 48 and 72 h as described in Mater*ials and Methods.* At the end of the experiments, samples from both lysates and supernatants were assayed for 18 mouse inflammatory mediators using the Luminex xMAP technology and the measurements were normalized for protein content as indicated. (A) MCP-1/CCL2 expression and release in primary mouse hepatocytes. Results are the mean ± SEM (n=4-8 independent experiments) and were analyzed by Two-Way ANOVA followed by the Holm-Sidak *post-hoc* test (**P*<0.001, normoxia vs. hypoxia within a specific time point). The insets show the levels of MCP-1/CCL2 in hypoxia samples.

4.4.2 Hierarchical Clustering and Principal Component Analysis reveal key differences in inflammatory mediator production/release in the hepatocyte response to cell stress

From the analysis above, we showed that, in addition to MCP-1/CCL2, other inflammatory mediators also change significantly over the time course of our studies. In order to address the question of which groups of mediators have similar dynamic trajectories, we performed hierarchical clustering on fold changes for each mediator at each pair of consecutive time points. We calculated the fold change values for all mediators over each time interval, in order to assess

how quickly the concentration of a given inflammatory mediator changed relative to its earlier value. Taken together, each inflammatory mediator's set of fold change values over time made up its dynamic pattern of expression and release. To identify those inflammatory mediators that showed similar production or secretion behavior, these patterns were then compared and grouped using hierarchical clustering, with inflammatory mediators in the resulting dendrogram ordered according to their membership in the clusters that emerged (Fig. 4.2; see *Materials and Methods* for methodological details). The fold change values for each inflammatory mediator are represented in heat maps, ranging from large negative (green) to large positive values (red). No changes (zero values) are represented in black (Fig. 4.2). We repeated the same clustering process with raw inflammatory mediator measurements as well, which was also used for meta-clustering analysis (see below). Analysis of the heat maps showed different grouping patterns in the experimental groups (normoxia vs. hypoxia) both in lysates and supernatants (Fig. 4.2).

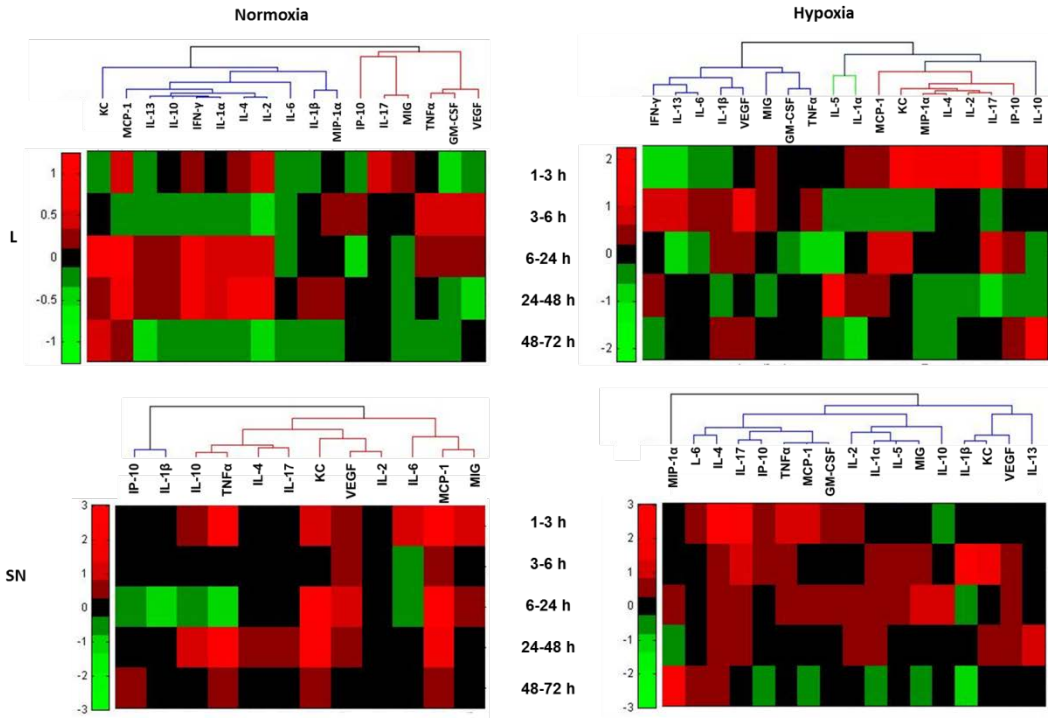

Figure 4.2: Hierarchical clustering over fold changes in wild-type hepatocytes (normoxia vs. hypoxia).
Fold change values for each inflammatory mediator are represented in heat maps, ranging from large negative (green) to large positive values (red). Zero fold changes are represented in black (see *Materials and Methods* and *Results* for full description and analysis).

We also sought to determine the subset of mediators that evolve dynamically in a manner that is most characteristic of the response to normoxia or hypoxia, respectively. Inflammatory mediators that have similar patterns of covariance have similar loadings onto principal components, and so would be expected to project in a similar direction in principal component space. We therefore used the angle of an inflammatory mediator's projection into PCA space as the basis of a distance metric in k-means clustering, as described in *Materials and Methods*. The resulting clusters contain mediators that have similar patterns of covariance with the remaining mediators. The inflammatory mediator groupings according to k-means clustering are shown in Fig. 4.3 for lysates (*Panel A* for normoxia and *Panel B* for hypoxia) and supernatants (*Panel C* for normoxia and *Panel D* for hypoxia). Despite an overlap in common mediators, k-means

clustering served to differentiate normoxia from hypoxia and lysates from supernatants in primary hepatocytes, where more than 60% of the total variance could be explained by the combination of only three principal components in all experimental conditions (Fig. 4.3A-D). We found that MCP-1/CCL2 and KC/CXCL1 were generally grouped together and were the predominant mediators along the first principal component (Fig. 4.3A-D). In normoxia lysates, MCP-1/CCL2 and KC/CXCL1 have the strongest covariance with each other and other mediators suggesting that these mediators may have the strongest signal in response to stress (Fig. 4.3A). Furthermore, in hypoxia lysates MCP-1/CCL2, KC/CXCL1, and MIG/CXCL9 are strongly correlated to each other as well as the overall covariance of all inflammatory mediators measured in hypoxia lysates, but the strongest response signal was carried by IL-2 and IL-4 (Fig. 4.3B). In normoxia supernatants, two sets of inflammatory mediators see to explain most of the covariance, but are anti-correlated with each other: KC/CXCL1, MCP-1/CCL2, VEGF, and MIG/CXCL9 all oppose signals from IL-1β, IL-10 and IP-10 (Fig. 4.3C). In hypoxia supernatants, the covariance of the response was dominated by IL-5, IL-6, and MIP-1α/CCL3 (Fig. 4.3D)**.** Overall, in lysates the strongest stress response seems to be from MCP-1/CCL2 and KC/CXCL1 together. In supernatants, these chemokines contribute, but to the secondary and tertiary, not primary responses.

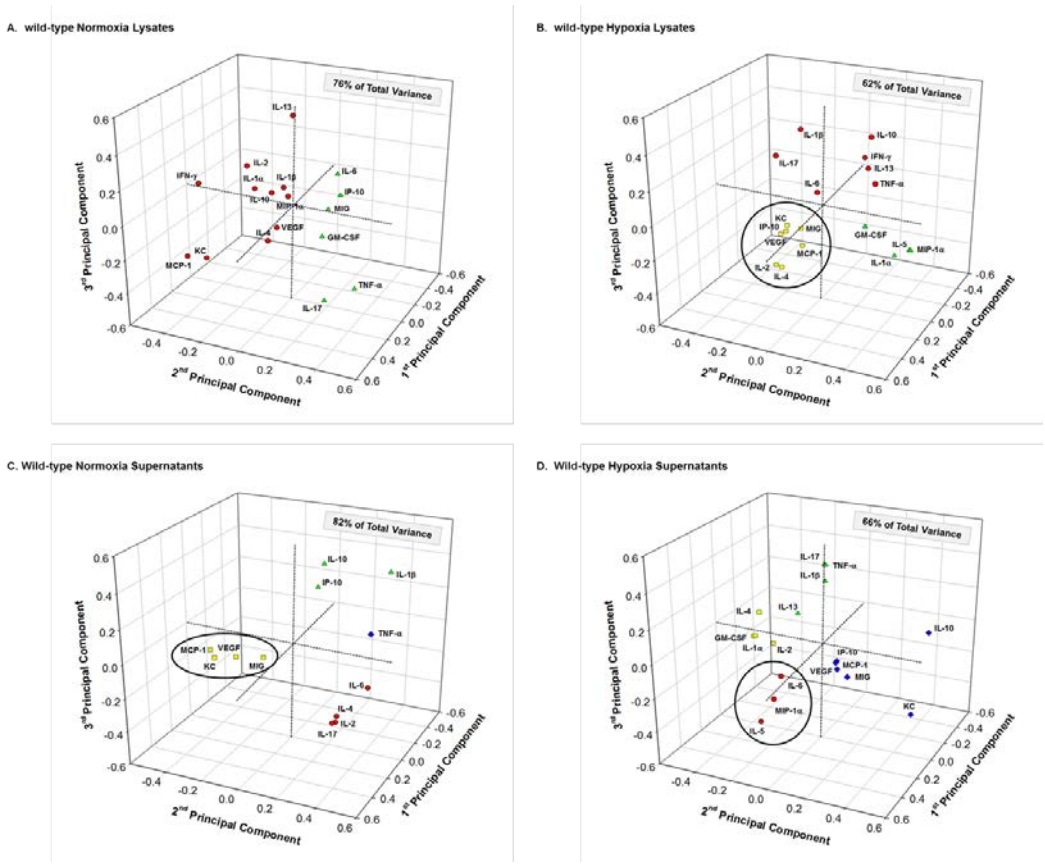

Figure 4.3: PCA and k-means Clustering.
Relevant inflammatory mediator groupings in the hepatocyte response to normoxia or hypoxia as determined by consensus of clustering methods. Freshly isolated hepatocytes from wild-type mice were cultured under normoxic (control, 21% O_2) or hypoxic (1% O_2) conditions for 1, 3, 6, 24, 48 and 72 h as described in *Materials and Methods*. At the end of the experiments, samples from both lysates (L) and supernatants (SN) were assayed for 18 mouse inflammatory mediators using the Luminex xMAP technology, the measurements were normalized for protein content and over each inflammatory mediator and each sample and k-means clustering was performed over dynamic inflammatory mediator measurements from 4 experimental conditions (N vs. H, and L vs. SN) using MatLab® software as described in the *Materials and Methods*. The tridimensional grouping of significant inflammatory mediators according to k-means clustering is represented as follows: (A) normoxia lysate, (B) hypoxia lysate, (C) normoxia supernatant, and (D) hypoxia supernatant. (The percentage of total variance corresponding to each analysis is shown on the top of the graphs).

We next sought to compare the results of the three aforementioned, independent clustering experiments. If the cluster memberships were similar, then those mediators that did not segregate consistently across different clusterings of a process could be treated as noise. In contrast, those inflammatory mediators that consistently segregated together were considered to

be the mediators that truly exhibited similar or correlated dynamic trajectories, and thus could be important drivers or indicators of the response of hepatocytes to either normoxia or hypoxia. To compare the outcomes of the hierarchical and k-means clustering methods, we performed a meta-clustering analysis (Fig. 4.4, see *Materials and Methods*), which resulted in a "consensus clustering" showing the inflammatory mediators that exhibited the same segregation pattern across all analysis methods. We found that MCP-1/CCL2 and KC/CXCL1 segregated together across all experimental conditions in every clustering experiment (Fig. 4.5).

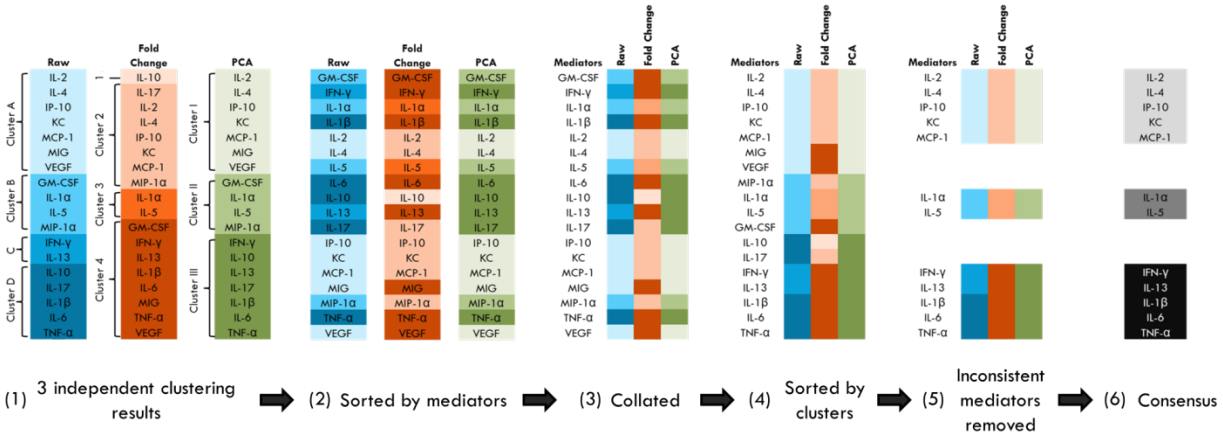

Figure 4.4: Meta-clustering process: from three independent clustering results to a consensus clustering. Example: wild-type Hypoxia Lysates.
Each method is colored one hue (blue = hierarchical clustering of raw data, orange = hierarchical clustering on fold changes, green = k-means clustering in PCA space) and clusters within each method are demarcated by shades and tones of each hue. Each column was then sorted alphabetically by mediator names and the clustering results were combined into a single matrix. The rows of this matrix were sorted by cluster labels, sequentially. This sorting allowed visual identification of clusters that were associated across methods. In this case the rows were first sorted according to PCA clusters, then by fold change cluster labels, and finally by raw data cluster labels. From here, a consensus can be determined by following a heuristic: identify associated clusters, identify and remove inconsistent mediators. For example, it is plain to see that a majority of mediators from Cluster A are also found in Cluster 2 and Cluster I. Therefore, these three clusters are considered to be the same. Any mediators associated with Cluster A, but not with both Cluster 2 and Cluster I were then marked as inconsistent and discarded from the analysis. One special case is when two clusters from one method fuse together to associate with clusters from other methods. In this case, Clusters C and D both associate with Cluster 4 and Cluster III. As long as neither C nor D associate with any other clusters, this is permitted.

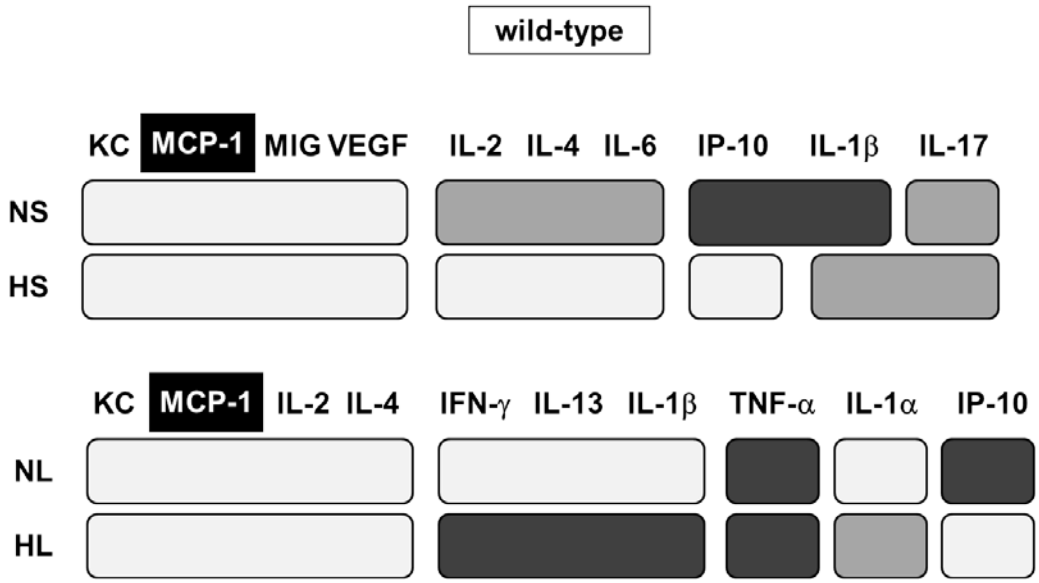

Figure 4.5: Comparison of the outcomes of the hierarchical and k-means clustering methods using meta-clustering.
The shading of the boxes indicates the grouping of inflammatory mediators that exhibited the same segregation pattern across all methods. For each experimental condition, only the mediators appearing in the consensus are shown in this figure. Furthermore, to compare two experimental conditions, we show only the mediators present in both consensuses (with ten mediators remaining in each comparison, very few mediators had to be omitted in the comparison step).

4.4.3 A predominant role for MCP-1/CCL2, KC/CXCL1, and IL-1α in the hepatocyte response to stress inferred from Dynamic Network Analysis

The preceding meta-clustering analysis allowed us to define groups of inflammatory mediators that had similar patterns as they changed in time (see above). We then used the Luminex™ time courses of mediators to determine how these associations changed across time. In order to identify the dynamic connections among inflammatory mediators, to determine which mediators appear to be "hubs" (or most connected to other mediators), and to delineate the changes in this architecture over time, we performed Dynamic Network Analysis (DyNA) as published previously (63) and described in the *Materials and Methods*. These analyses were performed for

each of the following time intervals: 1-3 h, 3-6 h, 6-24 h, 24-48 h, and 48-72 h. Summaries of DyNAs showing principal inflammatory mediator "hubs" of the response to normoxia and hypoxia are shown in Figs. 4.6 and 4.7, respectively. The total number of connections resulting from these analyses is shown in Fig. 4.8. Based on DyNA, MCP-1/CCL2 and KC/CXCL1 were the most connected mediators across all time points in normoxia supernatants, and at 24-72 h in normoxia lysates (Fig. 4.6). In hypoxia, the most connected inflammatory mediators were IL-1α and VEGF in supernatants and IL-1α and MIP-1α/CCL3 in lysates (Fig. 4.7). Overall, the most connected inflammatory mediators were MCP-1/CCL2 and IL-1α, with MCP-1/CCL2 being the only highly-connected node present in all experimental conditions examined (Fig. 4.8).

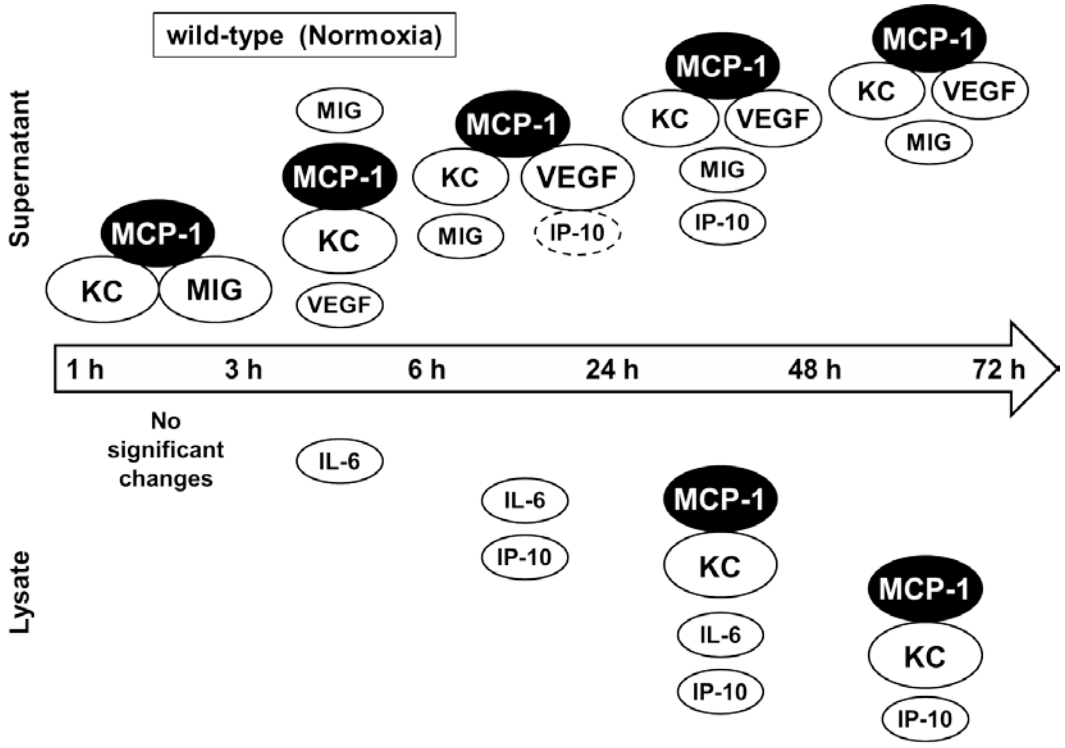

Figure 4.6. Dynamic Network Analysis (DyNA) of inflammatory mediators produced by normoxic mouse hepatocytes.
Primary hepatocytes from wild-type mice were cultured under normoxic conditions (1-72 h) followed by measurement of inflammatory mediators in both lysates and supernatants and lysates as described in Materials and Methods. After data normalization, Dynamic Network Analysis

during each of the following five time frames: 1-3 h, 3-6 h, 6-24 h, 24-48 h, and 48-72 h was performed for both normoxia lysates and normoxia supernatants as indicated. The most connected mediators—those that were correlated with the greatest number of other mediators in a time step—are shown here. Each mediator's node size is proportional to the number of connections it has in a given time interval. When correlated to other represented mediators, they are illutrated as touching. Other highly connected mediators that are not connected to mediators illustrated here are show not touching. MCP-1 is hgihlighted in black. A dotted circle indicates a high negative correlation between two touching mediators.

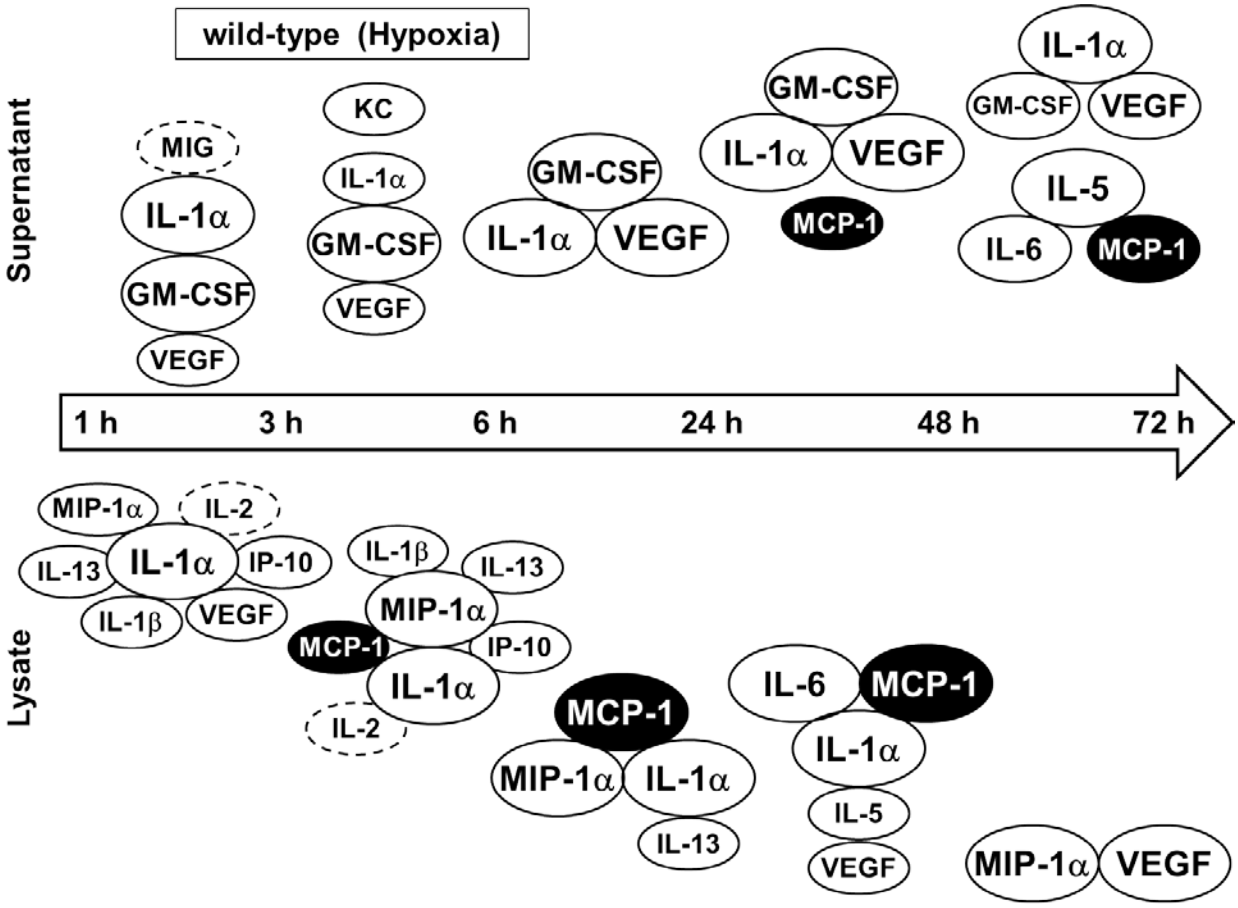

Figure 4.7. Dynamic Network Analysis (DyNA) of inflammatory mediators produced by hypoxic mouse hepatocytes.

Primary hepatocytes from wild-type mice were cultured under hypoxic conditions (1-72 h) followed by measurement of inflammatory mediators in both lysates and supernatants and lysates as described in Materials and Methods. After data normalization, Dynamic Network Analysis during each of the following five time frames: 1-3 h, 3-6 h, 6-24 h, 24-48 h, and 48-72 h was performed for both hypoxia lysates and hypoxia supernatants as indicated. The most connected mediators—those that were correlated with the greatest number of other mediators in a time step—are shown here. Each mediator's node size is proportional to the number of connections it has in a given time interval. When correlated to other represented mediators, they are illutrated as touching. Other highly connected mediators that are not connected to mediators illustrated here are show not touching. MCP-1 is hgihlighted in black. A dotted circle indicates a high negative correlation between two touching mediators.

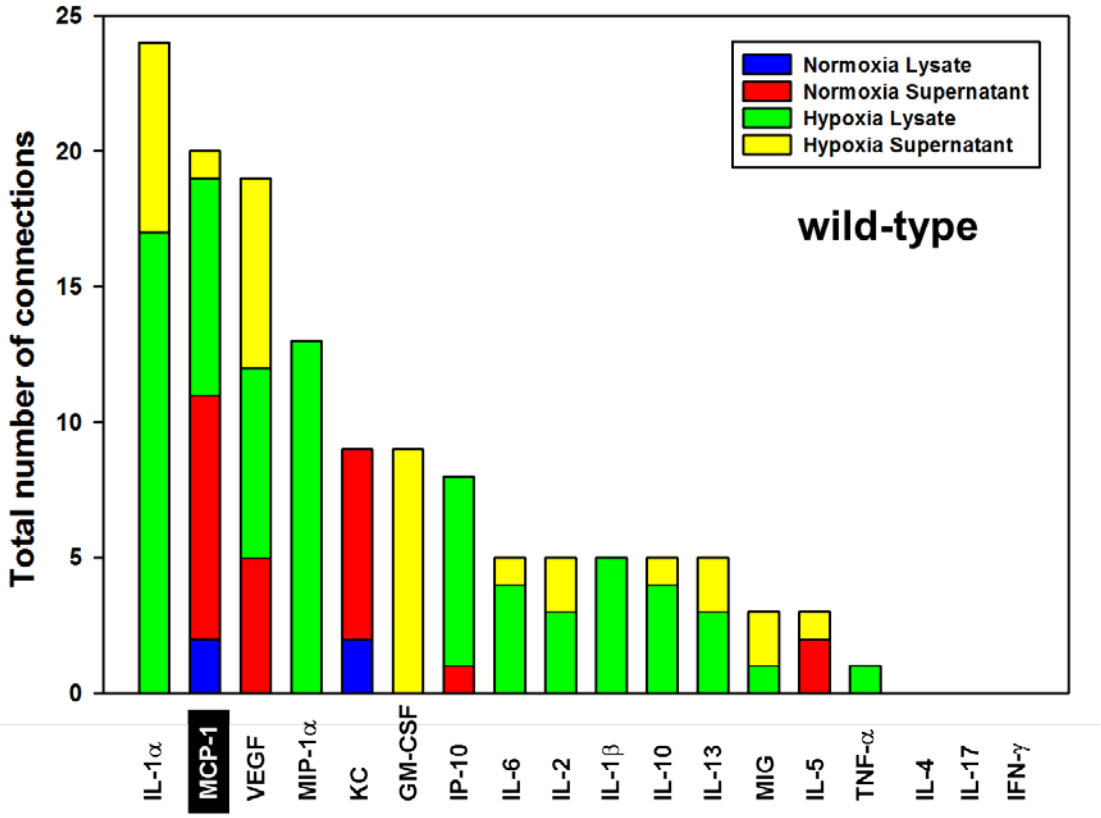

Figure 4.8: Total Connections in DyNA analyses across experimental conditions.
The stacked bars represent the total number of connections for each inflammatory mediator over all time intervals. Each color stands for one experimental condition. IL-1a, MCP-1 and VEGF had the highest number of connections overall. Notably, MCP-1 was the only mediator that was connected in all four experimental conditions.

4.4.4 Inflammatory dynamics and networks are disrupted in hepatocytes from MCP-1$^{-/-}$ mice

Our *in vitro* studies and computational analyses led us to hypothesize a central role for MCP-1/CCL2 in the response of mouse hepatocytes to cell stress. To test this hypothesis, we performed analogous experiments using primary hepatocytes from MCP-1$^{-/-}$ mice. As in our studies in wild-type mouse hepatocytes, freshly isolated hepatocytes from MCP-1$^{-/-}$ mice were

subjected to hypoxia (1% O_2) for various periods of time (1-72 h), followed by Luminex™ analysis of 18 mouse cytokines/chemokines in both the lysates and the supernatants and using normoxic cells as control.

We first sought to verify that MCP-1/CCL-2 was absent in MCP-$1^{-/-}$ mice. As shown in Fig. 4.9, normoxic hepatocytes from MCP-$1^{-/-}$ mice did not express MCP-1/CCL2 protein by Western blot, while a weaker band of approximately 30 kDa was detected in the lysates from hypoxic cells. In contrast, MCP-1/CCL2 protein expression was significantly higher in cell lysates of both normoxic and hypoxic hepatocytes from wild-type mice at 48 and 72 h (Fig. 4.9). This analysis suggested the low, but detectable, presence of a protein with MCP-1/CCL2-like characteristics in the nominally MCP-$1^{-/-}$ mice.

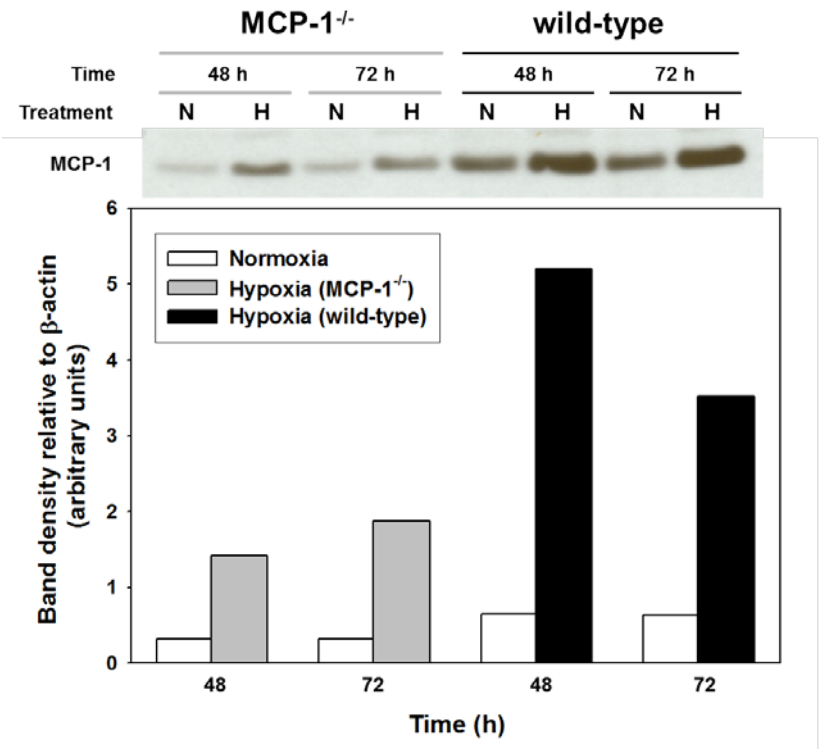

Figure 4.9. MCP-1/CCL2 is a central component of the dynamic, multi-dimensional response of hepatocytes to cell stress.
Primary hepatocytes from wild-type and MCP-$1^{-/-}$ mice were cultured under normoxic (N) or hypoxic (H) conditions for 1-72 h, followed by Luminex™ analysis of 18 inflammatory mediators in both the supernatant (SN) and whole-cell lysate (L). The measurements were normalized and hierarchical and k-means clustering was performed as described in *Materials and Methods*. A representative Western blot showing MCP-1/CCL2 protein expression in cell lysates from normoxic (N) and hypoxic (H) MCP-$1^{-/-}$ and wild-type mouse hepatocytes (48 and 72 h) and densitometric analysis as described in *Materials and Methods.*

Following normalization of the Luminex™ data for protein content, we performed one-way ANOVA for each inflammatory mediator in both lysates and supernatants of MCP-$1^{-/-}$ hepatocytes (Table 4.2). Based on this analysis, we observed differences in the mediators that changed over time depending on both the experimental treatment and the cellular localization as compared to wild-type hepatocytes (see Table 4.1). As in the wild-type cells, only three mediators in the normoxia group showed significant changes (MIG/CXCL9, KC/CXCL1, and IL-6 in lysates; KC/CXCL1, IL-1β, and VEGF in supernatants), while more inflammatory

mediators showed statistically significant changes in the hypoxia group (MIP-1α/CCL3, IL-1α, IL-1β, IL-2, IL-6, IL-10, IL-13, IFN-γ, and TNF-α in lysates; KC/CXCL1, IL-1α, and VEGF in supernatants).

Table 4.2: One-way ANOVA p-values (MCP-1$^{-/-}$)
Significance levels (P<0.05) for production and release of inflammatory mediators from MCP-1$^{-/-}$ mouse hepatocytes cultured under normoxic or hypoxic conditions (1-72 h) as determined by one-way ANOVA. *For hypoxia time courses, the analysis was performed using as baseline the respective concentration values for normoxia at 1 h.

	Normoxia		**Hypoxia***	
	Lysate	**Supernatant**	**Lysate**	**Supernatant**
GM-CSF	0.918	0.535	0.239	0.423
IFN-γ	0.897	0.371	**<0.001**	0.53
IL-1α	0.869	0.249	**0.002**	**0.034**
IL-1β	0.748	**0.031**	**0.008**	0.369
IL-2	0.978	0.332	**0.006**	0.282
IL-4	0.982	0.669	0.978	0.054
IL-5	0.757	1	0.379	1
IL-6	**<0.001**	0.475	**<0.001**	0.403
IL-10	0.439	0.696	**<0.001**	0.57
IL-13	0.191	0.888	**<0.001**	0.978
IL-17	0.992	0.995	0.96	0.945
IP-10	0.783	0.572	0.925	0.518
KC	**<0.001**	**<0.001**	0.234	**0.009**
MCP-1	0.823	0.535	0.573	0.782
MIG	**0.003**	0.761	0.609	0.068
MIP-1α	0.363	0.078	**0.009**	0.653
TNF-α	0.833	1	**0.002**	1
VEGF	0.599	**<0.001**	0.242	**0.019**

As we did for the wild-type hepatocytes, we next used Luminex™ mediator measurements from MCP-1$^{-/-}$ cells as the basis for meta-clustering (of hierarchical clustering over raw data, hierarchical clustering over fold changes, and k-means clustering in PCA space)

and Dynamic Network Analysis. As before, the fold change values for each inflammatory mediator are represented in heat maps, ranging from large negative (green) to large positive values (red). The absence of changes from baseline is represented in black (Fig. 4.10). As was the case for the wild-type hepatocytes, hierarchical clustering over fold changes resulted in different grouping patterns between the two experimental groups (normoxia vs. hypoxia) both in lysates and supernatants and also when comparing the MCP-1$^{-/-}$ (Fig. 4.10) vs. wild-type mouse hepatocytes (see Fig. 4.2 for comparison).

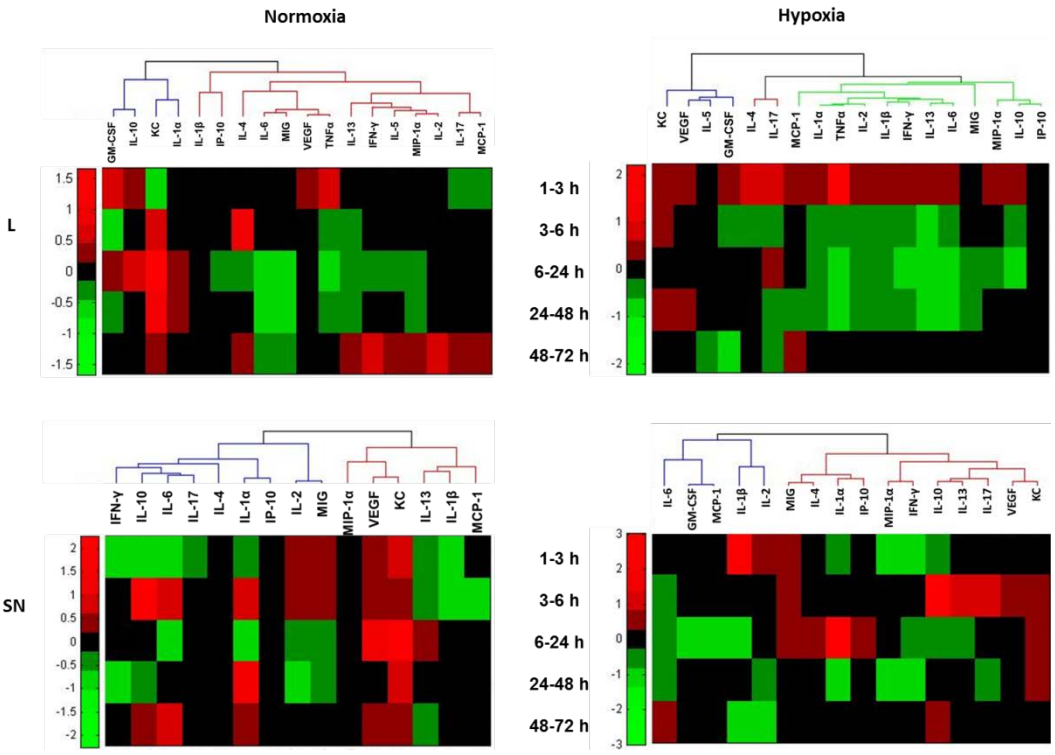

Figure 4.10. Hierarchical clustering over fold changes in MCP-1$^{-/-}$ hepatocytes (normoxia vs. hypoxia).
Fold change values for each inflammatory mediator ranging from large negative (green) to large positive values (red) are shown. No fold changes (zero values) are represented in black.

We next carried out k-means clustering over inflammatory mediator measurements transformed into PCA space. In normoxia lysates as well as hypoxia lysates (Fig. 4.11) and supernatants, MCP-1$^{-/-}$ hepatocytes) most of the variance could be explained by a linear

combination of only two principal components (in contrast to wild-type cells; see Figs. 4.3A-D for comparison). Despite using cells from MCP-1$^{-/-}$ mice, MCP-1/CCL2 still appeared to contribute to the overall variance of the response to cellular stress. However, this chemokine plays a less prominent role, with its coefficients causing it to be found closer to the origin when projected into principal component space. In normoxia lysates, all inflammatory mediators seemed to associate along the strongest directions of covariance, led by GM-CSF. KC/CXCL1 was the exception, characterizing the secondary response (Fig. 4.11). In hypoxia lysates, the primary response was dominated by IFN-γ, but included most other mediators to varying degrees. A secondary response was characterized by a cluster containing KC/CXCL1, VEGF, IL-4, and IP-10 (Fig. 4.11). In normoxia supernatants, a cluster containing KC/CXCL1 and VEGF was associated with the primary response, while in hypoxia supernatants, the primary response was characterized by two opposing clusters: KC/CXCL1, VEGF, and others oppose IL-6 and IL-2 along the strongest direction of covariance (Fig. 4.11D). Overall, in MCP-1$^{-/-}$ hepatocyte lysates, all inflammatory mediators generally co-varied together. In cells exposed to either hypoxia or normoxia, a secondary signal that was uncorrelated to the first was carried by a set of mediators including KC/CXCL1, but not MCP-1/CCL2. In MCP-1$^{-/-}$ hepatocyte supernatants, we observed an anti-correlated response consisting of KC/CXCL1 and VEGF.

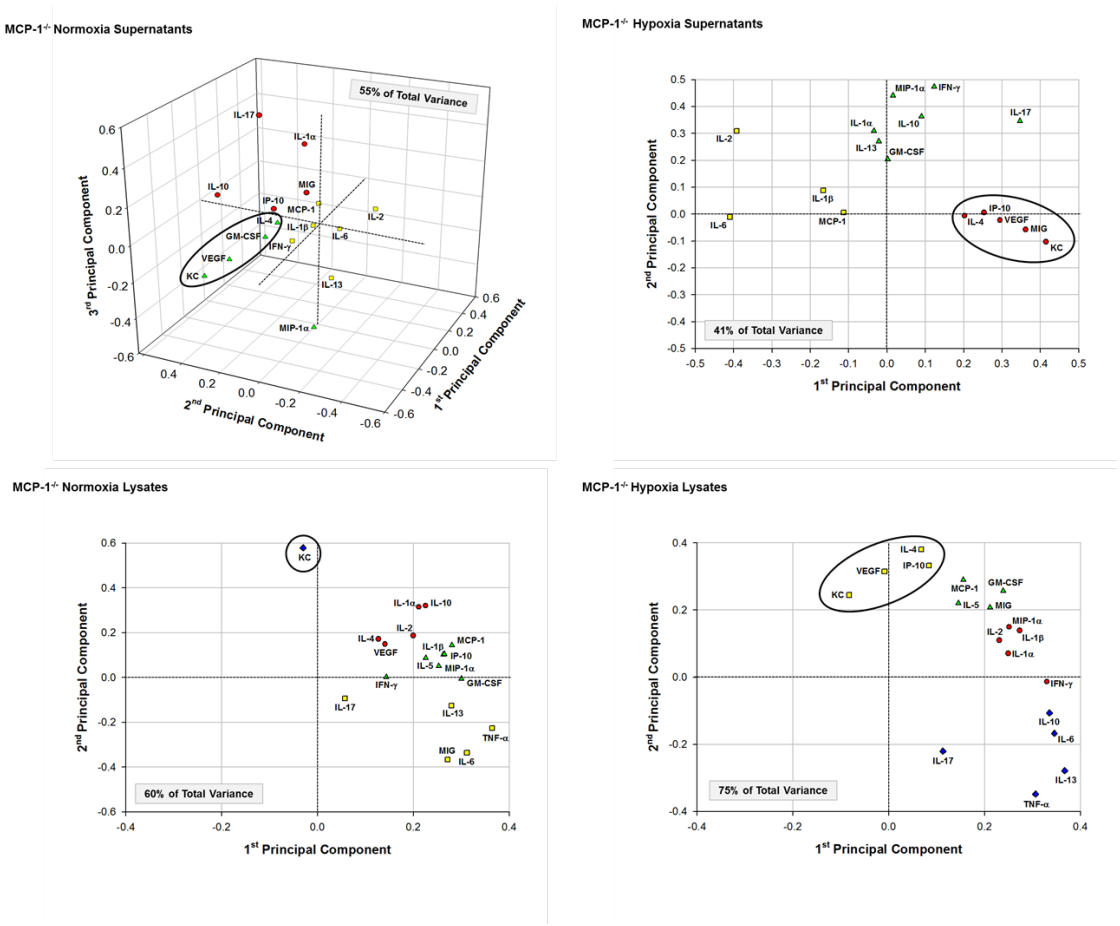

Figure 4.11. The grouping of significant inflammatory mediators according to k-means clustering.
Panels are arranged as follows: (A) normoxia lysate, (B) hypoxia lysate, (C) normoxia supernatant, and (D) hypoxia supernatant. (The percentage of total variance corresponding to each analysis is shown on the top of the graphs).

As in the analysis of the responses of wild-type hepatocytes to cells stress, and in order to synthesize the outcomes of the hierarchical and k-means clustering methods in the MCP-1$^{-/-}$ hepatocytes, we next performed meta-clustering. In contrast to the same analysis in wild-type cells (see Fig. 2.5 for comparison), IL-1β and MCP-1/CCL2 clustered together across all 4 experimental conditions (Fig. 4.12).

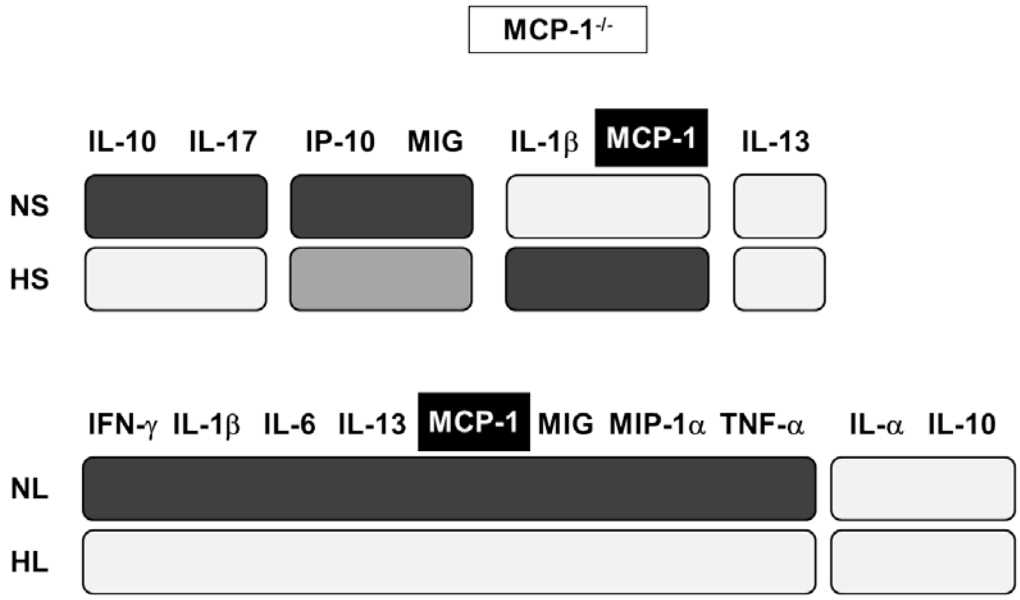

Figure 4.12. Comparison of the outcomes of the hierarchical and k-means clustering methods using meta-clustering.
The shading of the boxes indicates the grouping of the inflammatory mediators that exhibited the same segregation pattern across all methods.

4.4.5 Dynamic Network Analysis of inflammatory mediators produced by normoxic and hypoxic mouse hepatocytes isolated from MCP-1$^{-/-}$ mice

We next carried out DyNA of lysates and supernatants from normoxic and hypoxic MCP-1$^{-/-}$ hepatocytes. A summary of the this analysis, showing the principal inflammatory mediator "hubs" during the five time frames (1-3 h, 3-6 h, 6-24 h, 24-48 h, and 48-72 h), is shown in Figs. 4.13 (normoxia) and 4.14 (hypoxia). The total number of connections resulting from this analysis is shown in Fig. 4.15. This analysis suggested a significant decrease in the number of connections (Figs. 4.13-14) in both lysates and supernatants of normoxic cells and in hypoxia supernatants as compared to wild-type hepatocytes (Figs. 4.6-7). While in normoxia supernatants KC/CXCL1 was the most significantly changed mediator (with nearly zero connections across

all time points; Fig. 4.13), in hypoxia supernatants this chemokine was a central node without connections only at 24-72 h (Fig. 4.14). In normoxia lysates, IL-6 was the most significantly changed mediator, but had no connections to other mediators (Fig. 4.13). However, this cytokine was the most connected mediator (along with IFN-γ) in hypoxia lysates at all-time intervals after 6 h (Fig. 4.14). DyNA suggested a clear lessening in the total number of dynamic connections among inflammatory mediators in MCP-$1^{-/-}$ cells (Fig. 4.15) as compared to wild-type hepatocytes (Fig. 4.8). The most connected inflammatory mediator in MCP-$1^{-/-}$ hepatocytes was IL-6, but only in hypoxia lysates (Fig. 4.8).

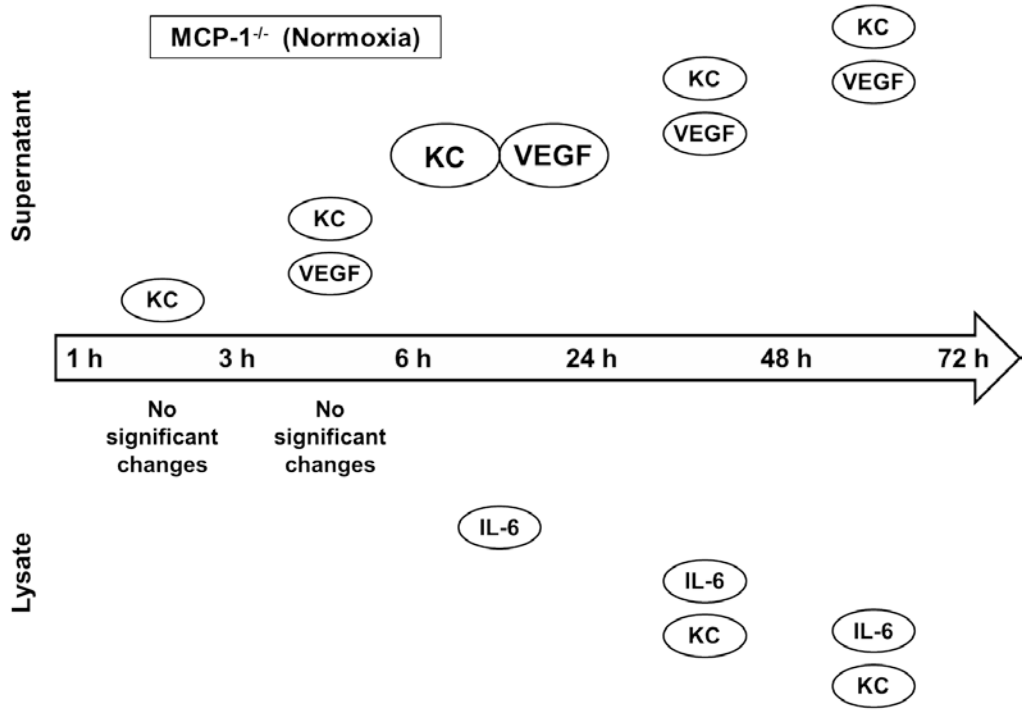

Figure 4.13. Dynamic Network Analysis (DyNA) of inflammatory mediators produced by normoxic mouse hepatocytes isolated from MCP-1$^{-/-}$ mice.
Primary hepatocytes from isolated from MCP-1$^{-/-}$ mice were cultured under normoxic conditions (1-72 h) followed by measurement of inflammatory mediators in both lysates and supernatants as described in *Materials and Methods*. After data normalization, DyNA was performed for both normoxic lysates and normoxic supernatants during each of the following five time frames: 1-3 h, 3-6 h, 6-24 h, 24-48 h, and 48-72 h as indicated. The most connected mediators—those that were correlated with the greatest number of other mediators in a time step—are shown here. Each mediator's node size is proportional to the number of connections it has in a given time interval. When correlated to other represented mediators, they are illutrated as touching. Other highly connected mediators that are not connected to mediators illustrated here are show not touching.

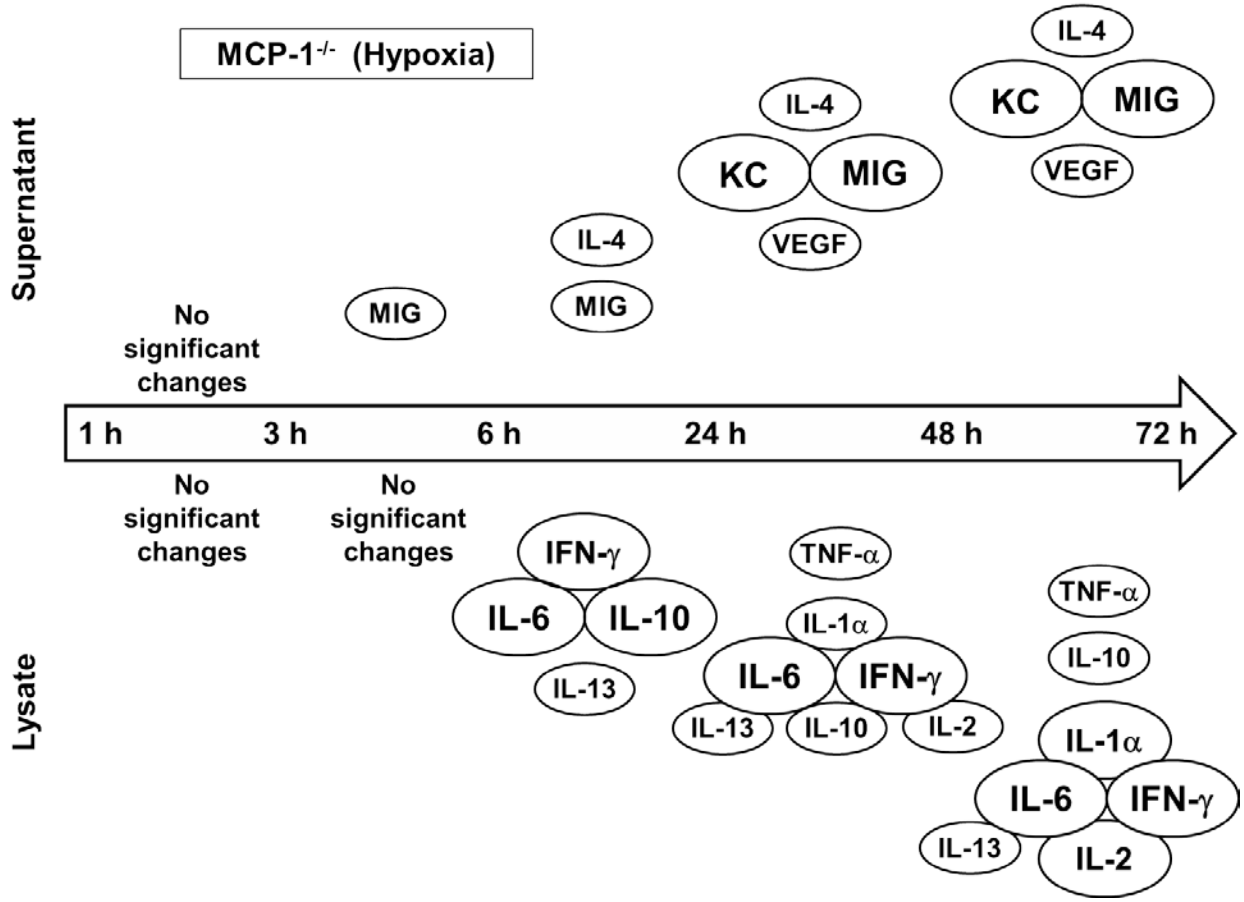

Figure 4.14. Dynamic Network Analysis (DyNA) of inflammatory mediators produced by hypoxic mouse hepatocytes isolated from MCP-1$^{-/-}$ mice.
Primary hepatocytes from isolated from MCP-1$^{-/-}$ mice were cultured under hypoxic conditions (1-72 h) followed by measurement of inflammatory mediators in both lysates and supernatants as described in *Materials and Methods*. After data normalization, DyNA was performed for both hypoxic lysates and hypoxic supernatants during each of the following five time frames: 1-3 h, 3-6 h, 6-24 h, 24-48 h, and 48-72 h as indicated. The most connected mediators—those that were correlated with the greatest number of other mediators in a time step—are shown here. Each mediator's node size is proportional to the number of connections it has in a given time interval. When correlated to other represented mediators, they are illutrated as touching. Other highly connected mediators that are not connected to mediators illustrated here are show not touching.

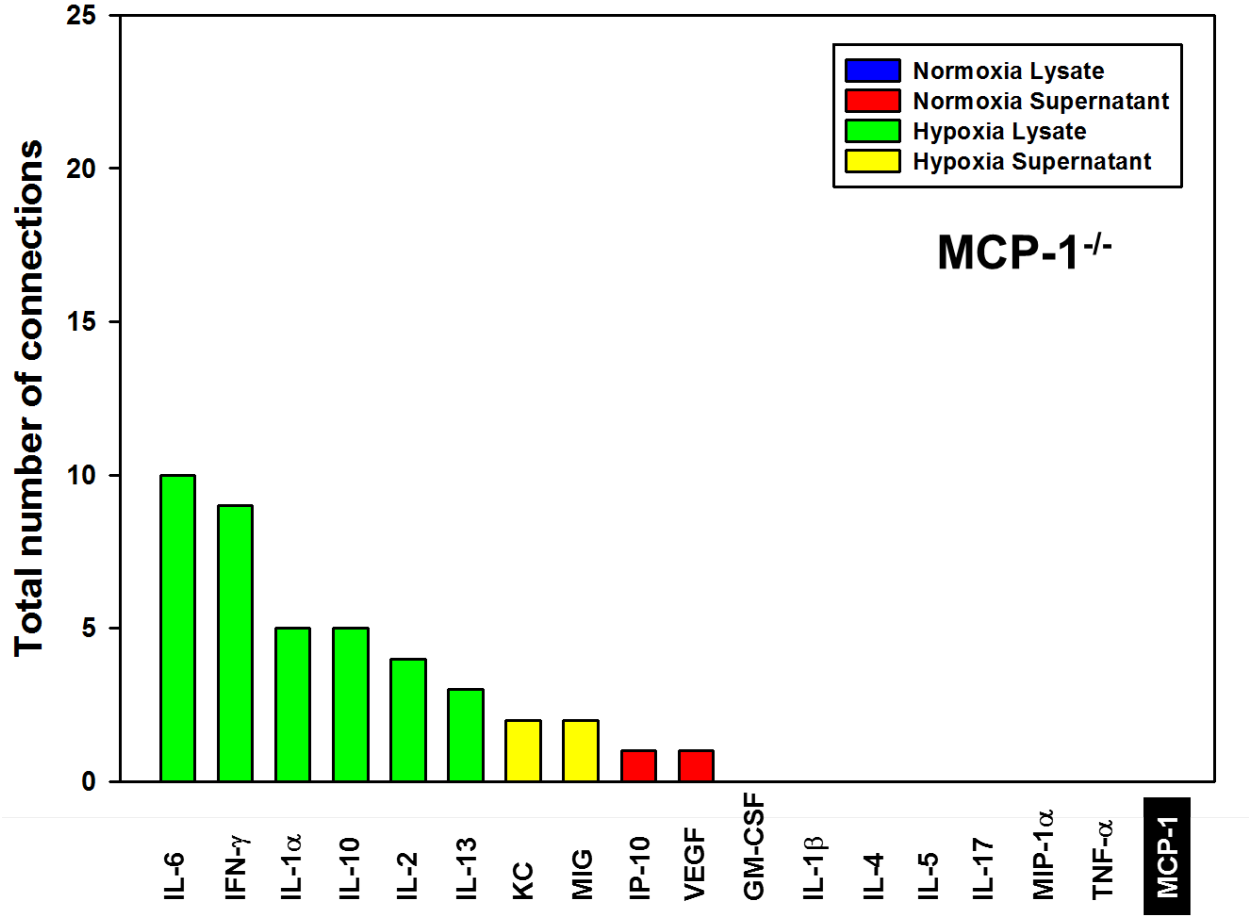

Figure 4.15. Total Connections in DyNA analyses across experimental conditions in MCP-1$^{-/-}$ cells.
The stacked bars represent the total number of connections for each inflammatory mediator over all time intervals. Each color stands for one experimental condition. Notably, no mediator had connections in more than one experiemental condition in MCP-1$^{-/-}$ cells.

4.4.6 Differential expression and release of IL-6 in mouse hepatocytes: *wild-type vs. MCP-1*$^{-/-}$

Because one-way ANOVA and DyNA revealed that the most significant changes in inflammatory mediator production and release were observed for MCP-1/CCL2 and IL-6, we decided to examine the time courses for IL-6 in more detail. Primary hepatocytes from wild-type

and MCP-1$^{-/-}$ mice were cultured under normoxic and hypoxic conditions for 1-72 h followed by Luminex™ analysis in both the whole-cell lysates and supernatants as described in the *Materials and Methods*. IL-6 levels were significantly lower in both normoxia lysates (Fig. 4.16A) and supernatants (Fig. 4.16B) of MCP-1$^{-/-}$ hepatocytes as compared to wild-type controls. In hypoxia lysates, IL-6 showed no significant changes in protein expression (though the values tended to decrease after the 24 h) (Fig. 4.16C). In contrast, IL-6 increased over time in supernatants from wild-type hepatocytes, but not in MCP-1$^{-/-}$ cells (Fig. 4.16D). These results suggest that the differential expression and release of IL-6 in mouse hepatocytes depends, at least in part, on MCP-1/CCL2.

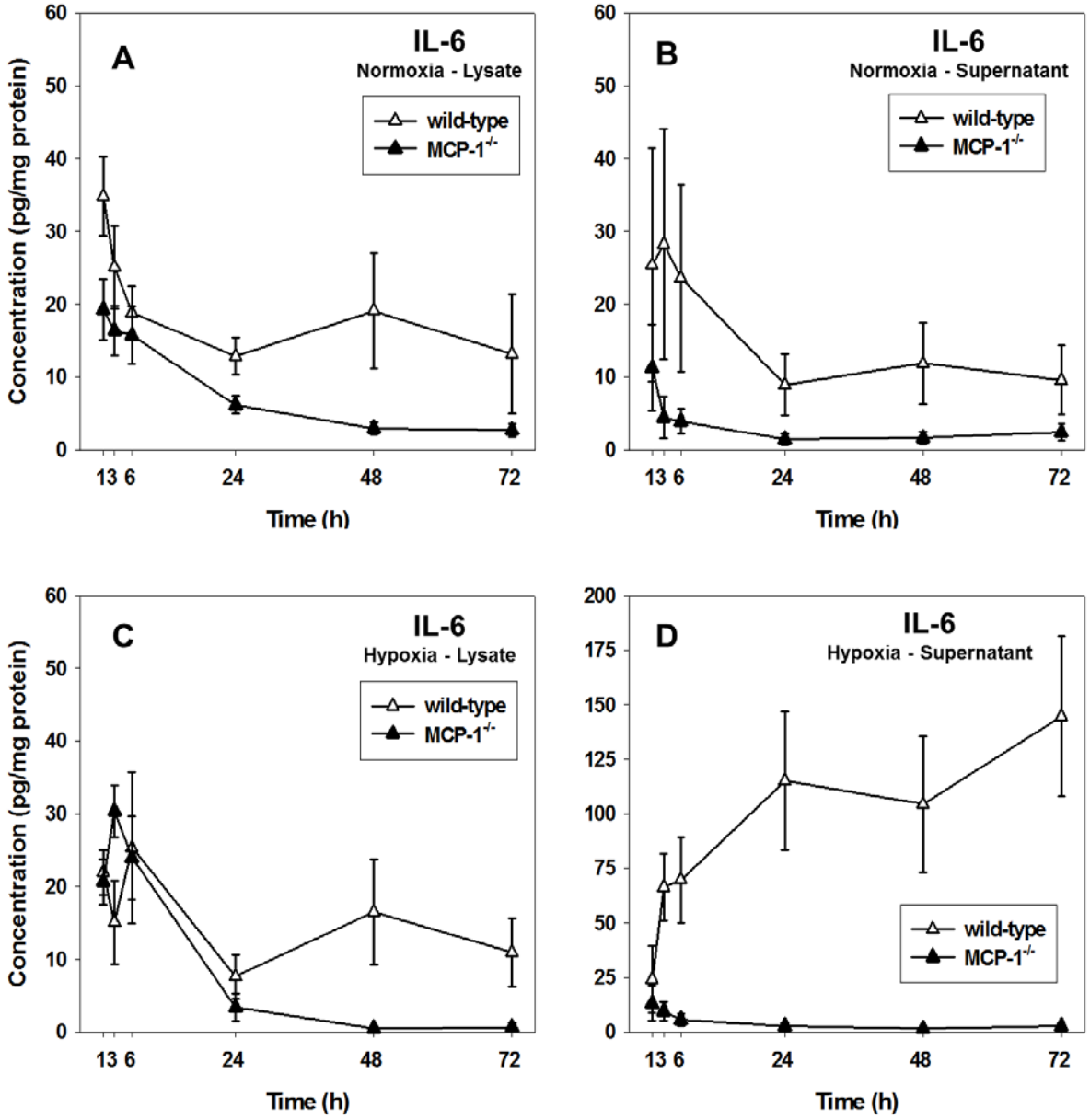

Figure 4.16. Time-dependent expression and release of IL-6 in mouse hepatocytes.
Primary hepatocytes from wild-type (open symbols) and MCP-$1^{-/-}$ (closed symbols) mice were cultured under normoxic (Panels A and B) and hypoxic (Panels C and D) conditions for 1, 3, 6, 24, 48 and 72 h followed by measurement of IL-6 in both lysates and supernatants using the Luminex™ xMAP technology as described in *Materials and Methods.* Results are the mean ± SEM (n=4-8 independent experiments, analyzed by Two-way ANOVA, $P<0.05$ (wild-type vs. MCP-$1^{-/-}$) for all conditions except hypoxia lysates, Panel C).

4.4.7 *In situ* hepatocyte expression of MCP-1 and IL-6 is attenuated in MCP-1$^{-/-}$ cells

The differential expression of MCP-1 and IL-6 in both wild-type and MCP-1$^{-/-}$ cells was confirmed using confocal immunofluorescence (Fig. 4.17A). Quantitative analysis of the images (Fig. 4.17B) revealed that MCP-1 is indeed elevated in wild-type hepatocytes as compared to MCP-1$^{-/-}$ cells, with much higher levels in normoxia vs. hypoxia, confirming the results obtained by Luminex measurements (see Fig. 4.1). Similarly, cellular IL-6 levels were lower in the MCP-1$^{-/-}$ cells as compared to wild-type hepatocytes, especially under hypoxic conditions (Fig. 4.17B).

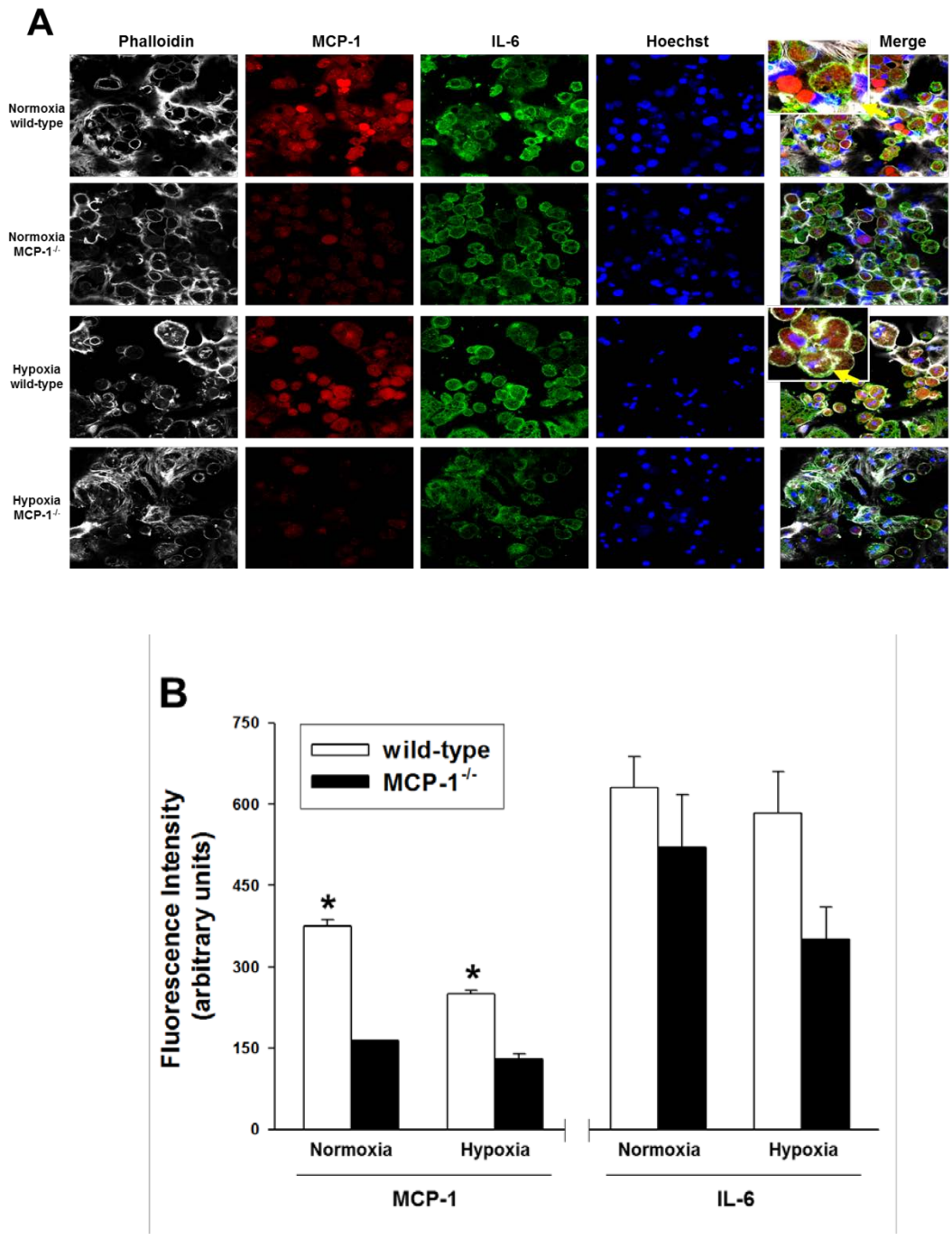

Figure 4.17. Differential expression of MCP-1 and IL-6 in wild-type and MCP-1$^{-/-}$ hepatocytes.
Primary hepatocytes isolated from wild-type and MCP-1$^{-/-}$ mice (n=3 each) were cultured under normoxic and hypoxic conditions for 48 h in three independent experiments. The cells were then fixed and processed for confocal immunofluorescence imaging as described in the *Materials and Methods*. (A) Fluorescent labeling: Phalloidin (white), MCP-1 (red), IL-6 (green), Hoechst (blue). (B) Quantification of immunostained cells (fluorescence intensity from 600-700 hepatocytes from 3 independent fields, n=3 coverslips/experiment). Results are the mean ± SEM (*P<0.001 wild-type vs. MCP-1$^{-/-}$, analyzed by *t*-test).

4.4.8 Elevated plasma MCP-1/CCL2 levels as biomarker for morbidity in human trauma/hemorrhage

Our *in vitro* findings suggested that MCP-1/CCL2 is central to the production and release of hepatocyte inflammatory mediators in response to cellular stress (key among them being IL-6). Since the liver is a central organ in the *in vivo* response to T/HS, and since IL-6 has been identified consistently as a marker of negative outcomes in T/HS, we next evaluated the potential of plasma MCP-1/CCL2 levels to serve as a biomarker for morbidity in blunt trauma patients. Indeed, an analysis of a cohort of 30 trauma patients revealed that patients could be segregated between survivors and non-survivors based on plasma MCP-1 levels within the first 24 h (Fig. 4.18).

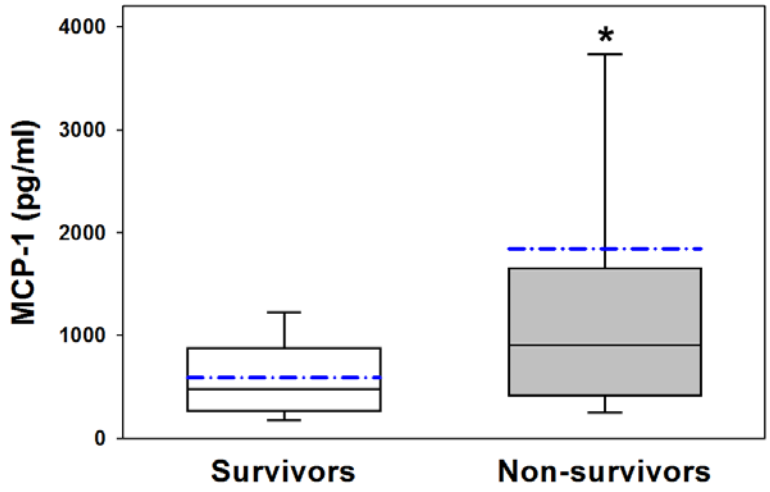

Figure 4.18: MCP-1 levels in plasma samples from trauma patients
Survivors vs. non-survivors, n=15 each taken within the first 24 h after trauma as described in the *Materials and Methods*. Results represent the mean ± SEM (The dotted line represents the mean value, **P*=0.001, survivors vs. non-survivors analyzed by *t*-test).

We next studied a cohort of 31 hypotensive patients matched with 31 normotensive patients as described in the *Materials and Methods*. We first sought to verify our *in vitro*/*in silico*-derived hypothesis that MCP-1/CCL2 levels are correlated with IL-6 levels. Plasma MCP-1/CCL2 and IL-6 levels in both patient cohorts are shown in Fig. 4.19. Plotting IL-6 vs. MCP-1/CCL2 plasma concentrations for the trauma patient cohort as a whole (n=62) suggested that circulating IL-6 levels in these patients could be segregated into two groups based on circulating MCP-1/CCL2 levels: low MCP-1 (<1000 pg/ml, Panels A-B) and high MCP-1 (>1500 pg/ml, Panels A-B). Furthermore, analysis of the data showed a positive correlation between MCP-1/CCL2 and IL-6 in both normotensive (correlation coefficient= 0.59, Panel A) and hypotensive (correlation coefficient= 0.41, Panel B) blunt trauma patients.

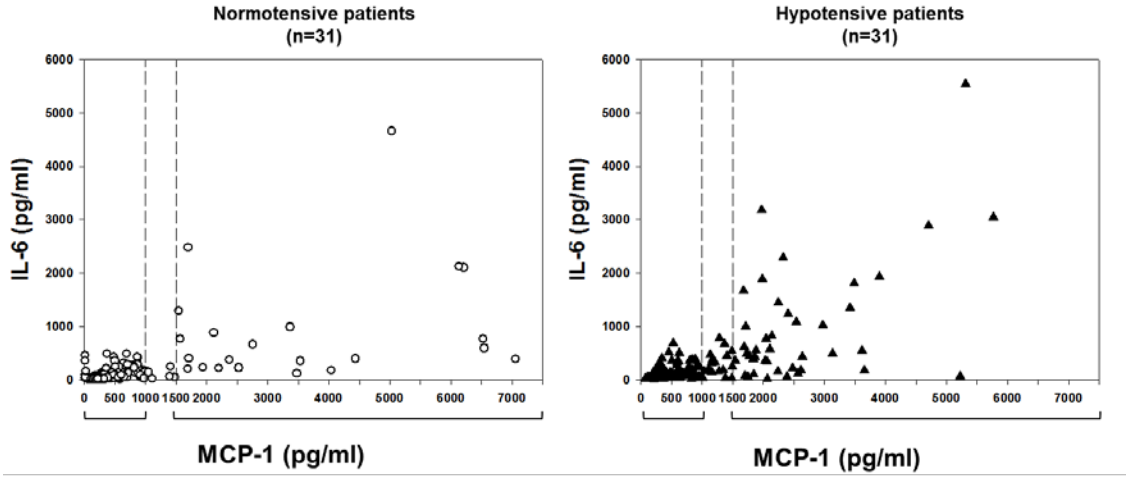

Figure 4.19: Elevated plasma MCP-1/CCL2 levels are associated with morbidity in human trauma/hemorrhage.
Plot of IL-6 vs. MCP-1/CCL2 levels in blood samples from normotensive (A) and hypotensive (B) trauma patients (n=31 each) taken within the first 24 h after trauma, followed by sampling at 48, 72 and 96 h as described in *Materials and Methods*.

We then performed a different grouping irrespective of blood pressure status and based solely on MCP-1/CCL-2 concentrations (<1000 pg/ml and >1500 pg/ml, respectively). This

grouping reduced the study cohort to 46 T/HS patients. We found that T/HS patients with lower circulating MCP-1/CCL-2 levels (Fig. 4.20, left; 400.54 ± 15.75 pg/ml; range: 12.13 - 991.67 pg/ml [n=38;]) have lower circulating IL-6 levels (106.14 ± 8.07 pg/ml; range: 3.42 - 682.11 pg/ml [n=38]) as compared to patients with higher circulating MCP-1/CCL-2 (Fig. 4.20, right; 4098.71 ± 772.85 pg/ml; range: 1486.46 - 26112.26 pg/ml [n=8]) who exhibited higher, though more variable circulating IL-6 levels (1457.67 ± 391.23 pg/ml; range: 26.12 - 10582.37 pg/ml [n=8]).

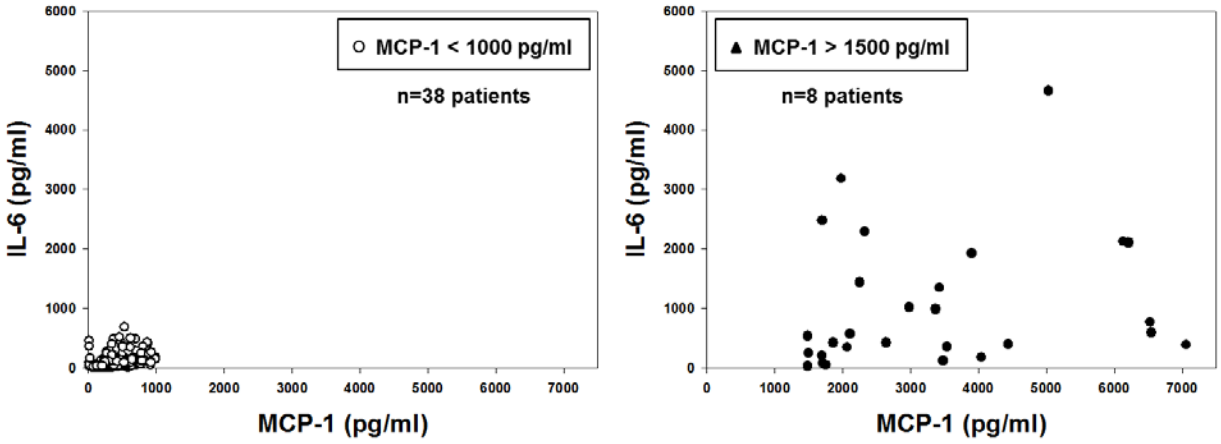

Figure 4.20. Grouping of T/HS patients based on circulating MCP-1/CCL2 levels.
Left hand panel shows MCP-1 values <1000 pg/ml (n=38 patients), right hand panel shows values >1500 pg/ml (n=8 patients).

We next sought to determine if these two cohorts of patients, segregated solely on the basis of circulating MCP-1/CCL-2 levels, exhibited any differences in outcomes. Patients with higher circulating MCP-1 levels had worse outcomes, as indicated by a longer total length of stay (LOS), longer intensive care unit (ICU) LOS, and greater requirement for mechanical ventilation (Fig. 4.21). Interestingly, statistical analysis using two-way ANOVA showed no significant differences between MCP-1/CCL2 levels in the initial cohort of normotensive vs. hypotensive

patients (data not shown), and analysis of the clinical outcomes of the patients segregated based on their normotensive/hypotensive status revealed no differences between normotensive and hypotensive patients (data not shown).

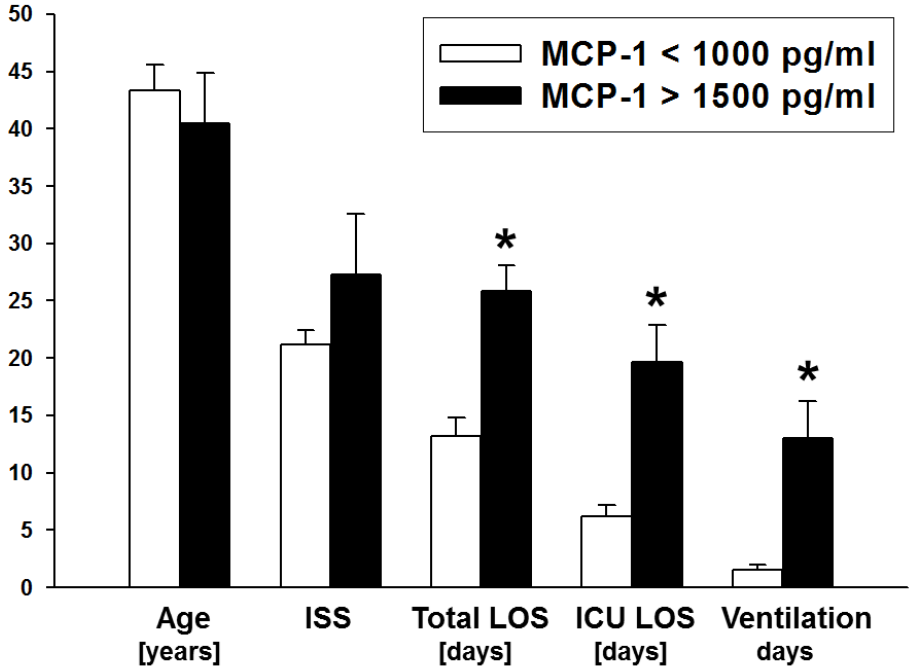

Figure 4.21. Overall demographics of T/HS patients segregated according to plasma MCP-1/CCL2 levels.
Low MCP-1(<1000 pg/ml; [n=38 patients]) vs. high MCP-1 (>1500 pg/ml; [n=8 patients]). Results represent the mean ± SEM. (**P*<0.05, analyzed by Mann-Whitney *U* test, MCP-1<1000 pg/ml vs. MCP-1>1500 pg/ml).

4.5 DISCUSSION

Liver ischemia and subsequent reperfusion, which can occur in T/HS and resuscitation, lead to inflammatory liver injury as well as to the systemic elaboration of inflammatory mediators and subsequent multiple organ dysfunction (37; 72; 79). Liver hypoxia is a primary feature of HS in experimental models (46; 60). Hypoxic stress, however, is but one of a variety of stresses (e.g. endoplasmic reticulum stress and autophagy) encountered by hepatocytes in settings such as T/HS (33) and I/R (35). We therefore reasoned that the analysis of synthesis and secretion of inflammatory mediators by stressed hepatocytes would help in our understanding of the pathophysiology of T/HS and other conditions characterized, at least in part, by hepatic stress.

Our key finding is that a combined *in vitro*/*in silico* analysis of the dynamics of synthesis and secretion of inflammatory mediators points to the chemokine MCP-1/CCL2 as a central coordinator of the inflammatory response of stressed hepatocytes, a finding that allowed us to segregate blunt trauma patients based on circulating levels of MCP-1/CCL2. Importantly, this segregation of patients would have proven ineffective if performed based on the patients' normotensive/hypotensive status post-injury.

Chemokines (also known as chemotactic cytokines) are small cytokine-like, heparin-binding molecules which play a major role in orchestrating immune and stem cell infiltration into the liver in response to acute and chronic injuries (37; 78). Hepatic chemokines are released not only during inflammatory injury (infection, drug intoxication), but these mediators play a key role in the activation and proliferation of liver-resident cells (including hepatocytes, stellate cells and endothelial cells) and thus help drive hepatic regeneration after partial hepatectomy (25; 78).

In our studies, multiple chemokines were synthesized by stressed hepatocytes. Though chemokines are often thought to be highly redundant in their actions, MCP-1/CCL2 was the only mediator that exhibited significant changes in both normoxia and hypoxia, and in both cell lysates (denoting cellular expression) and supernatants (denoting secretion by cells). Our findings of perturbed dynamic inflammatory networks in MCP-1$^{-/-}$ mice supports the hypothesis that this chemokine plays a central driving role in the hepatocyte response to stress. The presence of a weaker, but noticeable, MCP-1/CCL2 protein band in the lysates from hypoxic MCP-1$^{-/-}$ cells raises the possibility that the actual effects of MCP-1/CCL2 might be even more pronounced.

MCP-1 or chemokine (C-C motif) ligand 2 (CCL2) is one of the best-known CC chemokines. It was first identified as a monocyte-specific chemoattractant, and was later shown to attract memory T lymphocytes and NK cells. Binding to its seven transmembrane G-protein-coupled receptor CCR2 (CC chemokine receptor 2) results in signaling events that lead to the recruitment of monocytes to inflammation in a variety of *in vivo* experimental models of infection and injury (24; 42). In addition to recruiting monocytes, MCP-1/CCL2 can also activate macrophages and endothelial cells and has been implicated in the attraction of neutrophils and the generation of neutrophil-dependent tissue damage (42). Lu *et al.* showed that despite normal numbers of circulating leukocytes and resident macrophages, MCP-1$^{-/-}$ mice were specifically unable to recruit monocytes 72 h after intraperitoneal thioglycollate administration, indicating that MCP-1 is essential for monocyte recruitment and the expression of cytokines related to T helper responses *in vivo* (52).

Hepatic MCP-1/CCL2 can be upregulated *in vivo* by I/R (103) as well as by bacterial endotoxin (16), and in isolated mouse hepatocytes by hypoxia (49) and the present study). The

expression of MCP-1/CCL2 in normoxic primary cultured hepatocytes has been thought to be due to the stress of the cell isolation procedure (96), and we likewise found elevated MCP-1/CCL2 in normoxic hepatocytes. The effects of MCP-1/CCL2 in the liver range from protective (e.g. in experimental acetaminophen-induced injury) to detrimental (e.g. during experimental I/R injury) (49).

In addition to MCP-1/CCL2, our studies suggest that IL-1α, IL-6, KC/CXCL1, and MIG/CXCL9 exhibit the most significant dynamic changes in stressed hepatocytes. Our results suggest that MCP-1/CCL2 regulates the production of these other inflammatory mediators. This hypothesis is supported by prior studies, in which the expression of hepatic pro-inflammatory cytokines (including IL-6 and KC/CXCL1) was induced in alcohol-fed wild-type, but inhibited in MCP-1$^{-/-}$ animals (57). In support of this central role for KC/CXCL1, Frink *et al* showed that neutralization of this chemokine ameliorated liver damage after T/HS in mice. These authors also showed that MCP-1/CCL2 causes organ damage via upregulation of KC/CXCL1, supporting our findings of a network of hepatic inflammation that involves these two chemokines. However, the exact source of KC/CXCL1 remained unknown (38), and our present study suggests that hepatocytes are a key source of this chemokine.

Interleukin-6 is a biomarker of poor outcome in trauma (54; 106). It is therefore notable that IL-6 was highly correlated with MCP-1/CCL2 in T/HS patients, and that the production of IL-6 by hypoxic hepatocytes was essentially abolished in the absence of endogenous MCP-1/CCL2. Interestingly, a recent study suggests the presence of a positive feedback loop involving IL-6 and MCP-1/CCL2 in a setting of vascular inflammation (89).

The use of applied mathematical models and algorithms constitute a novel tool for interpreting complex biological data. In 2005, a pioneering study in this field constructed a

systems model comprising a large number of intracellular signaling events directly linked to outputs associated with apoptosis to study how molecular information is processed as a network (45). Prior studies have also utilized advanced computational analyses to discern key features of the inflammatory biology of hepatocytes. For example, Alexopoulos *et al* studied 26,000 protein state measurements from isolated primary human hepatocytes and HepG2 liver cancer cells exposed to growth factors or inflammatory mediators, yielding interaction graphs using multilinear regression (2). The authors suggested major differences between primary and transformed hepatocytes with respect to toll-like receptor-4 signaling and NF-κB-dependent secretion of chemokines and cytokines, and suggested, as we do here, that combined *in vitro*/*in silico* analyses can yield novel insights into hepatocyte biology (2). More recently, Boolean logic models of immediate-early signaling in liver cells were created by training a literature-based prior knowledge network against biochemical data obtained from primary human hepatocytes as well as four hepatocellular carcinoma cell lines exposed to combinations of cytokines and small-molecule kinase inhibitors (77). Our present study extends this paradigm to define key nodes in the stress-induced inflammatory networks induced in hepatocytes, as well as suggesting higher-order, clinically-applicable insights. Indeed, this study points to various similarities between hepatocytes *in vitro* and T/HS *in vivo*. For example, as in the present study, we found in a prior study of experimental T/HS in mice that together with MIG/CXCL9, IL-6 was highly elevated but disconnected from other inflammatory mediators (63). Our present study raises the possibility that MCP-1/CCL2 is the stimulus for post-HS MIG/CXCL9 and IL-6.

In the present study, we developed a novel algorithm for consensus clustering of multiple data-driven analyses of dynamic responses. We hypothesized that those inflammatory mediators exhibiting the most coordination across experimental conditions could be important drivers or

indicators of that process. The strategy we employed was to extract patterns from dynamic data, and to assess the measure of similarity across multiple dynamic patterns. To distill the most important information from three independent clustering results over 18 mediators for each of 4 experimental conditions, we filtered the results by discarding inflammatory mediators that showed inconsistent segregation patterns across the three analyses. A consensus clustering containing only the mediators whose coordination patterns in which we could be most confident was the basis of comparison across experimental conditions. This method identified MCP-1/CCL2 as the most relevant mediator in our studies.

This novel approach to data-driven modeling suggested the key aspect of our study, namely that trauma patients can be segregated into high- vs. low-producers of MCP-1/CCL2, and that circulating levels of MCP-1/CCL2 are better discriminators of outcome post-trauma than hypotension in our moderately-injured patients. This was true despite the fact that even a brief period of hypotension was suggested to elevate post-trauma morbidity and mortality in injured patients (109). Collectively, our results provide a systems view of the hepatocyte inflammatory response to cell stress, with implications for ischemia and hemorrhage, and point to hepatocytes as a likely cellular source of cytokines/chemokines in the inflammatory response. Furthermore, these results highlight the capacity of data-driven analyses for suggesting novel, clinically-relevant targets.

5.0 CONCLUSIONS

In this dissertation, I have explored the role of computational methods in elucidating biological information from complex systems. In each problem, the goal was to bridge from a confounding biological problem to a clinical solution using computational tools to shed insights along the way.

In an *in vitro* model of cellular stress, we identified a small set of interacting mediators that were elucidated consistently and with similar patterns. We showed that without one of those key mediators, the entire inflammatory milieu elucidated during cell stress was shifted. And most importantly, we showed that there was a strong correlation between levels of this mediator and inflammatory outcomes in human trauma patients. High levels of MCP-1 were associated with high levels of IL-6, a mediator that has been shown to be a hallmark of inflammation. Furthermore, high MCP-1 levels correlated with non-survival outcomes in human trauma patients.

An agent-based model of pressure ulcer formation successfully incorporated multiple levels of mechanistic information and produced tissue-realistic simulations that were comparable to images of pressure ulcers in people with spinal cord injury (SCI). This model was successfully used as a hypothesis testing platform to assess the viability of treatment strategies, including dosage and timing considerations. The visual output of the model also predicted morphological features (e.g. satellite ulcers, irregular shaped ulcer edges) that were observed in patients, but not

coded into the model. And, importantly, the inflammatory dynamics in the model exhibited the ability to reach two different steady states from the same initial conditions: resolving inflammation or unresolving, damaging positive feedback.

We then used computational tools to further explore the behaviors of the model, in order to pinpoint the players involved in the decision point between resolving and damaging inflammatory paradigms. Simulations provided an unending supply of training and testing data for classifiers that were trained on time series of model components (cells, mediators, cell properties, etc.). And finally, taking advantage of the spatial output of the model, local information could be gleaned in order to understand the decision process from the point of view of a single cell, rather than a whole tissue. The most natural next step with this ABM is to use image analysis techniques to bridge between the spatial output of the model and the clinical images that are the most reliable source of data for comparison. This model could continue to serve as a hypothesis-testing platform or with some increased functionality could be put to use as a diagnostic tool.

All of the experiments described here represent waypoints on a path from data to clinical interventions. From data, patterns can be inferred, and from patterns mechanisms. Mechanisms can be synthesized with other mechanisms to generate hypotheses. And after validating the hypothesis-generating platform, it can be used to test new hypotheses and strategies before developing them for clinical (or even animal) trials. Another important part of this arc is the idea that these transitions from one medium to the next do not happen in isolation; we are not suggesting an automated pipeline. Instead, experts are chauffeuring the insights along, checking that the outputs generated make sense in the context, and using domain knowledge and experience to interpret them and decide in what form they are passed to the next step. We have

illustrated a few parts of this path, but all of them are ongoing, if disjointedly. Computational methods are being used to boost the power of experimental results, allowing data from disparate sources to be related and new inferences to be made.

APPENDIX A

PUABM PSEUDOCODE

Key:

AGENTS

Agents' properties

DATA LAYERS – In rules, this refers to the local value of a data layer

User-defined-parameters

functions-defined-inside-PUABM

∝: "is proportional to"

At tick t, do the following:

- Reset tissue-health = 0
- Reset total-damage = 0
- If t mod *shear-interval* == 0, apply or release shear
- Data Layers diffuse: *TNF*, *TGF*, *IL-1B*, O_2, *DAMPs*, *ROS, STEROID, ANTIDAMPS*
- Data Layers evaporate: *TNF*, *TGF*, *IL-1B*, O_2, *DAMPs*, *OXIDASE*, *ROS, ANTIOXIDANT, STEROID, ANTIDAMPS*
- If t mod *pressure-interval* == 0, apply or release pressure by changing values of data layer, *PRESSURE*
- In a randomly determined order,
    - **EPITHELIAL CELLS** make-step:

- **Border** = false
- **Velocity** = 0
- If t > *antidamps-onset* and [(t – *antidamps-onset*) mod *antidamps-reapply* == 0], set *ANTIDAMPS* = *antidamps-dose*
- If **alive**, epithelial-function:
    - Set *ANTIOXIDANT* = *antiox-level*
    - If O_2 < 0.75, increase *OXIDASE* 0.01
    - If O_2 > 0 and *OXIDASE* > 0, make *ROS* ∝ O_2 and *OXIDASE*
    - If *ANTIOXIDANT* > 0 and *ROS* > 0
        - decrease *ROS* ∝ *ANTIOXIDANT* and *ROS*
        - decrease *ANTIOXIDANT* ∝ *ANTIOXIDANT* and *ROS*
    - If *ANTIDAMPS* > 0 and *DAMPS* > 0: with probability *damps-bind*
        - Decrease *DAMPS* ∝ *ANTIDAMPS* and *DAMPS*
        - Decrease *ANTIDAMPS* ∝ *ANTIDAMPS* and *DAMPS*
    - If *ROS* > 0, increase *injury-index* ∝ *ROS*
    - If *injury-index* > *injury-threshold* decrease **life** 90%
    - Decrease **life** ∝ (shear force)^2
    - Decrease **life** ∝ *TNF*, *IL-1B*, 1 - O_2
    - Increase **life** ∝ *TGF*, O_2
    - Set **color**
    - If **life** < 0
        - Increase total-damage 1
        - **Alive** = false
        - Die, exit
    - **Life** > 100 → 100
    - If **life** < 100, increase total-damage ∝ **life**
    - Increase tissue-health ∝ **life**
    - Increase *DAMPs* ∝ exp(-**life**/100)
- Else,

- If neighbors **alive**, **border** = true
- Increase total-damage 1

o **BLOOD VESSELS** make-step:

- **Size** scales ∝ (1 - *PRESSURE*)^4
- If one or fewer neighboring **EPITHELIAL CELLS** are **alive**, die
- Hatch one **MACROPHAGE** with probability ∝ **size**
- Hatch one **NEUTROPHIL** with probability ∝ **size**
- If d > 0.0001, hatch one **NEUTROPHIL**
- Increase *OXYGEN* ∝ **size**
- If t > *steroid-onset*, set *STEROID* = *steroid-dose*

o **MACROPHAGES** make-step:

If *STEROID* > *mac-steroid-toxicity*

- if **state** ==1, decrease activated-macrophages1 by 1
- if **state** ==2, decrease activated-macrophages2 by 1
- die, exit

Else:

- Wiggle 45°
- Jump
- Sniff *TGF* with probability 0.5
- Else, with probability 0.3:
  - Sniff *TNF*, then
  - Sniff *IL-1B*
- Else don't sniff anything
- If *TNF* > *tnf-activation-mac* or *IL-1B* > *il1-activation-mac*
  - **state** = 1 with probability = 1 / (1 + *il1-activation-mac*)
  - increase activated-macrophages1
  - **color** = red
  - if previous **state** == 2, decrease activated-macrophages2 by 1
- If *TGF* > *tgf-activation-mac* or *IL-1B* > il1-m2-activation
  - **state** = 2 with probability = 1/1+(*tgf-activation-mac*)

- increase activated-macrophages2
- **color** = green
- if previous **state** == 1, decrease activated-macrophages1 by 1

▪ decrease **age** 1

▪ if **age** < 0

- if **state** ==1, decrease activated-macrophages1 by 1
- if **state** ==2, decrease activated-macrophages2 by 1
- die, exit

o **NEUTROPHILS** make-step:

If *STEROID* > *pmn-steroid-toxicity*

- increase *ROS* 0.001
- if **state** ==1, decrease activated-neutrophils 1
- die, exit

Else:

▪ Wiggle 45°

▪ Jump

▪ Sniff *DAMPs*

▪ If **state** == 0 and *DAMPs* > *danger-pmn-activation*

- **State** = 1
- **Color** = black
- Increase **age** 3-8 ticks

▪ If **state** == 1, increase *TNF* ∝ (1+*TNF*)/(1+*TGF*)

▪ If **state** == 0

- If *TGF* < 0.001
  - o survey **EPITHELIAL CELLS** in a neighborhood of radius 1
  - o if their mean **life** < 90, **state** == 1

▪ decrease **age** 1

▪ if **age** < 0

        - increase *ROS* 0.001
        - if **state** == 1, decrease activated-neutrophils
        - die, exit
- Query values of: total-TNF, total-TGF, total-danger, total-pressure, total-oxygen, blood-flow, total-antioxidant, total-antidamps, total-ROS, total-oxidase, activated-macrophages1, activated-macrophages2, activated-neutrophils, epithelial-number

BIBLIOGRAPHY

1. **Adra S, Sun T, MacNeil S, Holcombe M and Smallwood R**. Development of a three dimensional multiscale computational model of the human epidermis. *PLoS ONE* 5: e8511, 2010.

2. **Alexopoulos LG, Saez-Rodriguez J, Cosgrove BD, Lauffenburger DA and Sorger PK**. Networks Inferred from Biochemical Data Reveal Profound Differences in Toll-like Receptor and Inflammatory Signaling between Normal and Transformed Hepatocytes. *Molecular & Cellular Proteomics* 9: 1849-1865, 2010.

3. **Allman RM**. Pressure ulcer prevalence, incidence, risk factors, and impact. *Clinics in geriatric medicine* 13: 421, 1997.

4. **An G**. In-silico experiments of existing and hypothetical cytokine-directed clinical trials using agent based modeling. *Crit Care Med* 32: 2050-2060, 2004.

5. **An G**. Closing the scientific loop: bridging correlation and causality in the petaflop age. *Science translational medicine* 2: 41ps34, 2010.

6. **An G, Bartels J and Vodovotz Y**. *In silico* augmentation of the drug development pipeline: Examples from the study of acute inflammation. *Drug Dev Res* 72: 1-14, 2011.

7. **An G, Mi Q, Dutta-Moscato J, Solovyev A and Vodovotz Y**. Agent-based models in translational systems biology. *WIRES* 1: 159-171, 2009.

8. **An G, Nieman GF and Vodovotz Y**. Computational and systems biology in trauma and sepsis: current state and future perspectives. *Int J Burn Trauma* 2: 1-10, 2012.

9. **An G**. Small to large, lots to some, many to few: In silico navigation of the Translational Dilemma. *Crit Care Med* 40: 1334, 2012.

10. **An G and Christley S**. Addressing the Translational Dilemma: Dynamic Knowledge Representation of Inflammation using Agent-based Modeling. *Critical Reviewsâ„¢ in Biomedical Engineering* 2012.

11. **Andersson U and Tracey KJ**. HMGB1 is a therapeutic target for sterile inflammation and infection. *Annu Rev Immunol* 29: 139-162, 2011.

12. **Arciero JC, Mi Q, Branca MF, Hackam DJ and Swigon D**. Continuum Model of Collective Cell Migration in Wound Healing and Colony Expansion. *Biophysical Journal* 100: 535-543, 2011.

13. **Armstrong DG, Ayello EA, Capitulo KL, Fowler E, Krasner DL, Levine JM, Sibbald RG and Smith AP**. New opportunities to improve pressure ulcer prevention and treatment: implications of the CMS inpatient hospital care present on admission indicators/hospital-acquired conditions policy: a consensus paper from the International Expert Wound Care Advisory Panel. *Advances in skin & wound care* 21: 469-478, 2008.

14. **Ayello EA and Lyder C**. A new era of pressure ulcer accountability in acute care. *Advances in skin & wound care* 21: 134-140, 2008.

15. **Bao F, Bailey CS, Gurr KR, Bailey SI, Rosas-Arellano MP, Dekaban GA and Weaver LC**. Increased oxidative activity in human blood neutrophils and monocytes after spinal cord injury. *Experimental neurology* 215: 308-316, 2009.

16. **Barclay D, Zamora R, Torres A, Namas R, Steed D and Vodovotz Y**. A simple, rapid, and convenient Luminex-compatible method of tissue isolation. *J Clin Lab Anal* 22: 278-281, 2008.

17. **Berlowitz DR and Brienza DM**. Are all pressure ulcers the result of deep tissue injury? A review of the literature. *Ostomy/wound management* 53: 34, 2007.

18. **Black J, Baharestani MM, Cuddigan J, Dorner B, Edsberg L, Langemo D, Posthauer ME, Ratliff C and Taler G**. National Pressure Ulcer Advisory Panel's updated pressure ulcer staging system. *Advances in skin & wound care* 20: 269, 2007.

19. **Bouten CV, Oomens CW, Baaijens FP and Bader DL**. The etiology of pressure ulcers: Skin deep or muscle bound? *Arch Phys Med Rehabil* 84: 616-619, 2003.

20. **Ceelen KK, Stekelenburg A, Loerakker S, Strijkers GJ, Bader DL, Nicolay K, Baaijens FPT and Oomens CWJ**. Compression-induced damage and internal tissue strains are related. *Journal of Biomechanics* 41: 3399-3404, 2008.

21. **Chambers DE, Parks DA, Patterson G, Roy R, McCord JM, Yoshida S, Parmley LF and Downey JM**. Xanthine oxidase as a source of free radical damage in myocardial ischemia. *Journal of molecular and cellular cardiology* 17: 145, 1985.

22. **Chang ST, Linderman JJ and Kirschner DE**. Multiple mechanisms allow Mycobacterium tuberculosis to continuously inhibit MHC class II-mediated antigen presentation by macrophages. *Proceedings of the National Academy of Sciences of the United States of America* 102: 4530-4535, 2005.

23. **Chaplain MA**. Mathematical modelling of angiogenesis. *Journal of neuro-oncology* 50: 37-51, 2000.

24. **Charo IF and Ransohoff RM**. The many roles of chemokines and chemokine receptors in inflammation. *N Engl J Med* 354: 610-621, 2006.

25. **Chen X, Xu C, Zhang F and Ma J**. Comparative analysis of expression profiles of chemokines, chemokine receptors, and components of signaling pathways mediated by chemokines in eight cell types during rat liver regeneration. *Genome* 53: 608-618, 2010.

26. **Chow WW**. Deformations and stresses in soft body tissures of a sitting person. *J Biomech Eng Trans ASME* 100: 79-87, 1978.

27. **Clermont G, Bartels J, Kumar R, Constantine G, Vodovotz Y and Chow C**. *In silico* design of clinical trials: a method coming of age. *Crit Care Med* 32: 2061-2070, 2004.

28. **Dale PD, Sherratt JA and Maini PK**. Role of fibroblast migration in collagen fiber formation during fetal and adult dermal wound healing. *Bulletin of mathematical biology* 59: 1077-1100, 1997.

29. **Dallon J, Sherratt J, Maini P and Ferguson M**. Biological implications of a discrete mathematical model for collagen deposition and alignment in dermal wound repair. *Mathematical Medicine and Biology* 17: 379-393, 2000.

30. **Day J, Rubin J, Vodovotz Y, Chow CC, Reynolds A and Clermont G**. A reduced mathematical model of the acute inflammatory response: II. Capturing scenarios of repeated endotoxin administration. *J Theor Biol* 242: 237-256, 2006.

31. **Dolynchuk K, Keast D, Campbell K, Houghton P, Orsted H, Sibbald G and Atkinson A**. Best practices for the prevention and treatment of pressure ulcers. *Ostomy Wound Management* 46: 38-52, 2000.

32. **Dorsett-Martin WA**. Rat models of skin wound healing: a review. *Wound Repair Regen* 12: 591-599, 2004.

33. **Duvigneau JC, Kozlov AV, Zifko C, Postl A, Hartl RT, Miller I, Gille L, Staniek K, Moldzio R, Gregor W, Haindl S, Behling T, Redl H and Bahrami S**. Reperfusion Does Not Induce Oxidative Stress But Sustained Endoplasmic Reticulum Stress in Livers of Rats Subjected to Traumatic-Hemorrhagic Shock. *Shock* 33: 2010.

34. **Edlich RF, Winters KL, Woodard CR, Buschbacher RM, Long WB, Gebhart JH and Ma EK**. Pressure ulcer prevention. *Journal of Long Term Effects of Medical Implants* 14: 285-304, 2004.

35. **Evankovich J, Zhang R, Cardinal JS, Zhang L, Chen J, Huang H, Beer-Stolz D, Billiar TR, Rosengart MR and Tsung A**. Calcium/calmodulin-dependent protein kinase IV limits organ damage in hepatic ischemia-reperfusion injury through induction of autophagy. *American Journal of Physiology - Gastrointestinal and Liver Physiology* 303: G189-G198, 2012.

36. **Foteinou PT, Calvano SE, Lowry SF and Androulakis IP**. Translational Potential of Systems-Based Models of Inflammation. *Clinical and Translational Science* 2: 85-89, 2009.

37. **Frangogiannis NG**. Chemokines in ischemia and reperfusion. *Thromb Haemost* 97: 738-747, 2007.

38. **Frink M, Hsieh YC, Hsieh CH, Pape HC, Choudhry MA, Schwacha MG and Chaudry IH**. Keratinocyte-derived chemokine plays a critical role in the induction of systemic inflammation and tissue damage after trauma-hemorrhage. *Shock* 28: 576-581, 2007.

39. **Frost F, Roach MJ, Kushner I and Schreiber P**. Inflammatory C-reactive protein and cytokine levels in asymptomatic people with chronic spinal cord injury. *Arch Phys Med Rehabil* 86: 312-317, 2005.

40. **Gefen A**. How much time does it take to get a pressure ulcer? Integrated evidence from human, animal, and in vitro studies. *Ostomy Wound Manage* 54: 30-35, 2008.

41. **Granger DN**. Role of xanthine oxidase and granulocytes in ischemia-reperfusion injury. *American Journal of Physiology-Heart and Circulatory Physiology* 255: H1269-H1275, 1988.

42. **Hildebrand F, Hubbard WJ, Choudhry MA, Frink M, Pape HC, Kunkel SL and Chaudry IH**. Kupffer cells and their mediators: the culprits in producing distant organ damage after trauma-hemorrhage. *Am J Pathol* 169: 784-794, 2006.

43. **Houwing R, Overgoor M, Kon M, Jansen G, Van Asbeck BS and Haalboom JRE**. Pressure-induced skin lesions in pigs: reperfusion injury and the effects of vitamin E. *Journal of wound care* 9: 36-40, 2000.

44. **Hubert L and Arabie P**. Comparing partitions. *Journal of Classification* 2: 193-218, 1985.

45. **Janes KA, Albeck JG, Gaudet S, Sorger PK, Lauffenburger DA and Yaffe MB**. A Systems Model of Signaling Identifies a Molecular Basis Set for Cytokine-Induced Apoptosis. *Science* 310: 1646-1653, 2005.

46. **Kan WH, Hsieh CH, Schwacha MG, Choudhry MA, Raju R, Bland KI and Chaudry IH**. Flutamide protects against trauma-hemorrhage-induced liver injury via attenuation of the inflammatory response, oxidative stress, and apopotosis. *Journal of Applied Physiology* 105: 595-602, 2008.

47. **Kranke P, Bennett MH, Martyn-St James M, Schnabel A and Debus SE**. Hyperbaric oxygen therapy for chronic wounds. *The Cochrane Library* 2012.

48. **Kumar R, Chow CC, Bartels J, Clermont G and Vodovotz Y**. A mathematical simulation of the inflammatory response to anthrax infection. *Shock* 29: 104-111, 2008.

49. **Laurens M, Defamie V, Scozzari G, Schmid-Alliana A, Gugenheim J and Crenesse D**. Hypoxia-reoxygenation-induced chemokine transcription is not prevented by preconditioning or intermittent hypoxia, in mice hepatocytes. *Transpl Int* 18: 444-452, 2005.

50. **Lindblad WJ**. Considerations for selecting the correct animal model for dermal wound-healing studies. *J Biomater Sci Polym Ed* 19: 1087-1096, 2008.

51. **Linder-Ganz E, Engelberg S, Scheinowitz M and Gefen A**. Pressure-time cell death threshold for albino rat skeletal muscles as related to pressure sore biomechanics. *Journal of Biomechanics* 39: 2725-2732, 2006.

52. **Lu B, Rutledge BJ, Gu L, Fiorillo J, Lukacs NW, Kunkel SL, North R, Gerard C and Rollins BJ**. Abnormalities in monocyte recruitment and cytokine expression in monocyte chemoattractant protein 1-deficient mice. *J Exp Med* 187: 601-608, 1998.

53. **Maggelakis SA**. A mathematical model of tissue replacement during epidermal wound healing. *Applied Mathematical Modelling* 27: 189-196, 2003.

54. **Maier B, Lefering R, Lehnert M, Laurer HL, Steudel WI, Neugebauer EA and Marzi I**. Early versus late onset of multiple organ failure is associated with differing patterns of plasma cytokine biomarker expression and outcome after severe trauma. *Shock* 28: 668-674, 2007.

55. **Makhsous M, Lim D, Hendrix R, Bankard J, Rymer WZ and Lin F**. Finite element analysis for evaluation of pressure ulcer on the buttock: development and validation. *Neural Systems and Rehabilitation Engineering, IEEE Transactions on* 15: 517-525, 2007.

56. **Maklebust J and Sieggreen M**. *Pressure ulcers: Guidelines for prevention and management*. Lippincott Williams & Wilkins, 2001.

57. **Mandrekar P, Ambade A, Lim A, Szabo G and Catalano D**. An essential role for monocyte chemoattractant protein-1 in alcoholic liver injury: Regulation of proinflammatory cytokines and hepatic steatosis in mice. *Hepatology* 54: 2185-2197, 2011.

58. **Mantovani A, Sica A and Locati M**. Macrophage polarization comes of age. *Immunity* 23: 344-346, 2005.

59. **Marino S, Hogue IB, Ray CJ and Kirschner DE**. A methodology for performing global uncertainty and sensitivity analysis in systems biology. *J Theor Biol* 254: 178-196, 2008.

60. **McCloskey CA, Kameneva MV, Uryash A, Gallo DJ and Billiar TR**. Tissue hypoxia activates JNK in the liver during hemorrhagic shock. *Shock* 22: 380-386, 2004.

61. **McDougall S, Dallon J, Sherratt J and Maini P**. Fibroblast migration and collagen deposition during dermal wound healing: mathematical modelling and clinical implications. *Philos Transact A Math Phys Eng Sci* 364: 1385-1405, 2006.

62. **Metukuri MR, Beer-Stolz D, Namas RA, Dhupar R, Torres A, Loughran PA, Jefferson BS, Tsung A, Billiar TR, Vodovotz Y and Zamora R**. Expression and subcellular localization of BNIP3 in hypoxic hepatocytes and liver stress. *Am J Physiol Gastrointest Liver Physiol* 296: G499-G509, 2009.

63. **Mi Q, Constantine G, Ziraldo C, Solovyev A, Torres A, Namas R, Bentley T, Billiar TR, Zamora R, Puyana JC and Vodovotz Y**. A dynamic view of trauma/hemorrhage-induced inflammation in mice: principal drivers and networks. *PLoS One* 6: e19424, 2011.

64. **Mi Q, Rivière B, Clermont G, Steed DL and Vodovotz Y**. Agent-based model of inflammation and wound healing: insights into diabetic foot ulcer pathology and the role of transforming growth factor-b1. *Wound Rep Reg* 15: 617-682, 2007.

65. **Mi, Q., Solovyev, A, Zhou, L., Mikheev, M., Dutta-Moscato, J., An, G., and Vodovotz, Y.** A computer simulation of pressure ulcer formation following spinal cord injury: An application of a novel agent-based biomedical modeling framework. 2009. *Proceedings of RESNA 2009 Annual Conference*.

66. **Mosser DM and Edwards JP**. Exploring the full spectrum of macrophage activation. *Nature Reviews Immunology* 8: 958-969, 2008.

67. **Nathan C**. Points of control in inflammation. *Nature* 420: 846-852, 2002.

68. **Nieman G, Brown D, Sarkar J, Kubiak B, Ziraldo C, Dutta-Moscato J, Vieau C, Barclay D, Gatto L, Maier K, Constantine G, Billiar TR, Zamora R, Mi Q, Chang S and Vodovotz Y**. A two-compartment mathematical model of endotoxin-induced inflammatory and physiologic alterations in swine. *Crit Care Med* 40: 2012.

69. **Olsen L, Maini PK, Sherratt JA and Marchant B**. Simple modelling of extracellular matrix alignment in dermal wound healing I. Cell flux induced alignment. *Computational and Mathematical Methods in Medicine* 1: 175-192, 1998.

70. **Olsen L, Sherratt JA, Maini PK and Arnold F**. A mathematical model for the capillary endothelial cell-extracellular matrix interactions in wound-healing angiogenesis. *Mathematical Medicine and Biology* 14: 261-281, 1997.

71. **Peirce SM, Skalak TC, Rieger JM, Macdonald TL and Linden J**. Selective A2A adenosine receptor activation reduces skin pressure ulcer formation and inflammation. *American Journal of Physiology-Heart and Circulatory Physiology* 281: H67-H74, 2001.

72. **Peitzman AB, Billiar TR, Harbrecht BG, Kelly E, Udekwu AO and Simmons RL**. Hemorrhagic shock. *Curr Probl Surg* 32: 925-1002, 1995.

73. **Ranzato E, Patrone M, Pedrazzi M and Burlando B**. Hmgb1 promotes wound healing of 3T3 mouse fibroblasts via RAGE-dependent ERK1/2 activation. *Cell biochemistry and biophysics* 57: 9-17, 2010.

74. **Ray JC, Flynn JL and Kirschner DE**. Synergy between Individual TNF-Dependent Functions Determines Granuloma Performance for Controlling Mycobacterium tuberculosis Infection. *The Journal of Immunology* 182: 3706-3717, 2009.

75. **Regan MA, Teasell RW, Wolfe DL, Keast D, Mortenson WB and Aubut JA**. A systematic review of therapeutic interventions for pressure ulcers after spinal cord injury. *Arch Phys Med Rehabil* 90: 213-231, 2009.

76. **Robson MC, Hill DP, Woodske ME and Steed DL**. Wound healing trajectories as predictors of effectiveness of therapeutic agents. *Arch Surg* 135: 773-777, 2000.

77. **Saez-Rodriguez J, Alexopoulos LG, Zhang M, Morris MK, Lauffenburger DA and Sorger PK**. Comparing Signaling Networks between Normal and Transformed Hepatocytes Using Discrete Logical Models. *Cancer Res* 71: 5400-5411, 2011.

78. **Sahin H, Trautwein C and Wasmuth HE**. Functional role of chemokines in liver disease models. *Nat Rev Gastroenterol Hepatol* 7: 682-690, 2010.

79. **Saiman Y and Friedman SL**. The role of chemokines in acute liver injury. *Front Physiol* 3: 213, 2012.

80. **Salcido R, Popescu A and Ahn C**. Animal models in pressure ulcer research. *The journal of spinal cord medicine* 30: 107, 2007.

81. **Saltelli A, Chan K and Scott EM**. *Sensitivity Analysis*. Chichester, New York: Wiley, 2000.

82. **Segal JL, Gonzales E, Yousefi S, Jamshidipour L and Brunnemann SR**. Circulating levels of IL-2R, ICAM-1, and IL-6 in spinal cord injuries. *Arch Phys Med Rehabil* 78: 44-47, 1997.

83. **Segovia-Juarez JL, Ganguli S and Kirschner D**. Identifying control mechanisms of granuloma formation during M. tuberculosis infection using an agent-based model. *Journal of Theoretical Biology* 231: 357-376, 2004.

84. **Sherratt JA and Dallon JC**. Theoretical models of wound healing: past successes and future challenges. *C R Biol* 325: 557-564, 2002.

85. **Solovyev A, Mikheev M, Zhou L, Ziraldo C, An G and Mi Q**. SPARK: A Framework for Multi-Scale Agent-Based Biomedical Modeling. *International Journal of Agent Technologies and Systems (IJATS)* 2: 18-30, 2010.

86. **Solovyev, A. and Mi, Q.** Simple Platform for Agent-Based Representation of Knowledge (SPARK). 2012.

87. **Stern JR, Christley S, Zaborina O, Alverdy JC and An G**. Integration of TGF-beta- and EGFR-based signaling pathways using an agent-based model of epithelial restitution. *Wound Repair Regen* 20: 862-863, 2012.

88. **Straino S, Di Carlo A, Mangoni A, De Mori R, Guerra L, Maurelli R, Panacchia L, Di Giacomo F, Palumbo R and Di Campli C**. High-mobility group box 1 protein in human and murine skin: involvement in wound healing. *Journal of Investigative Dermatology* 128: 1545-1553, 2008.

89. **Tieu BC, Lee C, Sun H, Lejeune W, Recinos A, III, Ju X, Spratt H, Guo DC, Milewicz D, Tilton RG and Brasier AR**. An adventitial IL-6/MCP1 amplification loop accelerates macrophage-mediated vascular inflammation leading to aortic dissection in mice. *J Clin Invest* 119: 3637-3651, 2009.

90. **Vodovotz Y**. Translational systems biology of inflammation and healing. *Wound Repair Regen* 18: 3-7, 2010.

91. **Vodovotz Y, Clermont G, Chow C and An G**. Mathematical models of the acute inflammatory response. *Curr Opin Crit Care* 10: 383-390, 2004.

92. **Vodovotz Y, Constantine G, Rubin J, Csete M, Voit EO and An G**. Mechanistic simulations of inflammation: Current state and future prospects. *Math Biosci* 217: 1-10, 2009.

93. **Vodovotz Y, Csete M, Bartels J, Chang S and An G**. Translational systems biology of inflammation. *PLoS Comput Biol* 4: 1-6, 2008.

94. **Walker DC, Hill G, Wood SM, Smallwood RH and Southgate J**. Agent-based computational modeling of wounded epithelial cell monolayers. *IEEE Trans Nanobioscience* 3: 153-163, 2004.

95. **Walker D, Wood S, Southgate J, Holcombe M and Smallwood R**. An integrated agent-mathematical model of the effect of intercellular signalling via the epidermal growth factor receptor on cell proliferation. *Journal of Theoretical Biology* 242: 774-789, 2006.

96. **Wang H, Gao X, Fukumoto S, Tademoto S, Sato K and Hirai K**. Differential expression and regulation of chemokines JE, KC, and IP-10 gene in primary cultured murine hepatocytes. *J Cell Physiol* 181: 361-370, 1999.

97. **Wang HM, Hsiao CL, Hsieh AR, Lin YC and Fann CSJ**. Constructing Endophenotypes of Complex Diseases Using Non-Negative Matrix Factorization and Adjusted Rand Index. *PLoS ONE* 7: e40996, 2012.

98. **Waugh HV and Sherratt JA**. Macrophage dynamics in diabetic wound dealing. *Bull Math Biol* 68: 197-207, 2006.

99. **Waugh HV and Sherratt JA**. Modeling the effects of treating diabetic wounds with engineered skin substitutes. *Wound Repair Regen* 15: 556-565, 2007.

100. **Wearing HJ and Sherratt JA**. Keratinocyte growth factor signalling: a mathematical model of dermal-epidermal interaction in epidermal wound healing. *Math Biosci* 165: 41-62, 2000.

101. **Xing Z, Pei J and Philip SY**. Early classification on time series. *Knowledge and information systems* 31: 105-127, 2012.

102. **Xing, Zhengzheng, Pei, Jian, and Yu, Philip S.** Early prediction on time series: a nearest neighbor approach. 1297-1302. 2009.

103. **Yamaguchi Y, Matsumura F, Liang J, Okabe K, Ohshiro H, Ishihara K, Matsuda T, Mori K and Ogawa M**. Neutrophil elastase and oxygen radicals enhance monocyte chemoattractant protein- expression after ischemia/reperfusion in rat liver. *Transplantation* 68: 1459-1468, 1999.

104. **Yang H, Ochani M, Li J, Qiang X, Tanovic M, Harris HE, Susarla SM, Ulloa L, Wang H, DiRaimo R, Czura CJ, Wang H, Roth J, Warren HS, Fink MP, Fenton MJ, Andersson U and Tracey KJ**. Reversing established sepsis with antagonists of endogenous high-mobility group box 1. *Proc Natl Acad Sci U S A* 101: 296-301, 2004.

105. **Yang H, Wang H, Czura CJ and Tracey KJ**. HMGB1 as a cytokine and therapeutic target. *Journal of endotoxin research* 8: 469-472, 2002.

106. **Yang S, Hu S, Hsieh YC, Choudhry MA, Rue III LW, Bland KI and Chaudry IH**. Mechanism of IL-6-mediated cardiac dysfunction following trauma-hemorrhage. *Journal of molecular and cellular cardiology* 40: 570-579, 2006.

107. **Yeung, K. Y.** Principal component analysis for clustering gene expression data. Bioinformatics 17(9), 763-774. 2001.

108. **Yeung KY, Haynor DR and Ruzzo WL**. Validating clustering for gene expression data. *Bioinformatics* 17: 309-318, 2001.

109. **Zenati MS, Billiar TR, Townsend RN, Peitzman AB and Harbrecht BG**. A brief episode of hypotension increases mortality in critically ill trauma patients. *J Trauma* 53: 232-236, 2002.